Feedback Control of Collective Spin States for Atom Interferometry

Ralf Kohlhaas

INSTITUT D'OPTIQUE GRADUATE SCHOOL

ÉCOLE DOCTORALE ONDES ET MATIÈRE

Discipline : Physique

THÈSE
pour l'obtention du grade de Docteur en science de l'Institut d'Optique Graduate School
préparée au Laboratoire Charles Fabry

soutenue le 17/01/2014

par

Ralf KOHLHAAS

Feedback Control of Collective Spin States for Atom Interferometry

---

Composition du jury **:**

M.	A. Aspect	Directeur de thèse
M.	R. Kaiser	Rapporteur
M.	E. Rasel	Rapporteur
M.	S. Bize	Examinateur
M.	J.-M. Courty	Examinateur
M.	P. Pillet	Président du jury
M.	P. Bouyer	Membre invité
M.	A. Landragin	Membre invité

To my family.

Contents

Introduction

On 22 October 1707 four English warships, the Association, Eagle, Firebrand and Romney, hit ground in a foggy night at the Scilly Islands on the English coast and sank. Two thousand lives were lost. The accident would have been avoidable - had only the crews known their longitude. At that time, no reliable method existed to determine the longitude of a ship. An astronomical solution seemed most promising and had led before to the construction of the astronomical observatories in Greenwich and Paris, but without any success so far for the longitude problem.

In 1714, the English government issued the "longitude act", awarding 20.000 pounds (the equivalent of several million euros today) to anybody who could determine a longitude within half a degree. Although everybody expected an astronomical solution, the final answer turned out to be much simpler: a good clock. With the ability to take a timekeeper with you, and the possibility to determine the local time over the position of the sun, the time difference to the home port could be calculated.

At the beginning of the 18th century, the best available clocks went wrong by several seconds a day and were far from being transportable. Leading scientists including Isaac Newton considered the determination of longitude by a portable timekeeper hopeless. They were proven wrong by John Harrison, a former carpenter and then clockmaker. He built in a life work from 1713 to 1776 transportable clocks which went only wrong in a fraction of a second over a whole month, and his portable clock, called the chronometer, became the standard for determining longitude. The stability of the chronometer was owed to a careful choice of materials and new inventions (for example, it used bimetallic strips and caged roller bearings, both invented by John Harrison), and became the standard for the determination of longitude in the navy[1].

[1] Nevertheless, John Harrison has never been awarded the official longitude act prize as a result of political quarrels. A very good book about the history of the chronometer and the longitude act can be found in [Sobel 07].

Today's best clocks are based on the laws of quantum mechanics. They go wrong only by a fraction of a second over the age of the universe, or in other words have an instability of 10^{-18} [Hinkley 13, Bloom 13]. Quantum mechanics is based on a set of rules which are not common with the classical world we face every day. First, we know the energy can only exist in fixed packages, so called quanta. This gives an exact building plan for single atoms, and because its constituents (protons, neutrons and electrons) are always the same, all atoms with the same number of constituents are the same as well. The difference between the energy levels $\Delta E = E_2 - E_1$ in atoms can serve then as an absolute frequency reference via Planck's law $\Delta E = \hbar\omega$, where $\hbar = 2\pi\, 6.626 \times 10^{-34}$ Js is the reduced Planck's constant and ω an angular frequency.

Another property of quantum mechanics is that objects very well isolated from their environment can be prepared, and survive, in a superposition of different states. A single electron can behave as if it travels two paths at the same time, as if it were an electromagnetic wave. In an atomic interferometer, it is the internal or external states of atoms which are put in superposition states. Dedicated protocols, such as the Ramsey scheme [Ramsey 80], use the creation and combination of superposition states for the measurement of physical quantities such as frequencies, accelerations and magnetic fields [Berman 97].

In an atomic clock, the frequency of a macroscopic oscillator (e.g. a quartz crystal) is periodically compared to a transition frequency of an atomic species. This oscillator (also called local oscillator LO) is then stabilized on the atomic transition frequency. The frequency of the classical oscillator can be measured with a counter and is used for the definition of time. The stability of the LO improves when its frequency is compared to the frequency of the atomic reference for a longer interval. But this interrogation time is usually limited: during the interrogation, the atoms are in a superposition of states, and the superposition can be destroyed under the influence of the environment. This process is called decoherence, and the initial ability of the atomic states to interfere, their coherence, is reduced.

The most precise atomic clocks are based on atomic ensembles, and the main decoherence source is the frequency noise of the free running LO itself. Noise of this kind is called "collective noise" because it affects all atoms in the same

way. A direct approach to reduce the effect of the bare LO frequency noise is to pre-stabilize the LO as well as possible. In atomic clocks working with optical transitions, the LO is a laser. The stabilization of lasers on ultra-stable optical resonators is a target pursued by a large number of groups around the world, and tremendous progress has been made with instabilities down to the 10^{-16} level at one second [Jiang 11, Thorpe 11, Kessler 12]. However, the interrogation times of optical atomic clocks have remained below a fraction of a second. In trapped microwave clocks, the recently found spin-self rephasing of atoms [Deutsch 10] could potentially enable interrogation times of tens of seconds, but the quality of the existing microwave oscillators does not allow it.

An alternative solution to protect a quantum system against decoherence is to measure it, and to apply feedback either on the quantum system itself or on its environment. Another feature in quantum mechanics comes into play here, the property that measuring a quantum system also modifies it. The control laws in quantum mechanics can be therefore very distinct from classical control laws and have been subject to extensive theoretical efforts [Doherty 00, Lloyd 00, Ahn 02, Mancini 07] and first experimental demonstrations [Armen 02, Smith 02, Gillett 10]. Only recently, for the first time a quantum state, a photon number state, was permanently stabilized against decoherence [Sayrin 11]. Experiments on superconducting qubits show fast progress in the same direction, with the real time stabilization of Rabi-oscillations [Vijay 12] and quantum measurements with variable measurement strength [Hatridge 13]. The main application area is likely to be here quantum information processing.

In this thesis, we bring the concept of feedback on a quantum system to atomic interferometers. From a first glance, this approach might appear to be a bad idea. The atoms in the interferometer act as a probe, and as such should by no means be disturbed during their evolution. But simply measuring the atoms does exactly that. However, there is a way out of this problem: atomic ensembles can be measured gently, or "weakly", to provide significant information while changing the quantum state only very little [Aharonov 88, Smith 04, Aharonov 10]. This makes it possible to use classical feedback control for the collective quantum system. We will show that in this way decoherence by collective noise in atomic interferometers can at least be partially removed. Our experimental results and feedback protocols indicate a realistic potential for the improvement of atomic sensors by active feedback control.

This is the third PhD thesis handed in on the experimental apparatus after Simon Bernon [Bernon 11a] and Thomas Vanderbruggen [Vanderbruggen 12]. As a postdoc, Andrea Bertoldi took both part in the experimental work and later took over a large part of the direction of the experiment. Arnaud Landragin and Philippe Bouyer were the scientific directors of the experiment and Alain Aspect as the head of the Atom Optics group and my PhD supervisor advised the performed work. Etienne Cantin is a new PhD student who contributed to the last experimental results in this manuscript. The results presented in this manuscript have been already partially covered by our previous publications [Bernon 11b, Kohlhaas 12, Vanderbruggen 13], and results from the last two chapters remain to be published. The feedback protocols in the last chapter have been submitted for a patent application.

The experimental setup as it already existed at the beginning is described only briefly, as a basis for the understanding of the further work. Detailed calculations or derivations will only be shown if they are original and are otherwise cited. For most explanations, at first a simple picture is given before a more formal description. The manuscript is organized in 5 chapters. Below a summary of the chapters is given.

- **Chapter 1**. In this chapter, the main theoretical concepts used in the thesis are introduced. The Bloch sphere picture describes the structure and evolution of the internal states of atomic ensembles. The formulation in the Dicke state basis allows for arbitrary state transformations. Generalized quantum measurements are introduced as a generalization of the ideal projective measurement. The concept of generalized quantum measurements on collective spin states is explained, and the special case of weak measurements is discussed.

- **Chapter 2**. The experimental setup for the preparation of cold atomic clouds is presented. It contains several unique features, including a dipole trap in an optical cavity in butterfly configuration. We present novel technological solutions such as a new stabilization scheme of a laser on a cavity, and the production of a Bose-Einstein condensate with a cavity-enhanced dipole trap. We show a new procedure to engineer the atomic light shift on an optical transition and demonstrate how we prepare a pure internal state of a dense ensemble of atoms with optical methods.

- **Chapter 3**. In this chapter, we describe the development of our system for nondestructive measurements of cold atomic ensembles. It is based on frequency modulation spectroscopy, and is the only system where the population difference of two non-magnetic atomic states can be read out nondestructively with a single optical beam. We show how to set the couplings of the light to the atomic levels correctly, avoid light shifts from the probe and balance the spontaneous emission to the probed states. The beam waist of the beam is optimized for a maximal signal-to-noise ratio. We show some first results with the nondestructive detection system such as the real time observation of Rabi oscillations.

- **Chapter 4**. We present the feedback control of the collective internal states in an atomic ensemble. All atoms are prepared in a superposition state of two atomic levels, and artificial noise is applied on the atoms. The state of the atoms is measured weakly, and feedback with coherent manipulations restores partly the initial state. We study theoretically different parameters over which the feedback efficiency can be characterized, and choose experimentally to observe the output coherence of the state. We show that there is a trade-off between the information and the perturbation from the measurement. Different noise and feedback scenarios are studied. The work in this chapter represents the first demonstration of the protection of a superposition state against decoherence with feedback control, although only for the case of an ensemble and collective noise.

- **Chapter 5**. We stabilize the phase of a LO in an atomic clock on the phase of a superposition state of the atoms, as it was proposed in [Shiga 12] to improve atomic clocks. The scheme is equivalent to remove the decoherence of the atoms by feedback on the environment, which is here the LO. We find a drawback in the original phase lock scheme proposed in [Shiga 12], and develop a new feedback protocol. The experimental results raise realistic hopes that our methods could be used to improve atomic clocks. It is shown that our feedback protocol is versatile, and could be applied to other atomic interferometers such as gravimeters. The work in this chapter shows for the first time the stabilization of a classical object to a quantum system in a superposition state, which could have widespread applications for precision measurements.

The content of this manuscript is more focused on new ideas and techniques than on pushing an instrument to its limits. The hope is expressed here that the reader

will find some of it interesting, and that perhaps part of the work will be the basis for further research.

1. Collective Spin States and Generalized Quantum Measurements

1.1. Introduction

The central goal of this thesis is to demonstrate how trapped coherent atomic ensembles can be measured nondestructively and controlled via feedback, and to investigate if this could lead to an improvement of atomic interferometers. In this chapter, the theoretical basics for this work are given. The trapped atoms that we use can be approximated by a two-level system, one of the most basic systems in quantum mechanics. A useful tool to illustrate the evolution of a single two-level system is the Bloch sphere model, which is introduced in Section 1.2.1. In this model, the state of a two-level system becomes a pseudo-spin, in analogy to a real spin vector of for example a magnetic moment.

Since we work with an ensemble of atoms, a generalization of the Bloch sphere picture to many atoms is needed. The simplest collective state of an ensemble of two-level atoms, a coherent spin state (CSS), is then introduced in Section 1.2.2. In a CSS, all atoms are in the same pure internal state, and all single pseudo-spins can be added up to from a giant collective spin. Although we do not work with entangled states, the concept of a spin squeezed state (SSS) is introduced in Section 1.2.3. In a spin squeezed state, a constraint is imposed on the collective spin state and the indistinguishable individual spins are correlated. Since a SSS can be the result of a partially projective quantum measurement, it is a good starting point for the introduction of generalized quantum measurements on collective atomic states.

To actively control any system, one has to measure it. In quantum mechanics, the measurement process itself can modify the system of interest. The prime example here is an ideal projective measurement, where before the measurement a particle can be in a superposition of two states, and after the measurement it is only in one of the two states. The projective measurement is the textbook example

of a quantum measurement, but unfortunately often also the only type of quantum measurement taught to students of quantum mechanics. As a matter of fact, the ideal projective measurement does not exist in practice, since any measurement always contains some residual noise. The experiments which have so far come the closest to an ideal projective measurement were performed on microwave photons measured by Rydberg atoms [Guerlin 07] and on trapped ions [Hume 07][1].

The main results of this thesis will rely on the fact that a measurement on a quantum system does not necessarily have to be projective. In fact, our goal will be to project the measured state as little as possible while still obtaining sufficient information to perform feedback on the atoms. The concept of general quantum measurements is introduced in Section 1.3 with the Kraus operator formalism, which gives the rules to formulate general quantum measurements. We apply the concept then to collective atomic states in Section 1.3.3.5, and define the important parameters for the measurement process. The results from this last section will then be repeatedly used throughout this manuscript. The feedback control of collective atomic states is not treated in this chapter, and is developed alongside with the experimental results in Chapter 4.

1.2. Collective Spin States

1.2.1. Bloch Sphere

The Bloch sphere representation has been introduced for the description of nuclear magnetic resonance (NMR) phenomena, and named in honor of F. Bloch for his pioneering work on nuclear induction [Bloch 46]. In NMR, the real nuclear magnetic spin with a vector $\mathbf{M}$ in an external magnetic field $\mathbf{B}$ is the Bloch vector. It can have any direction in space, and the Bloch sphere is formed by the set of all spin directions. By going in the rotating frame of a transverse oscillating magnetic field, an easy picture for manipulations of the nuclear spin can be obtained, and this is still the basic model in NMR experiments.

It was later pointed out by R. Feynman and coworkers [Feynman 57] that the Bloch sphere model can be generalized to other systems containing at least two

[1] The atomic state of $^{27}Al^{+}$ could be measured in [Hume 07] with a certainty of 99.94%. The development of measurement tools for ions and microwave photons were one reason for the Nobel prize in Physics in 2012 to S. Haroche and D. Wineland.

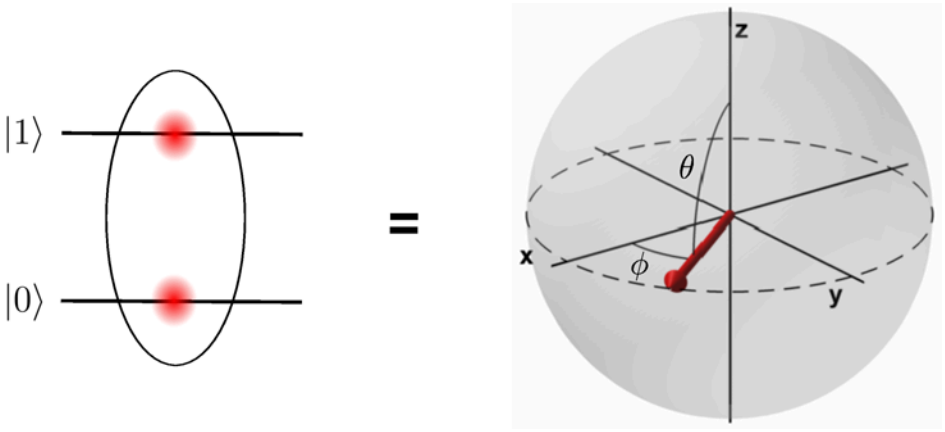

Figure 1.1.: Introduction to the Bloch sphere picture. The state of a two-level system can be represented as a spin vector on the Bloch sphere. The z-axis corresponds to the population difference and the $x-y$ plane designates the phase between the superposition state referenced on the phase of a local oscillator (LO). The spin direction is described with the azimuthal angle ϕ and the polar angle θ.

distinct levels. A single atom containing two quantized energy levels can then be represented as a pseudo-spin on the Bloch sphere. The same holds as well for superposition states of the polarization of a photon [O'Brien 07], but also for classical systems such as coupled modes of a mechanical oscillator [Faust 13]. The Bloch sphere is a useful tool to describe atomic interferometers, notably atomic clocks. The state of a single two-level system can be described as

$$|\varphi\rangle = a\,|0\rangle + be^{-i\omega_{\mathrm{at}}t}\,|1\rangle\ , \tag{1.1}$$

where a and b are the probability amplitudes to be in state $|0\rangle$ or $|1\rangle$ and it holds $|a|^2 + |b|^2 = 1$. We will later identify in the experimental work $|0\rangle$ and $|1\rangle$ to be two hyperfine ground states of ^{87}Rb. The frequency ω_{at} comes from the energy difference of the two energy states with $E = \hbar(\omega_1 - \omega_0) = \hbar\omega_{\mathrm{at}}$. We can therefore imagine the two states $|0\rangle$ and $|1\rangle$ as two oscillators with angular frequencies ω_0 and ω_1. For a superposition state, the relative phase $\phi_{\mathrm{at}} = \omega_{\mathrm{at}}t$ oscillates then at an angular frequency ω_{at}.

The fast oscillating term $e^{-i\omega_{\mathrm{at}}t}$ can be removed by entering a rotating frame at a frequency ω_{at}. In practice, this requires a LO with a frequency $\omega_{\mathrm{LO}} = \omega_{\mathrm{at}}$ as

a reference. However, in general the frequency ω_{LO} of the LO is not stable. In the special case of an atom clock, the task is even to stabilize ω_{LO} on ω_{at}. In the rotating frame of the LO, the phase of the superposition state is $\phi = \phi_{\mathrm{LO}} - \phi_{\mathrm{at}}$. The state from Equation (1.1) referenced to the LO frame should be represented with both its amplitude and phase, which makes the Bloch sphere a suitable model as presented in Figure 1.1. Note that in the Bloch sphere picture there is no information if the phase of the LO or of the atoms is changed.

For the formal description of the state as a Bloch vector, the state is written as a spin-$\frac{1}{2}$ particle similar as for the description of angular momentum operators. The spin vector $\mathbf{j}$ can be decomposed in three orthogonal components via the operators [Itano 93]

$$j_x = \frac{1}{2}\left(|0\rangle\langle 1| + |1\rangle\langle 0|\right), \tag{1.2}$$

$$j_y = \frac{i}{2}\left(|0\rangle\langle 1| - |1\rangle\langle 0|\right), \tag{1.3}$$

$$j_z = \frac{1}{2}\left(|1\rangle\langle 1| - |0\rangle\langle 0|\right), \tag{1.4}$$

which fulfill the commutation relations

$$[j_k, j_l] = i\epsilon_{klm} j_m \ . \tag{1.5}$$

When the spin vector is written in spherical coordinates the expectation values of its components are

$$\langle j_x\rangle = \frac{1}{2}\sin\theta\cos\phi, \tag{1.6}$$

$$\langle j_y\rangle = \frac{i}{2}\sin\theta\sin\phi, \tag{1.7}$$

$$\langle j_z\rangle = \frac{1}{2}\cos\theta, \tag{1.8}$$

where as before ϕ is the phase between the LO and the atoms and θ parametrizes the population difference.

1.2.2. Coherent Spin States

On the experiment, we will work with a cloud of cold atoms, which corresponds to an ensemble of two-level systems. The picture above can be easily extended to this

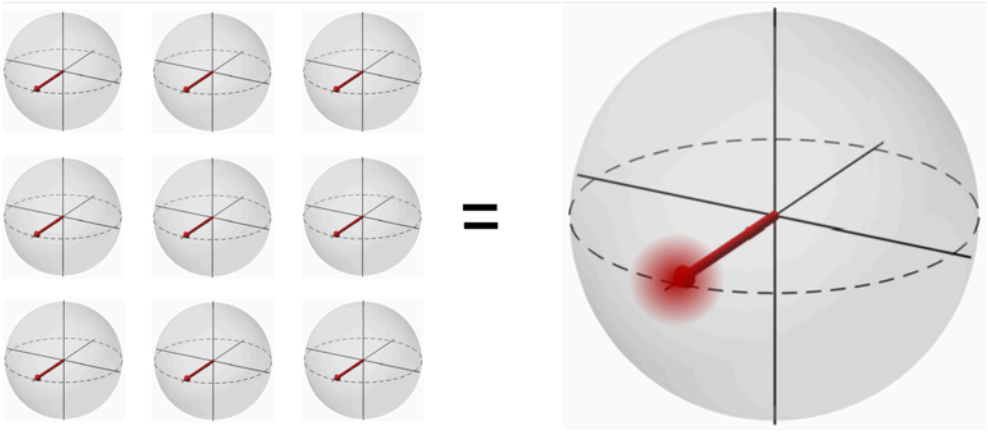

Figure 1.2.: Construction of a CSS. The pseudo-spins of a an ensemble of two-level atoms with the same pure internal state are added to form a large spin. The noise around the CSS is the projection noise.

case, especially if all the two-level systems are in the same (pure) internal state. All the single pseudo-spins can then simply be added up to form a giant collective spin (Figure 1.2), similarly to adding single dipoles to obtain the full polarization. The new collective state is called a coherent spin state (CSS), and has a length of $J = \frac{N_{\text{at}}}{2}$, where N_{at} is the total number of particles or atoms belonging to the state.

The operators for the spin components can be constructed with the single spin operator by $J_c = \sum_n j_c^{(n)}$, with $c = x, y, z$ and n numbers the operator for each single spin. In the same way as for a single spin, the commutation relations

$$[J_k, J_l] = 2i\epsilon_{klm} J_m, \tag{1.9}$$

for the total spin hold. Equation (1.9) also holds if the components k, l, m are not the axes x, y, z, but any set of three orthogonal directions on the Bloch sphere α, β, γ. The Robertson-Schroedinger uncertainty relation[2] [Robertson 29] then writes

$$\Delta J_\alpha \Delta J_\beta \geq \frac{1}{2} \left| \langle J_\alpha, J_\beta \rangle \right| \ , \tag{1.10}$$

[2]The first heuristic arguments of an uncertainty relation for the observables of the same quantum system was given by W. Heisenberg [Heisenberg 27]. Its general form given here was formulated however by H. P. Robertson and E. Schrödinger.

which leads for a CSS to

$$\Delta J_\alpha \Delta J_\beta = \frac{1}{2} \left| \langle J_\gamma \rangle \right| \ , \tag{1.11}$$

and by symmetry we have

$$\Delta J_\alpha = \Delta J_\beta = \sqrt{\frac{J}{2}} = \sqrt{\frac{N_{\mathrm{at}}}{4}} \ . \tag{1.12}$$

We can therefore draw a circular noise region perpendicular to any CSS on the Bloch sphere which is called the atomic projection noise.

The Robertson-Schrödinger uncertainty relation gives information about the distribution of the measurement results of one of the observables if the same quantum state is prepared several times. It is intrinsically not a statement about the results of successive quantum measurements on the same system, as it was the first motivation by Werner Heisenberg for the uncertainty relation. For example, consider Equation (1.11) with a first precise measurement result such that $\Delta J_\alpha = 0$. This would imply that $\Delta J_\beta = \infty$, which is obviously wrong because J_β is bounded by the full spin length J.[3] What is the lowest limit on the uncertainty of successive measurements on the same quantum system is at the moment a topic of an open debate, in which the Ozawa error-disturbance relation [Ozawa 03, Erhart 12, Rozema 12] is one possible answer.

The uncertainty from the Robertson-Schrödinger relation has its origin in the microscopic properties of the collective quantum system. For a formal description of a CSS, we can write it in the basis of the energy eigenstates of J_z, which are called the Dicke states named after R. H. Dicke [Dicke 54]. The eigenvalues and eigenstates of J_z are

$$J_z \left| J, m \right\rangle = m \left| J, m \right\rangle \ . \tag{1.13}$$

The CSS in spherical coordinates and in the single particle basis is

$$\left| \theta, \phi \right\rangle = \bigotimes_n^{N_{\mathrm{at}}} \left[\cos \frac{\theta}{2} \left| 0 \right\rangle_n + e^{i\phi} \sin \frac{\theta}{2} \left| 1 \right\rangle_n \right] \ . \tag{1.14}$$

[3] A general proof that the Heisenberg uncertainty relation as a statement about measurements is violated for projective measurements and bounded variables is given in [Ozawa 05] (theorem 5).

In the Dicke state basis, this becomes [Zhang 90]

$$|\theta,\phi\rangle = \sum_{m=_J}^{J} c_m(\theta) e^{-i(J+m)\phi} |J,m\rangle \ , \tag{1.15}$$

where the coefficients c_m give a binomial distribution with

$$c_m = \left[\frac{(2J)!}{(J+m)!(J_m)!}\right]^{\frac{1}{2}} \cos^{J-m}\frac{\theta}{2} \sin^{J+m}\frac{\theta}{2} \ . \tag{1.16}$$

From the Moivre-Laplace theorem, we can approximate the binomial distribution for $J \gg 1$ by

$$c_m = \frac{1}{\sqrt{\sqrt{\pi J}\sin\theta}} e^{-\frac{(m-J\cos\theta)^2}{2J\sin^2\theta}} \ . \tag{1.17}$$

For example, in the case of $\theta = \frac{\pi}{2}$ (state on the equator of the Bloch sphere), the probability distribution $p(m)$ to measure the result m with the operator J_z is

$$p(m,\theta=\frac{\pi}{2}) = c_m^2 = \frac{1}{\sqrt{\pi J}} e^{-\frac{m^2}{J}} \ , \tag{1.18}$$

which is the same distribution as expected from the Robertson-Schrödinger uncertainty relation in Equation (1.11). The atomic shot noise results from the fact that each individual spin can be after the measurement either in $|0\rangle$ or $|1\rangle$. This leads for all particles to a binomial distribution of the total population difference.

Under a global measurement of the collective spin, the individual spins are indistinguishable. If the system is therefore found after the measurement in a Dicke state, the collective state is in a superposition of all possibilities of how the individual spins can form the found energy state. A Dicke state is therefore a highly entangled state, in which the individual spins are correlated. For example, the Dicke state $|J, m = -J+1\rangle$, where only one spin is in an excited state, can be written as

$$|J, m = -J+1\rangle = \frac{1}{\sqrt{N_{\text{at}}}} \sum_n j_{+,n} |00\ldots0\rangle \ , \tag{1.19}$$

where $j_+ = j_x + ij_y$ is the single spin raising operator which transforms a spin n from $|0\rangle$ to $|1\rangle$ ($j_- = j_x - ij_y$ performs the opposite operation). A Dicke state has no mean spin direction and is represented as a ring around the Bloch sphere

(see Figure 1.3). It is interesting to note that although the spins in a CSS are uncorrelated, it can be constructed from a basis where the single spins are highly entangled.

1.2.3. Spin Squeezed States

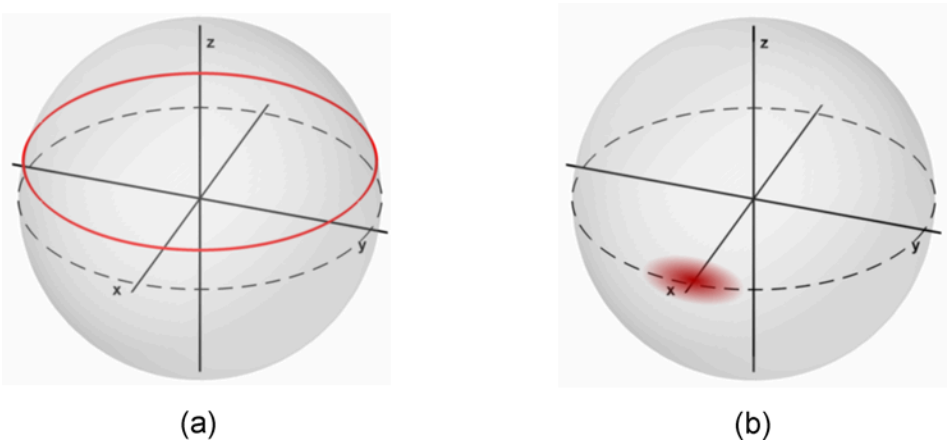

Figure 1.3.: Entangled states on the Bloch sphere. (a) Dicke state. (b) Spin squeezed state.

A spin squeezed state (SSS) resembles strongly a CSS, only that one of its noise components orthogonal to the mean spin direction is below the noise level of a CSS (see Figure 1.3). Because the total area of uncertainty of the state is fixed by the uncertainty relation, the direction orthogonal to the squeezed noise is expanded as if one would squeeze a balloon. In many precision measurements, only one noise component of the collective state is important, and a SSS can therefore lead to metrological gain. However, this assumes no or a low influence of the environment on the state (see e.g. [André 04, Shaji 07, Dorner 12]), and a detection system whose noise is below the projection noise of the SSS.

There are several criteria to define spin squeezing, and a good review can be found in [Ma 11]. Nevertheless, only two criteria are in common use, the Kitagawa-Ueda criterion [Kitagawa 93] and the Wineland criterion [Wineland 92]. The Kitagawa-Ueda criterion can be written with the spin squeezing parameter

[Kitagawa 93, Ma 11]

$$\xi_{\mathrm{KU}}^2 = \frac{\min\left(\Delta J_\perp^2\right)}{J/2} \,, \tag{1.20}$$

where $\Delta J_\perp^2$ is the variance of the noise perpendicular to the mean spin direction. For a CSS we have $\min\left(\Delta J_\perp^2\right) = \frac{J}{2}$ and $\xi_{\mathrm{KU}} = 1$. If $\xi_{\mathrm{KU}} < 1$, the projection noise is below the noise of a CSS and the state is squeezed. The fulfillment of the Kitagawa-Ueda criterion implies that the particles are at least pairwise entangled (see proof in [Wang 03]).

The relation $|\langle \mathbf{J} \rangle| = \frac{N_{\mathrm{at}}}{2}$ is only valid when the system is in a pure state. For a single two-level system, a state which has partly decohered by the interaction with the environment can be represented by a spin with a length shorter than $j = \frac{1}{2}$. We can apply the same model for a CSS, where a lower coherence is depicted by a shorter spin vector. A better criterion to take into account that the squeezing process can partially decohere the state is the Wineland criterion [Wineland 92]. It is motivated by the condition that squeezing should enable an increase in the sensitivity of a phase measurement with the collective state,

$$\Delta\phi = \frac{\xi_S}{\sqrt{N_{\mathrm{at}}}} \,, \tag{1.21}$$

where $1/\sqrt{N_{\mathrm{at}}}$ is the limit of the phase estimation with a coherent state. We obtain then

$$\xi_S^2 = \frac{(\Delta\phi)^2}{(\Delta\phi)_{CSS}^2} = \frac{\frac{(\Delta J_\perp)^2}{|\langle \mathbf{J} \rangle|}}{\frac{J}{\frac{2}{J^2}}} = \frac{N_{\mathrm{at}}\left(\Delta J\perp\right)^2}{|\langle \mathbf{J} \rangle|^2} \,. \tag{1.22}$$

Loosely speaking, the Wineland criterion says that for spin squeezing the projection noise has to be decreased as least as much as the coherence of the state that is lost during the squeezing process. Spin squeezing in atomic systems has been achieved in several experiments via atomic interactions (e.g. in [Esteve 08]), by cavity-mediated light atom interaction [Leroux 10a] and nondestructive measurements of the atomic spin (e.g. [Appel 09b, Schleier-Smith 10]). In Chapter 3, we will show in the characterization of our nondestructive measurement system that we are experimentally close to fulfill the Wineland criterion, but that the destructivity from spontaneous emission from the optical probe is slightly higher than the reduction in quantum noise.

First demonstration experiments have been given that spin squeezed

states can improve the performance of atomic interferometers [Leroux 10b, Louchet-Chauvet 10, Ockeloen 13]. Nevertheless, it remains to be shown that for absolute precision measurements spin squeezing introduces no systematic errors. The highest amount of spin squeezing so far (10.2 dB in variance) has been obtained with a cavity-aided nondestructive detection system [Bohnet 13].

1.2.4. Evolution under Unitary Operations

1.2.4.1. Rotation Operators

The operation of atomic interferometers relies on coherent manipulations of the atomic spin. Those unitary transformations can be represented by rotation operators on the Bloch sphere. We will experimentally apply rotations only around the x, y, z axes of the Bloch sphere, which are naturally defined by the rotation operators

$$R_x(\theta_1) = e^{-i\theta_1 J_x} \ , \quad R_y(\theta_2) = e^{-i\theta_2 J_y} \ , \quad R_z(\phi) = e^{-i\phi J_z} \ . \tag{1.23}$$

Experimentally, rotations around the z-axis will be usually phase shifts on the LO or a detuning between the LO frequency and the frequency of the atomic transition during an interrogation time. Rotations around x- and y-axis will be implemented by sending a coherent microwave pulse on resonance with an atomic transition onto the atoms. The rotation axis and direction can be set by changing the phase of the LO in steps of $\frac{\pi}{2}$.

The rotation operators alone are sufficient to describe the evolution of CSSs in an atomic interferometer. Nevertheless, for a highly entangled input state it is more difficult to know the distribution of the state in the Dicke state basis after a rotation from Equation (1.23). The way to solve this problem is based on the work of E. Wigner on the algebra of angular momentum states [Wigner 59]. For this purpose, we introduce the rotation operator

$$R(\alpha, \beta, \gamma) = e^{-i\alpha J_z} e^{-i\beta J_y} e^{-i\gamma J_z} \ , \tag{1.24}$$

in which contrary to before the rotations are around the z-axis, then around the y-axis, and then again around the z-axis[4]. With this operator, any rotation on the Bloch sphere can be performed. From a physical perspective, it is equivalent to per-

[4]This is the $z - y - z$ convention for Euler angles.

forming any other sequence of rotations with the operators from Equation (1.23). The rotation of a Dicke state can then be written as

$$R(\alpha,\beta,\gamma)\,|J,m\rangle = \sum_{m'}\langle J,m'|R(\alpha,\beta,\gamma)|J,m\rangle|J,m'\rangle \tag{1.25}$$

$$= \sum_{m'} D^J_{m'm}(\alpha,\beta,\gamma)|J,m'\rangle\ , \tag{1.26}$$

where $D^J_{m'm}(\alpha,\beta,\gamma)$ is the Wigner-D matrix. It can be decomposed into

$$D^J_{m'm}(\alpha,\beta,\gamma) = \langle J,m'|R(\alpha,\beta,\gamma)|J,m\rangle = e^{-im'\alpha}d^J_{m'm}(\beta)e^{-im\gamma}\ , \tag{1.27}$$

where we used the definition for the (small) Wigner-d matrix elements

$$d^J_{m'm}(\beta) = \langle J,m'|e^{-i\beta J_y}|J,m\rangle\ . \tag{1.28}$$

The key difficulty is to determine the coefficients $d^J_{m'm}(\beta)$, which were found by Wigner [Wigner 59]

$$\begin{aligned} d^J_{m'm}(\beta) = {} & [(J+m')!(J-m')!(J+m)!(J-m)!]^{1/2} \\ & \times \sum_s \left[\frac{(-1)^{m'-m+s}}{(J+m-s)!s!(m'-m+s)!(J-m'-s)!}\right. \\ & \left.\times \left(\cos\frac{\beta}{2}\right)^{2J+m-m'-2s}\left(\sin\frac{\beta}{2}\right)^{m'-m+2s}\right]. \end{aligned} \tag{1.29}$$

Equations (1.24) - (1.29) will be used in Chapter 4 for the Monte-Carlo simulation of the feedback control of a collective spin state.

1.2.4.2. Ramsey Interferometer

We show now that the rotation operators from Equation (1.23) are sufficient to describe both the mean spin direction and the projection noise of a CSS after unitary evolution on the Bloch sphere. As an example, a Ramsey interferometer is treated. Ramsey interferometry will be the basis of many measurements in this thesis, and is one method to operate atomic clocks as it will be presented in Chapter 5. For the development of his "separated oscillatory field method", N. F. Ramsey received the Nobel prize in physics in 1989.

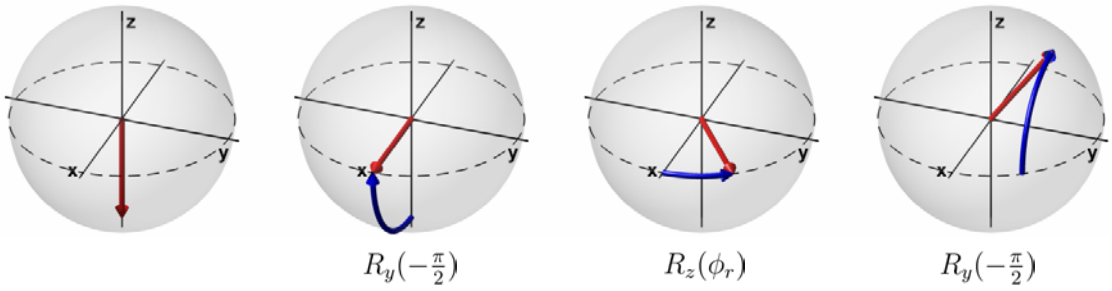

Figure 1.4.: Operation principle of a Ramsey interferometer. It includes the preparation of a superposition state, a free evolution time T and the mapping of the acquired phase on the z-axis of the Bloch sphere.

The operation principle of a Ramsey interferometer is depicted in Figure 1.4. The interferometer begins with all atoms prepared in the ground state, i.e. $|\Psi_0\rangle = |\theta = \pi, \phi = 0\rangle$. A first rotation, called a $\frac{\pi}{2}$-pulse, prepares the superposition state $\left|\theta = \frac{\pi}{2}, \phi = 0\right\rangle$. During a free evolution time T, the spin rotates by an angle ϕ_r around the equator of the Bloch sphere which gives the state $\left|\theta = \frac{\pi}{2}, \phi = \phi_\mathrm{r}\right\rangle$. The goal of the Ramsey interferometer is to measure the phase ϕ_r, but usually only the population difference can be read out directly. A final $\frac{\pi}{2}$-pulse therefore maps the phase on the z-axis of the Bloch sphere and gives the final state $\left|\theta = \phi_\mathrm{r}, \phi = \frac{\pi}{2}\right\rangle$. The complete interferometer sequence can be described by the unitary evolution operator

$$U_R = e^{i\frac{\pi}{2}J_y} e^{-i\phi_\mathrm{r} J_z} e^{i\frac{\pi}{2}J_y} \,. \tag{1.30}$$

We are interested in the expectation value and the noise of the final measurement along the z-axis. For the expectation value, we have

$$\begin{aligned} \langle J_z \rangle &= \left\langle \Psi_0 \left| U_R^\dagger J_z U_R \right| \Psi_0 \right\rangle && (1.31)\\ &= -\cos\phi_\mathrm{r} \langle J_z \rangle_0 + \sin\phi_\mathrm{r} \langle J_y \rangle_0 && (1.32)\\ &= J\cos\phi_\mathrm{r} \,, && (1.33) \end{aligned}$$

and for the noise variance

$$\begin{aligned} (\Delta J_z)^2 &= (\Delta J_z)_0^2 \cos^2\phi_\mathrm{r} + (\Delta J_y)_0^2 \sin^2\phi_\mathrm{r} - \sin\phi_\mathrm{r}\cos\phi_\mathrm{r} \langle J_z J_y + J_y J_z \rangle && (1.34)\\ &= \frac{J}{2}\sin^2\phi_\mathrm{r} \,. && (1.35) \end{aligned}$$

The only noise source for the phase for a perfectly precise detection is the projection

noise, and from error propagation one obtains

$$\Delta\phi = \frac{\Delta J_z}{\left|\frac{\partial\langle J_z\rangle}{\partial\phi}\right|} = \frac{1}{\sqrt{N_{\mathrm{at}}}} \,. \tag{1.36}$$

The read out noise for a CSS is therefore independent of the rotation angle. However, this is only true as long as there is no additional detection noise which would be added to the variance in Equation (1.35). The precision of the phase estimation decreases then with the distance from the equator of the Bloch sphere. In many interferometry schemes the phase ϕ_{r} is typically small, and it is therefore beneficial to perform the last $\frac{\pi}{2}$-pulse not around the y- but the x-axis. The expectation value is then $\langle J_z\rangle = J\sin\phi_{\mathrm{r}}$ and the projection noise $\Delta J_z = \sqrt{\frac{J}{2}}\cos^2\phi_{\mathrm{r}}$.

The same calculations can be repeated with entangled input states, where the expectation values and projection noise can be obtained with the help of the Wigner-D matrix introduced before. The unitary rotations from Equation (1.23) maintain the shape of Gaussian states. A particular problem for a SSS is that if after the interferometer operation the state is close to the poles of the Bloch sphere, the noise of a SSS is even larger than that of a CSS. In this case, the entangled state performs worse in the phase measurement than the uncorrelated state. A solution for this problem based on feedback control with weak measurements was proposed in [Borregaard 13b] and is discussed at the end of Chapter 4.

1.3. Generalized Quantum Measurements

1.3.1. Motivation

Without any specification, the term measurement in quantum mechanics usually refers to an ideal projective measurement. Here, one starts with a quantum system about which some *a priori* information may or may not be available, and one determines a property by a precise measurement. Since the quantum system possesses with certainty the measured property after the measurement, the *a posteriori* quantum state is then in a state both in conformity with the *a priori* knowledge and the measurement result. If the quantum state is measured again, the same measurement result will be obtained.

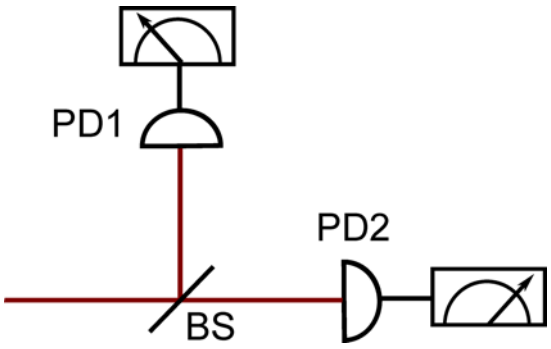

Figure 1.5.: A simple which-path experiment. A single photon is in a superposition of two paths after a beamsplitter (BS). The measurement of the path of the photon by the two photodiodes PD1 and PD2 is not an ideal projective measurement because the photon is destroyed after the measurement and the photodiodes have a technical detection noise.

Although the above way is the standard procedure to define a measurement in quantum mechanics (its mathematical formulation is given below), this situation is never encountered in practice. As an example, consider the which-path experiment depicted in Figure 1.5. A single photons is prepared in a superposition of two paths with two photodiodes PD1 and PD2 for the detection. The photodiodes are connected to a counter and if in one of the two paths there is a "click" we could deduce that a photon arrived. However, the photon has been destroyed by the interaction with the photodiode, and it cannot be measured again. In addition, a photodiode is usually not a perfect detector, and has for example a quantum efficiency (the ratio of the generated charge carriers to photons) below one, and dark counts by thermally generated carriers. Even if a "click" is registered on one of the two counters, it cannot be ascertained that a photon has arrived. Also without the destruction of the photon, the photodetection is therefore not an ideal measurement.

A general way to describe a measurement has to take into account both the possible destructivity by the measurement and uncertainties in the state determination. Here, we will focus on the uncertainty in the state determination, because we treat later the destructivity for our collective spin systems phenomenologically. The understanding of general quantum measurements of collective spins will be the basis for the measurement based feedback control used in this thesis.

As before, a language close to the Kopenhagen interpretation of quantum mechanics is chosen, although phrases such as "collapse of the wavefunction" are omitted. This does not reflect a bias towards any interpretation, but is merely a practical choice to use formulations with which most physicists are comfortable with. In any case, it should be noted that with strong evidence quantum mechanics is a complete theory [Bell 64, Aspect 82, Weihs 98, Rowe 01], and that formal descriptions can be used without reference to any additional interpretation.

1.3.2. Ideal Projective Measurement

We recall at first the concept of an ideal projective measurements on a pure quantum state. It is characterized by so called projectors,

$$P_m = |m\rangle \langle m| \ , \tag{1.37}$$

where m is a measurement result and the vectors $\{|m\rangle\}$ span a basis of the Hilbert space of interest. The projector P_m can be applied to a quantum state $|\Psi_{\text{in}}\rangle$ to give

$$|\Psi_{\text{out}}\rangle = \frac{P_m |\Psi_{\text{in}}\rangle}{\sqrt{\langle \Psi_{\text{in}} | P_m | \Psi_{\text{in}} \rangle}} \tag{1.38}$$

$$= \frac{c_m}{|c_m|} |m\rangle \ , \tag{1.39}$$

where we have used the relation $|\Psi_{\text{in}}\rangle = \sum_m c_m |m\rangle$ in the final equality. The coefficients $c'_m s$ are the probability amplitudes of $|\Psi_{\text{in}}\rangle$ in the basis $\{|m\rangle\}$. In the limit where the basis becomes a continuous set, the coefficients $c'_m s$ correspond to the wavefunction of the state. The probability to obtain a measurement result m is

$$p(m) = \langle \Psi_{\text{in}} | P_m | \Psi_{\text{in}} \rangle \tag{1.40}$$

$$= |\langle m | \Psi_{\text{in}} \rangle|^2 \tag{1.41}$$

$$= |c_m|^2 \ . \tag{1.42}$$

This equation is also known as the Born rule, named after M. Born who obtained for its statistical interpretation of the wave-function the Physics Nobel prize in

1957. The expectation or average value for the measurement results m is then

$$E(m) = \sum_m mp(m) \tag{1.43}$$

$$= \sum_m m \langle \Psi_{\text{in}} | P_m | \Psi_{\text{in}} \rangle \tag{1.44}$$

$$\equiv \langle \Psi_{\text{in}} | O_m | \Psi_{\text{in}} \rangle \ , \tag{1.45}$$

where the definition of the observable for the physical property measured was used:

$$O_m = \sum_m m P_m \ . \tag{1.46}$$

In the definitions above, no conditions for the measurement process are needed, except that a measurement result m is obtained using an ideal measurement apparatus. We are ready to see now how the model of an ideal projective measurement can be extended to the case where the measurement is not performed with a projector as in Equation (1.39), but with a measurement which contains some uncertainty in the measurement result.

1.3.3. Generalized Measurement Operators

1.3.3.1. Definition

A general quantum measurement is defined by the general measurement operators M_m, where m is a measurement result. The state after the measurement is

$$|\Psi_{\text{out}}\rangle = \frac{M_m |\Psi_{\text{in}}\rangle}{\sqrt{\left\langle \Psi_{\text{in}} \left| M_m^\dagger M_m \right| \Psi_{\text{in}} \right\rangle}} \ , \tag{1.47}$$

and the probability to measure m

$$p(m) = \left\langle \Psi_{\text{in}} \left| M_m^\dagger M_m \right| \Psi_{\text{in}} \right\rangle \ . \tag{1.48}$$

The probabilities should all sum to unity, i.e.

$$1 = \sum_m p(m) \tag{1.49}$$

$$= \sum_m \left\langle \Psi_{\text{in}} \left| M_m^\dagger M_m \right| \Psi_{\text{in}} \right\rangle \ , \tag{1.50}$$

which is equivalent to require

$$\sum_m M_m^\dagger M_m = I \ , \tag{1.51}$$

where I denotes the identity operator.

1.3.3.2. Example

Consider a two level system prepared in the input state

$$|\Psi_{\text{in}}\rangle = \frac{1}{\sqrt{2}} \left(|0\rangle + |1\rangle \right) \ . \tag{1.52}$$

We consider the two measurement operators

$$M_0 = \sqrt{p}\, |0\rangle \langle 0| + \sqrt{1-p}\, |1\rangle \langle 1| \,, \tag{1.53}$$

$$M_1 = \sqrt{1-p}\, |0\rangle \langle 0| + \sqrt{p}\, |1\rangle \langle 1| \,. \tag{1.54}$$

The operator M_0 (M_1) is applied when the measurement result $m = 0$ ($m = 1$) is obtained. The form of the measurement operators reflects a situation where a measurement result m is obtained but the measurement system has an intrinsic uncertainty. The factor $1-p$ then corresponds to the probability of a measurement error. The measurement operators fulfill the completeness condition $M_0^\dagger M_0 + M_1^\dagger M_1 = I$. The state after a measurement result $m = 0$ is

$$|\Psi_{\text{out}}\rangle = \frac{M_0 |\Psi_{\text{in}}\rangle}{\sqrt{\left\langle \Psi_{\text{in}} \left| M_0^\dagger M_0 \right| \Psi_{\text{in}} \right\rangle}} \tag{1.55}$$

$$= \sqrt{p}\, |0\rangle + \sqrt{1-p}\, |1\rangle \ . \tag{1.56}$$

The state is therefore partially projected by the partial information from the measurement. In an interesting scenario, another measurement on the state is per-

formed and the result is $m = 1$. The output state is then

$$|\Psi'_{\text{out}}\rangle = \frac{M_1 |\Psi_{\text{out}}\rangle}{\sqrt{\left\langle \Psi_{\text{out}} \left| M_1^\dagger M_1 \right| \Psi_{\text{out}} \right\rangle}} \tag{1.57}$$

$$= \frac{1}{\sqrt{2}} (|0\rangle + |1\rangle) \ , \tag{1.58}$$

which is same as the input state $|\Psi_{\text{in}}\rangle$. The presented case where performing a measurement can remove the partial projection of a state is known under the name "weak measurement reversal" (see e.g. [Ueda 92, Katz 08]).

1.3.3.3. Relation to Bayes Theorem

Note that the probability amplitudes are very similarly treated in a general quantum measurement as one would update the probability of a classical system. In fact, the principle is the same, only that in one case the information about probabilities and in the other case about probability amplitudes is updated. It appears natural for the estimation of a parameter to take the probabilities from the *a priori* knowledge of a system, and multiply them with the probabilities from a new estimate. Normalization gives then the *a posteriori* probability distribution. This is common practice for the determination of errors and can be formalized writing

$$p(x, y) = p(x|y)p(y) = p(y|x)p(x), \tag{1.59}$$

where $p(x, y)$ is the joint probability to have both x and y and $p(x|y)$ and $p(y|x)$ are conditional probabilities. A simple rearrangement of Equation (1.59) leads to Bayes theorem

$$p(x|y) = \frac{p(y|x)p(x)}{p(y)} \ , \tag{1.60}$$

where

$$p(y) = \int_{-\infty}^{\infty} p(y|x)p(x)dx \ . \tag{1.61}$$

Bayes theorem tells how the state of knowledge of the variable x, represented by the probability distribution $p(x)$ is updated. A measurement gives new data y, and in order to change our knowledge about x, we have to know how y is related to x. This relationship is usually known in practice. If for example x is a position and y is the measured position with a Gaussian uncertainty, then $p(y|x)$ is peaked at x and has a Gaussian shape. Inserting this in Equation (1.60) gives then the

a posteriori knowledge of x. The general measurement law in Equation (1.47) is therefore nothing else than the Bayes theorem applied to state vectors with probability amplitudes. An ideal projective measurement is analogous to the case where $p(y|x)$ is a delta function.

1.3.3.4. Extension to Density Operators

State vectors are intrinsically probabilistic in nature because they can be expressed as superposition of quantum states with different probability amplitudes. There exists, however, the possibility that for a quantum system there are only information available about its classical probabilities to be in a certain state[5]. We assume that we have an ensemble of states $|\Psi_k\rangle$, which were prepared with different probabilities p_k, with $\sum_k p_k = 1$. For each state the conditional probability to measure a result m is

$$p(m|k) = \left\langle \Psi_k \left| M_m^\dagger M_m \right| \Psi_k \right\rangle \tag{1.62}$$

$$= \sum_k \left\langle k \left| M_m^\dagger M_m \right| \Psi_k \right\rangle \langle \Psi_k | k \rangle \tag{1.63}$$

$$= \mathrm{tr}\left(M_m^\dagger M_m \left| \Psi_k \right\rangle \langle \Psi_k | \right) \ , \tag{1.64}$$

where we have used the definition for a trace. The total probability $p(m)$ is

$$p(m) = \sum_k p(m|k) p_k \tag{1.65}$$

$$= \sum_k p_k \mathrm{tr}\left(M_m^\dagger M_m \left| \Psi_k \right\rangle \langle \Psi_k | \right) \tag{1.66}$$

$$= \mathrm{tr}\left(M_m^\dagger M_m \rho \right) \ , \tag{1.67}$$

where the density operator ρ is introduced

$$\rho = \sum_k p_k \left| \Psi_k \right\rangle \langle \Psi_k | \ . \tag{1.68}$$

Even though the density operator is an operator in its nature, it contains all information available about a quantum system. A general measurement can be treated as if the measurement operator acts on each state $|\Psi_k\rangle$ singularly, and we

[5] The distinction between probability amplitudes and probabilities is clear in a mathematical formulation, but harder to express in words. In general, the two can be distinguished by the property that probability amplitudes can lead to interference.

can therefore write

$$\rho_{\text{out}} = \sum_k p(k|m) \frac{M_m |\Psi_k\rangle \langle\Psi_k| M_m^\dagger}{\left\langle \Psi_k \left| M_m^\dagger M_m \right| \Psi_k \right\rangle} \tag{1.69}$$

$$= \sum_k \frac{M_m \rho_{\text{in}} M_m^\dagger}{\text{tr}\left(M_m^\dagger M_m \rho\right)} , \tag{1.70}$$

where Equation (1.64) and Equation (1.59) were used. The operators in M_m could be in principle replaced by any other set of operators satisfying the completeness relation (and so the conservation of the total probability). The measurement operators are therefore only a special case of a more general class of operators, called Kraus operators [Kraus 71, Kraus 83]. A map from one density operator to another one is then called a quantum channel which gives a general mean to describe any evolution of a quantum system. A unitary evolution is also a special case of such an evolution, with

$$\rho_{\text{out}} = U \rho_{\text{in}} U^\dagger . \tag{1.71}$$

In the case of a general quantum measurement, it is possible that not the full form of the Kraus operators M_m is known, but only the probabilities of the measurement results. This is expressed by the operators $E_m = M_m^\dagger M_m$, which are non-negative and Hermitian, and form a so called positive-operator valued measure (POVM). To each probability operator E_m of the POVM several different measurement operators M_m and therefore output states can correspond. With the probability operators, a quantum measurement can be expressed without the knowledge of the all details of the measurement process.

1.3.3.5. General Quantum Measurements of Collective Spin States

Our target is to measure the population difference of a CSS along the z-axis of the Bloch sphere, which is the observable variable in atom interferometry. In the limit of $J \gg 1$, we have shown that the state in the Dicke basis is given by

$$|\Psi_{\text{in}}\rangle = |\theta, \phi\rangle = \sum_{m=\_J}^{J} c_m(\theta) e^{-i(J+m)\phi} |J, m\rangle , \tag{1.72}$$

with

$$c_m = \frac{1}{\sqrt{\sqrt{\pi J}\sin\theta}} e^{-\frac{(m-J\cos\theta)^2}{2J\sin^2\theta}} \ . \tag{1.73}$$

The projector in this basis is

$$J_z = |J,m\rangle \langle J,m| \ . \tag{1.74}$$

We assume that the measurements are nondestructive, i.e. the system remains in a pure state after the measurement. Furthermore, we assume that the measurement has a Gaussian uncertainty with a value σ_{det} with respect to the full spin length J. The situation is then similar to measuring the position on a ruler with a bad vision. From the probability distribution of the measurement itself, we know the form of $M_m^\dagger M_m$, and taking the square root for the probability amplitudes leads to

$$M_m = \left(2\pi\sigma_{\text{det}}^2\right)^{-1/4} e^{-\frac{1}{4\sigma_{\text{det}}^2}(J_z-m)^2} . \tag{1.75}$$

When the measurement operator is applied on the CSS from Equation (1.72), one obtains the output state

$$|\Psi_{\text{out}}\rangle = \frac{M_{m_0}|\Psi_{\text{in}}\rangle}{\sqrt{p(m_0)}} \tag{1.76}$$

$$= \left(2\pi\xi^2 J\sin^2\theta\right)^{-1/4} \sum_{m=\_J}^{J} e^{-\frac{(m-\mu_0)^2}{2\xi^2 J\sin^2\theta}} e^{-i(J+m)\phi} |J,m\rangle \ . \tag{1.77}$$

The index m_0 in Equation (1.77) was introduced to distinguish a specific measurement result from the variable m for the state vectors. The other variables are the squared squeezing factor

$$\xi^2 = \frac{1}{1+\kappa^2\sin^2\theta} \ , \tag{1.78}$$

the squared measurement strength

$$\kappa^2 = \frac{\sigma_{\text{J}}^2}{\sigma_{\text{det}}^2} \tag{1.79}$$

$$= \frac{J}{4\sigma_{\text{det}}^2}, \tag{1.80}$$

and the peak position of the Gaussian distribution after the measurement

$$\mu_0 = \frac{\kappa^2 \sin^2\theta m_0 + J\cos\theta}{1+\kappa^2\sin^2} \,. \tag{1.81}$$

The probability of a measurement result m_0 is

$$\begin{aligned} p\left(m_0\right) &= \langle\theta,\varphi|\, M_{m_0}^{\dagger} M_{m_0}\, |\theta,\varphi\rangle & (1.82)\\ &= \frac{1}{\sqrt{2\pi}}\frac{\xi_\theta}{\sigma_{\mathrm{det}}} \exp\left[-\frac{\xi_\theta^2\left(m_0 - J\cos\theta\right)^2}{2\sigma_{\mathrm{det}}^2}\right] \,. & (1.83) \end{aligned}$$

The definition for the measurement strength is related to the situation when a CSS is prepared on the equator of the Bloch sphere. In this case, the state after the measurement is

$$|\Psi_{\mathrm{out}}\rangle = \left(2\pi\frac{1}{1+\kappa^2}J\right)^{-1/4} \sum_{m=_-J}^{J} e^{-\frac{\left(m-\frac{\kappa^2}{1+\kappa^2}m_0\right)^2}{2\frac{1}{1+\kappa^2}J}} e^{-i(J+m)\phi}\,|J,m\rangle \,. \tag{1.84}$$

The measurement strength κ is the ratio of the size of the initial Gaussian wavefunction for a CSS on the equator of the Bloch sphere to the uncertainty of the measurement. The squeezing factor ξ is the ratio of the sizes of the new and the old wavefunction. With an increasing precision of the measurement, the measurement strength increases and the quantum noise of the output state in the measured direction is reduced.

The measurement process can be nicely illustrated by considering only the absolute value of the wavefunction as depicted in Figure 1.6. The wavefunction after the measurement is simply the initial wavefunction multiplied with another function defined by the measurement operator Equation (1.75). It seems reasonable to call this function "measurement function" in analogy to the term wavefunction[6]. At every position m one then has to multiply the probability amplitudes of the wavefunction and the measurement function. Finally, one normalizes the result by requiring that the total probability of the output wavefunction is equal to 1. In the same spirit, the probability distribution of the measurement results is the

[6] We only became later aware of the already existing formalism for generalized quantum measurements, and derived the above results without this knowledge. The term "measurement function" was very useful in the discussions with the team members, and it is proposed here to keep it for the future.

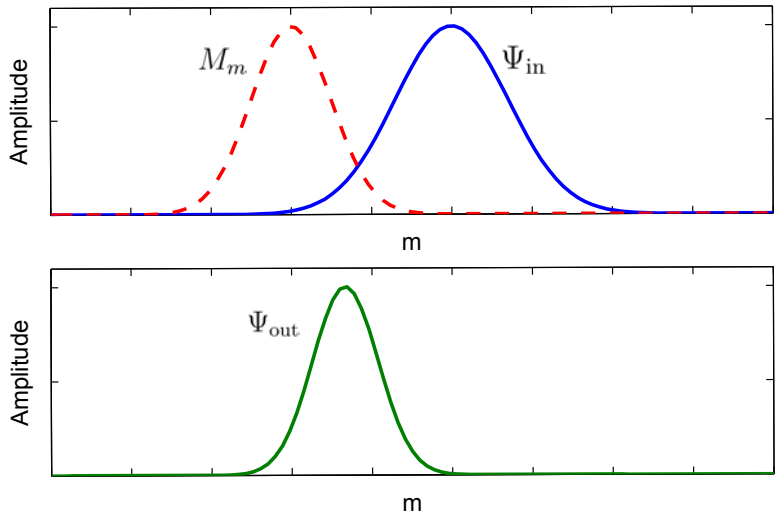

Figure 1.6.: Illustration of a general quantum measurement with Gaussian variables. The wavefunction Ψ_{out} after the measurement is simply the multiplication of the initial wavefunction Ψ_{in} and the measurement function M_m (with a final normalization).

squared convolution of the measurement function and wavefunction.

The situation where a CSS is prepared on the equator of the Bloch sphere and undergoes a partial projection is the basic procedure to generate a spin-squeezed state by a nondestructive measurement. The Wineland criterion (Section 1.2.3) is then given by

$$\xi_S^2 = \frac{2J\left(\Delta J_\perp\right)^2}{|\langle \mathbf{J}\rangle|^2} = \frac{\xi^2 J^2}{|\langle \mathbf{J}\rangle|^2} = \frac{\xi^2}{\eta_{\text{coh}}^2}\,, \tag{1.85}$$

where $\eta_{\text{coh}} = \frac{|\langle \mathbf{J}\rangle|}{J}$ accounts for the possible decoherence during the measurement process. Another property is that from Equation (1.84) the expectation value for a next measurement is $\epsilon m_0 = \frac{\kappa^2}{1+\kappa^2} m_0$. The variable ϵ is therefore the correlation coefficient between two successive measurements on the same axis on a CSS.

Partial projective measurements are an interesting tool to prepare entangled states for metrology. Nevertheless, we take in this manuscript a different path and explore the active control of quantum states in atomic interferometers. The projectivity of the quantum measurements can in this case be a disadvantage. For example, consider the case of an ideal projective measurement. It prepares a Dicke

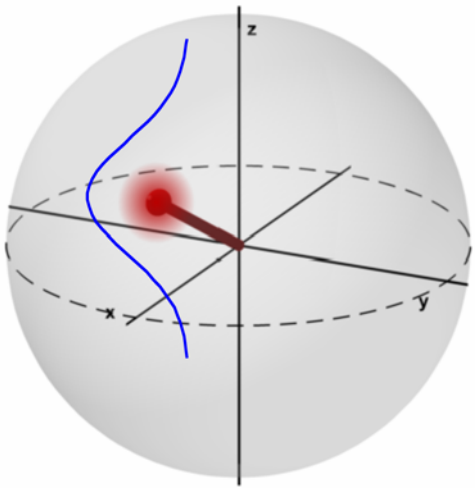

Figure 1.7.: Weak measurement of a collective spin. Although the uncertainty of the measurement is larger than the projection noise, still the mean spin direction can be determined. If the measurement is nondestructive the spin state is preserved.

state, which has no mean spin direction and can therefore not be read out with the standard Ramsey scheme introduced before. Furthermore, the projectivity of the measurements is in practice linked to their destructivity. In our experiment this will be the case with the number of photons in the optical beam to probe the atoms. To both reduce the projectivity and the destructivity, we can choose the parameter range

$$\frac{1}{2J} < \kappa^2 \ll 1 \,, \qquad \xi \approx 1 \,, \qquad \epsilon \approx 0 \,. \tag{1.86}$$

The situation is illustrated in Figure 1.7: even though the uncertainty of the measurement is much larger than the size of the atomic projection noise, it is still possible to obtain information about the population difference. The state after the measurement is

$$|\Psi_{\text{out}}\rangle \approx |\Psi_{\text{in}}\rangle \,. \tag{1.87}$$

Collective quantum states such as a CSS therefore have the interesting property that valuable information about them can be obtained while the state remains basically unchanged. We can therefore obtain information with almost no cost, unlike in most other situations with quantum systems. The precision to which a population difference can be measured goes as $\frac{\sigma_{\text{det}}}{J} \to 0$ for $J \to \infty$.

We call such measurements where the uncertainty of the measurement is larger than the uncertainty of the state "weak measurements". This term has been introduced in connection to schemes where at first one performs on a quantum system a weak (almost non-projective) measurement, and subsequently a strong projective measurement [Aharonov 88]. When the results are postselected according to the results of the strong final measurements, unexpected predictions about the results of the weak measurements can be made[7]. In particular, one comes to the non-intuitive result that the weak intermediate measurement could find a spin which is systematically larger then the length of the real spin (see [Aharonov 10] for a good explanation of this effect). Such "weak value amplification" schemes have been used for the measurement of tiny physical effects [Hosten 08, Dixon 09]. Nevertheless, the question of whether weak value amplification can lead to a gain in metrology is still open [Knee 13, Jordan 13, Ferrie 13]. In Appendix A an example for weak measurements with postselection is given.

Weak measurements in the sense of Equation (1.86) will be a central tool in this manuscript. They will be used in combination with feedback control to protect collective spin states against a typical form of decoherence in atomic interferometers. On this basis, we develop and demonstrate a feedback protocol to increase the interrogation time in atomic interferometers.

1.3.3.6. Relation to Quantum Non-Demolition Measurements

It should be noted that in the discussion in this chapter, no assumptions on the measurement process itself were made. We have seen that such assumptions are not required, and any quantum measurement can be completely described by the information gain and the general measurement operators M_m. However, there is the question of how a nondestructive measurement can be performed in practice. The strategy is usually to use an indirect measurement. Here, an auxilary "meter" quantum system interacts and is entangled with the "signal" quantum system. The meter can then be destroyed and its information content treated with a classical apparatus. Because the meter and the signal were entangled by the interaction, the signal quantum system is then fully or partially projected. Such kind of measurement schemes were at first devised by J. von Neumann [von Neumann 96], and conditions for quantum non-demolition (QND) measurements were given

[7] In the community of quantum optics, the term "weak measurement" is often used equivalently for the case of a weak measurement with postselection, which leads to semantic problems. To make the distinction, it could be better to call the latter "weak value measurement".

in [Braginsky 80]. In [Grangier 98], criteria to evaluate the quality of the QND measurements are given.

We assume that the total Hamiltonian of the system is $H = H_S + H_M + H_{MS}$, where H_S is the Hamiltonian of the system, H_M is the Hamiltonian of the meter and H_{MS} is the interaction Hamiltonian between the system and the meter. Furthermore, we call the observables of the system and of the meter A_S and A_M, respectively. We have then the following three requirements for a QND measurement. At first, the meter has to interact with the quantum system,

$$[H_{MS}, A_M] \neq 0 \ , \tag{1.88}$$

the interaction between the meter and the signal should not change the signal,

$$[H_{MS}, A_S] = 0 \ , \tag{1.89}$$

and the observable should be conserved under free evolution,

$$[H_S, A_S] = 0 \ . \tag{1.90}$$

In practice, the first and last condition are easily fulfilled, whereas the second condition is problematic. It implies that the meter should not cause any decoherence on the signal at all. Experiments with close to no destructivity and variable measurement strength were so far performed on photons in a microwave cavity [Guerlin 07] and on superconducting qubits [Hatridge 13].

Nondestructive measurements on the internal state of atoms are usually performed by the dispersive probing with off-resonant light on an atomic transition. There is always a contribution from spontaneous emission and the condition $[H_{MS}, A_S] = 0$ can therefore not be strictly fulfilled. However, within the scientific community, it has become common practice to take the Wineland criterion as a benchmark for a QND measurement on collective spin states. If a CSS can be squeezed according to the Wineland criterion, then the nondestructive measurement can be called a quantum non-demolition measurement. Since in our experimental setup we cannot fulfill the Wineland criterion, we use in the following chapters the term nondestructive measurements to describe our detection system.

2. Preparation of Cold Atomic Samples

2.1. Introduction

In this chapter, our procedure to prepare a large coherent ensemble of two-level atoms is described. Coherence can refer for an atomic cloud to the internal states, the external states, or both. In atomic clocks, mainly the internal state purity is of interest. In a matter-wave Bragg interferometer, only the external states are manipulated, and therefore an atomic sample should be as cold as possible and preferably be without atomic interactions. In a Raman interferometer, both the internal and external states are equally crucial. Nevertheless, since in most interferometers the internal and external states of the atoms can couple to each other, we aim to achieve at the same time a high purity both of the internal and external states.

In its initial orientation, our experimental setup was designed as a compact prototype for matter-wave experiments, combined with a nondestructive detection system for the atoms. We work with the atomic species ^{87}Rb, which is routinely used for cold atom experiments in laboratories around the world, and for which first companies sell dedicated products[1]. The focus in this chapter is therefore on the non-standard experimental solutions we have chosen for our setup.

A unique feature in our experimental setup is an optical cavity with mirrors arranged in a butterfly configuration, presented in Section 2.3. The optical cavity stores and therefore enhances the field derived from a telecom laser at 1560 nm. The light in the cavity is used as an optical trap for the atoms, and because of the power enhancement of the cavity less laser power is needed for the same depth of the trap. A detailed description of the vacuum system for the atoms, the magneto-optical trap and the optical cavity was already given in the PhD thesis of Simon Bernon [Bernon 11a], and I will therefore only highlight the

[1] One company, Quantel, used our setup to test one of their laser systems especially designed for the cooling of ^{87}Rb. Another company, ColdQuanta, sells even an entire setup for the production of cold atomic clouds.

main characteristics here (Section 2.2 and Section 2.3). To use the the optical cavity, the frequency of the dipole trap laser has to be kept on resonance with the cavity via a feedback system. We developed a new method for such a stabilization system based on serrodyne frequency shifting as described in Section 2.3.4.

One of our first goals with the experimental setup was to obtain a Bose-Einstein condensate with the help of the cavity-enhanced light field, and our results are shown in Sections 2.4 and 2.5. For our experiments with the nondestructive detection system we were only interested in the internal states of the atoms. Because of their higher atom number we therefore chose to continue our work with trapped thermal clouds with a temperature of around 10 μK.

The optical dipole trap at 1560 nm causes a large light shift on the optical transitions used to probe the atoms. In Section 2.6, we describe a compensation method which cancels this large light shift with an auxiliary laser at 1529 nm. This allows us to treat the optical transitions of ^{87}Rb as if the atoms would be probed in free space. Since we worked with a very dense atomic cloud, multiple scattering of light did not allow us to use a conventional technique for the preparation of the internal atomic states. In the last part of this chapter (Section 2.6.2), we show how we dealt with this problem and describe our state preparation method. The trapped atomic ensembles with no differential light shift on the optical transitions are then the basis for the work in the succeeding chapters.

2.2. Vacuum System and Magneto-Optical Trap

Cold atoms must me hold in ultra high vacuum to avoid their random interaction with the environment. This prevents heating of the atoms or random changes of their internal atomic states. To obtain a cold atomic cloud with a high atom number and a long lifetime, we use the vacuum system shown in Figure 2.1. It consists of two chambers, one to cool atoms from the background pressure of a solid sample of ^{87}Rb, and one for the storage of the atoms in ultra high vacuum.

The first vacuum chamber contains a two dimensional magneto-optical trap (2D MOT) and the second chamber a three dimensional magneto-optical trap (3D MOT) and a dipole trap enhanced by an optical cavity. In the second chamber the experiments are performed and it is called the science chamber. The pressure in the 2D MOT chamber is below 10^{-7} mbar and in the science chamber below

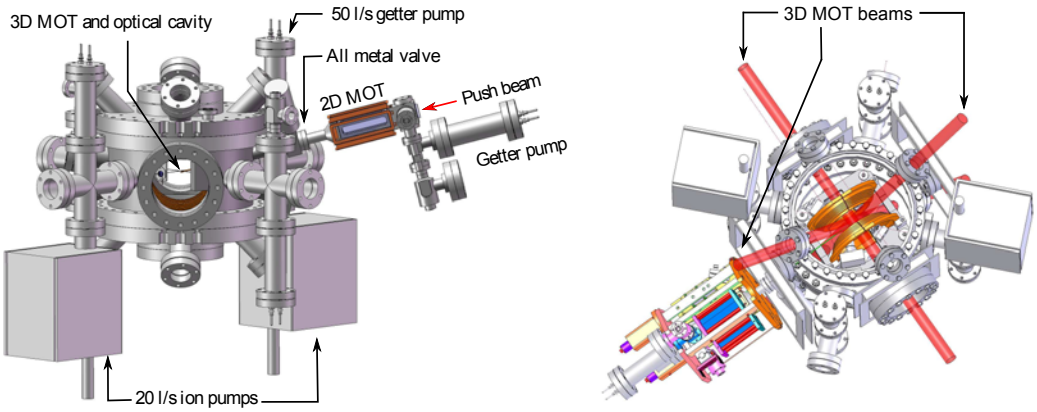

Figure 2.1.: Side (a) and bottom (b) view of the vacuum system with the 2D MOT and the science chamber. The 2D MOT is used to load fast the 3D MOT which is placed at the center of the crossed optical cavity.

10^{-9} mbar. The vacuum is maintained in the science chamber thanks to a 50 l/s getter pump and two 20 l/s ion pumps.

The purpose of a MOT is both to cool and to trap atoms. The 2D MOT and 3D MOT use laser Doppler cooling of ^{87}Rb with radiation at 780 nm, derived from extended cavity diode lasers (ECDLs, 300 kHz linewidth). Doppler cooling relies on the red-detuning of the laser beams from an optical transition ($F = 2 \rightarrow F' = 3$, see level scheme in Figure 2.2(a)), such that because of the Doppler effect only atoms which move in the direction of the laser absorb light. Since the spontaneous emission from the atoms is isotropic in space, the full cycle of absorption and reemission results in a net reduction in the atomic velocity, and therefore cooling[2].

A magnetic gradient is applied with coils in anti-Helmholtz configuration and the cooling light is circularly σ_+/σ_- polarized (see Figure 2.2(b)). Since the Zeeman-sublevels of the optical transition are more shifted in resonance with the laser when leaving the trap center, a magneto-optical trap is formed[3]. The atoms

[2]Doppler cooling has been simultaneously proposed by D. J. Wineland and H. G. Dehmelt [Wineland 75] and T. W. Hänsch and A. L. Schawlow [Hänsch 75]. It was first demonstrated by D. J. Wineland, R. E. Drullinger and F. L. Walls [Wineland 78].

[3]More details for the operation of an magneto-optical trap can be found in numerous PhD theses, books and review articles, see e.g. [Adams 97].

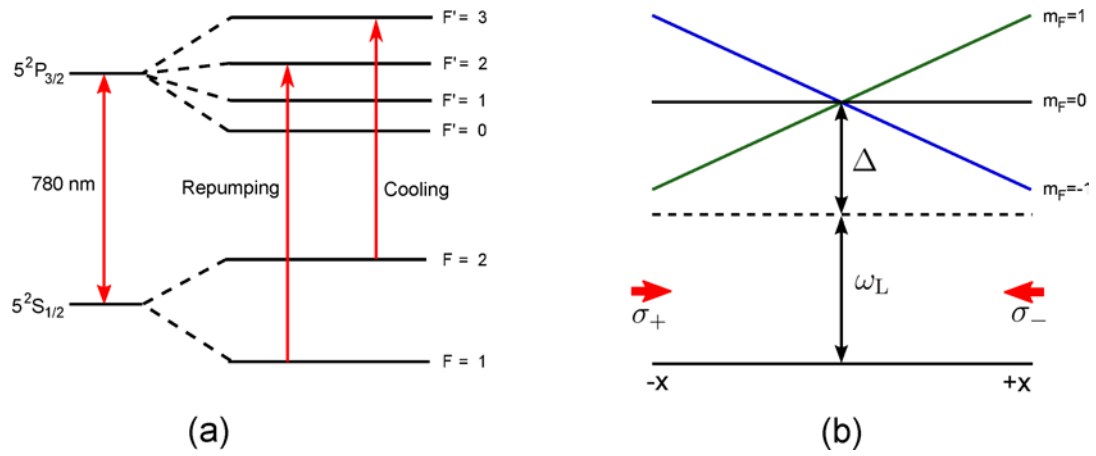

Figure 2.2.: (a) Level scheme on the D2 line of ^{87}Rb. A more detailed level scheme is given in Appendix B. (b) Operation principle of a MOT. The atomic levels are shifted closer to resonance of the laser light when they leave the trap center.

are confined in vacuum.

In our experiment, the 2D MOT serves as a source of atoms to load fast and efficiently the 3D MOT. It is loaded from the background vapor pressure of a solid rubidium sample which had an initial mass of 1 g at the construction of the experiment. The atoms are cooled down from 2 orthogonal directions, with a total cooling laser power of 100 mW and detuned by 2.5 times the linewidth $\Gamma = 6.07$ MHz[4] from the $F = 2 \rightarrow F' = 3$ transition. The cooling transition is in principle a closed transition, but the cooling light can also off-resonantly excite the state $F' = 2$ which is 267 MHz to the red of the $F' = 3$ state. From $F' = 2$ the atoms can decay and accumulate in $F = 1$, which is not addressed by the cooling radiation. To pump the atoms back to $F = 2$, repump light on the $F = 1 \rightarrow F' = 2$ transition is added to the MOT beams.

We frequency lock the repump laser on the $F = 1 \rightarrow F' = 1, 2$ cross-over and shift it with an AOM on the $F = 1 \rightarrow F' = 2$ atomic transition. The cooling laser is frequency offset locked on the repumper. The servo control relies on an optical phase locked loop (PLL), which allows to continuously frequency shift the cooling laser frequency over a range of 400 MHz. This is later used in the loading of the

[4]Throughout this thesis the convention $\Gamma = 6.07$ MHz is used. Note that e.g. in [Steck 01] instead $\Gamma = 2\pi \times 6.07$ MHz

dipole trap from the 3D MOT. The repump laser is superimposed with all cooling beams in the 2D and 3D MOT. All laser beams are prepared on a separated optical table and transported to the setup via optical fibers.

The 2D MOT loads the 3D MOT with a rate of about 5×10^8 atoms per second, guided by a push beam of 2 mW power. The magnetic field of the 3D MOT has a gradient of 7.7 $\mathrm{G\,cm^{-1}}$, and there are six beams on three orthogonal axis of the MOT for the cooling (Figure 2.2(b)). Each beam has an optical power of about 8 mW and is in addition retro-reflected to recycle the light for a higher effective laser power. The atomic cloud reaches its maximal size with typically 10^9 atoms after about 2 s loading time. The lifetime of the atoms in the 3D MOT is 20 s as measured with fluorescence after switching off the 2D MOT.

2.3. Cavity Enhanced Optical Dipole Trap

2.3.1. Motivation for Optical Cavity

The temperature limit in a 3D MOT for rubidium atoms is the Doppler limit

$$T_D = \frac{\hbar\Gamma}{2k_b} = 146\ \mu\mathrm{K}\ , \tag{2.1}$$

which is due to the random walk from spontaneous emission. In general, we would prefer to work with atomic clouds of lower temperatures. Furthermore, the atoms cycle incoherently between $F = 2$ and $F' = 3$, which prevents experiments based on coherent manipulations of the internal states. To gain a better control of the internal states and to further decrease their temperature, the atoms can be loaded in a conservative potential. Cooling can for example then be achieved by suitably lowering the potential barriers. Here, similar as in the evaporation in a coffee cup, atoms with high energies escape the trap. After thermalization the overall temperature of the remaining atoms is decreased[5].

For neutral atoms, there are typically two choices for the conservative trap, either a magnetic trap or an optical dipole trap. A magnetic trap has the advantage that the trap barriers can be lowered without reducing the trap frequency,

[5] see [Ketterle 96] for a good review article about the history and physical principles of the evaporative cooling of atoms.

which leads to a more effective evaporation process. On the other hand it has the disadvantage that internal magnetic states of the atoms cannot be manipulated independently. Furthermore, magnetic traps can introduce systematic errors for matter wave sensors because of residual magnetic fields during the propagation of the atoms in the interferometer.

We therefore decided in our experiment to load the atoms in an optical dipole trap. The wavelength of the dipole trap was chosen at 1560 nm because of the availability of a variety of telecom lasers at this wavelength[6]. Telecom lasers at 1560 nm have very favorable linewidth characteristics (down to a few KHz), and several fibered optical components at this wavelength are available with which robust optical setups can be built [Ménoret 11]. In addition, the light at 1560 nm can be doubled to obtain lasers with a narrow linewidth at 780 nm. As a disadvantage, the optical power of the lasers at 1560 nm is comparably low, and commercially available erbium doped fiber amplifiers (EDFA) can deliver at the moment only up to a few tens of W of optical power. To overcome this limitation, we decided to use the power enhancement in an optical cavity.

2.3.2. Geometrical Description

For the design of the optical cavity, a configuration with four mirrors on a square with a diagonal of 90 mm was chosen as seen in Figure 2.3.

With the four mirrors, the light can travel along a butterfly shape in the optical cavity and the cavity arms cross in the middle. Each laser beam gives a tight confinement along its transverse directions and the crossing leads to a high trap depth in three dimensions. Because of the crossing angle of 90° and because the polarization is chosen to be in the cavity plane, there is no interference of the beams at the cavity center. The injection of laser light at one input port gives rise to a running wave configuration and there is no standing wave as in a Fabry-Perot cavity.

Each mirror is plane concave with a curvature of $R = 100$ mm and has a diameter of 1/2 inch. As shown in Figure 2.3, the MOT coils are directly mounted on the titanium plate of the optical cavity. This is of advantage for a steep magnetic gradient, but has the disadvantage that changes in the magnetic field lead to

[6]The wavelength range from 1530 nm to 1565 nm is called in fiber communications the C band and benefits from the low losses of silica optical fibers in this region.

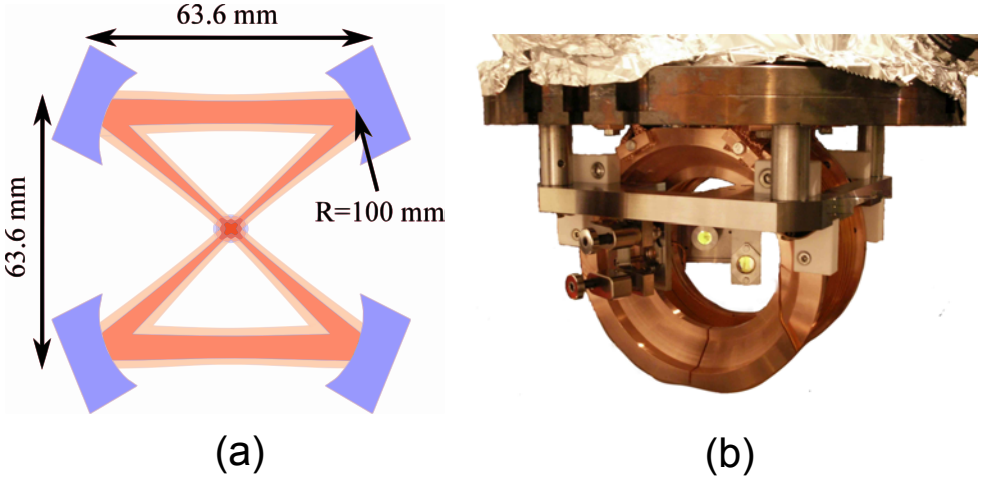

Figure 2.3.: (a) Scheme of the optical cavity and (b) experimental implementation with surrounding MOT coils

correlated changes of the cavity length.

2.3.3. Optical Properties

An optical cavity can be considered as a reservoir of light which is continuously pumped from the outside and leaking through the output mirrors. To determine completely the properties of the dipole trap in the cavity, one has to know the intracavity field and the optical beam waists in the cavity crossing. The beam waists are imposed by the cavity size, the curvature of the mirrors and the wavelength at 1560 nm. The calculation with the ABDC formalism of Gaussian beams[7] gives a beam waist of $w_{\parallel} = 93.1$ μm in the cavity plane and $w_{\perp} = 129.8$ μm in the vertical direction.

The field build-up in the optical cavity results from the constructive interference of the input light with the intracavity light. It occurs therefore only at distinct frequencies, separated by the free spectral range (FSR). The FSR of our cavity is 976.2 MHz, which has been measured by injecting both the carrier and the frequency sidebands generated with an electro-optical modulator (EOM) into adjacent fundamental modes of the cavity. The value is consistent with

[7] A review article about the ABCD formalism of Gaussian beams applied to optical resonators can be found in [Kogelnik 66]. The calculation for our optical cavity is described in the PhD thesis of Simon Bernon [Bernon 11a].

Property	Value
Finesse F	1788
Free spectral range (FSR)	976.2 MHz
Beam waist $w_{\parallel}$	93.1 μm
Beam waist $w_{\perp}$	129.8 μm
Ratio $P_{\text{intra}}/P_{\text{out}}$	2800

Table 2.1.: Summary of the optical properties of the crossed optical cavity at 1560 nm. P_{intra} is the power in one cavity arm and P_{out} the power at one cavity output

FSR = c/L, where $L = 30.73$ cm is the total travel length inside the optical cavity. The linewidth of a cavity indicates the rate at which the cavity field decays and the full-width half-maximum (FWHM) linewidth at at 1560 nm is for our cavity $\gamma = 546$ kHz. The finesse is therefore $F_{1560} = \text{FSR}/\gamma = 1788$. Divided by π it corresponds to how many cycles a photon travels on average in the cavity before it leaves it.

A perfect Fabry-Perot cavity consists of two mirrors with the same reflectivity and its power enhancement factor is $\eta_{\text{FP}} = 2F/\pi$. The optical power inside the cavity can be therefore directly deduced from the input power. In our cavity in butterfly configuration, the condition that all incoming light interferes constructively with the light in the cavity is not fulfilled and a major part of the incoming light on the cavity is reflected. An additional difficulty is that there are three outputs ports instead of one. A practical method therefore is for a complex cavity to measure the optical power at one output port and then deduce from this the intracavity power. We assume that each mirror in the optical cavity is identical and

$$R + D + T = 1 \,, \tag{2.2}$$

where R is the mirror reflectivity, T is the transmission and D are diffusive losses. The cavity finesse for a symmetrical four mirror cavity is given by

$$F = \frac{\pi R}{1 - R^2} \,. \tag{2.3}$$

Further, by definition of the transmission T we have that the output power of the

cavity is

$$P_{\text{intra}} = \frac{1}{T} P_{\text{out}} \ . \tag{2.4}$$

Using the definition $x = D/T$ and inserting Equation (2.2) and Equation (2.3) in Equation (2.4) one arrives then at

$$P_{\text{intra}} = \frac{2F}{\pi}(1+x) P_{\text{out}} \ . \tag{2.5}$$

The measurement of the intracavity power for a given input power has been performed with the light shift method described in [Bertoldi 10], which gave $P_{\text{intra}}/P_{\text{out}} = 2800$ and so $x = 1.46$.

For the dipole trap, a distributed feedback erbium doped fiber laser (DFB EDFL, Koheras, from NKT Photonics) was used which was amplified with an EDFA to 5 W. We obtained typically a coupling efficiency of $25\% - 30\%$, close to the largest theoretically possible value of $35(2)\%$. As a maximum value, we could reach an intracavity power of 200 W, sufficiently enough to trap and further cool down the atoms.

2.3.4. Laser Stabilization by Serrodyne Modulation

2.3.4.1. Motivation

The frequency of the dipole trap laser has to be kept on a resonance of the optical cavity to optically pump it. However, the resonator is subject to fluctuations from the environment and therefore the cavity resonances drift. The same holds for the laser frequency which is in general not stable over time. We therefore have to stabilize either the frequency of the laser on the optical cavity or the other way around.

The relative frequency fluctuations between the dipole trap laser and a resonance of the optical cavity should be kept as small as possible, and the laser should never unlock from the cavity. A crucial parameter for this is the bandwidth of the actuator used to apply frequency corrections. The bandwidth, and so the speed of the actuator should be always above the frequencies of the dominating noise sources and in general be as big as possible. This rules out feedback on the mirrors of our optical cavity, because the mirrors are to heavy and allow only a correction bandwidth of a few tens of Hertz. We therefore perform feedback on the laser frequency.

For a large class of lasers, such as fiber or diode pumped solid state lasers, the only possibility to act directly on the laser frequency is on their piezo-electric transducers (PZT). The correction bandwidth is here only a few kHz. Higher bandwidths can be achieved with an external frequency actuator, which is typically an acousto-optical modulator (AOM). It is often used in a double pass configuration, so that the output beam alignment is independent of the frequency shift. The bandwidth with which an AOM can perform frequency corrections is typically of the order of a few hundred kHz, and limited by the time it takes the radio frequency waves to travel in the crystal of the actuator. The range of frequency deviations for which an AOM can correct is usually about 10% of its nominal working frequency or less. Low frequency drifts are then corrected on the PZT of the laser.

We used in our experiment an AOM in double pass for the stabilization of the dipole trap laser on the optical cavity (see details in [Bertoldi 10]). This was sufficient for all our experimental work, but the stabilization system sometimes tended to unlock. We therefore decided to develop a new stabilization scheme [Kohlhaas 12], based on an actuator with both a larger correction bandwidth and correction range than an AOM. The results are shown in the following sections.

2.3.4.2. Principle of Serrodyne Modulation

An alternative component to an AOM to change the frequency of an optical beam is an electro-optical actuator (EOM), which at a wavelength of 1560 nm can have a bandwidth of several tens of GHz. An EOM is a phase modulator where the phase of the light is changed by the application of a voltage. Since the frequency is the time derivative of the phase, frequency corrections can be applied by an EOM by the application of a voltage ramp which results in a phase ramp. The maximal voltage before the EOM is damaged corresponds usually to a phase shift of a few times π. In a frequency stabilization system, it is therefore not possible to simply apply directly a correction voltage to an EOM, because frequency corrections cannot be maintained and the laser would unlock. An EOM can in this situation only be used in combination with a slower actuator, usually an AOM, as it was at first demonstrated in [Hall 84].

Preferentially, an EOM should be used as a single fast frequency actuator. This can be achieved by producing frequency sidebands of the light with a sinusoidal

radio-frequency or microwave field at the modulation input. The spectrum of the optical field E after modulation is:

$$E = E_0 \sum_{n=-\infty}^{\infty} J_n(\beta) \cos\left(\omega t + n\Omega_m t\right), \tag{2.6}$$

where ω is the frequency of the light, Ω_m is the modulation frequency, J_n are Bessel functions of the first kind and β is called the modulation depth. The frequency spectrum after modulation is a comb of equally spaced sidebands with a distance Ω_m from the central laser frequency. One of the first order sidebands $n = \pm 1$ could be injected in an optical cavity, and then frequency shifted with a correction bandwidth and range which corresponds to the bandwidth of the EOM. However, only a maximal fraction of $\eta = (J_1(\beta_{\max}))^2 \approx 0.34$ of the optical power can be put in an optical sideband and a large fraction of the light is lost. Since for most technological applications the optical power is a crucial parameter for the system performance this constitutes a significant drawback.

The limitation can be overcome by considering other modulation methods. In particular, by using a saw-tooth modulation with a frequency f_{saw} and phase amplitude $2\pi m$ with $m \in N$ [Johnson 88], the field after modulation is

$$E = E_0 \cos\left(\omega t + m f_{\text{saw}} t\right) \tag{2.7}$$

and so all light is shifted to a new frequency $\omega + m f_{\text{saw}}$. The frequency shifting effect can be easily understood as coming from a phase ramp, but where the phase is set back to zero at multiple values of $2\pi m$ to avoid damage on the EOM.

In practice, the quality of the frequency shifting depends on the quality of the generated saw-tooth form. A cheap and efficient method to generate the saw-tooth form relies on a non-linear transmission line (NLTL), which transforms a sinusoidal waveform to a high fidelity saw-tooth signal with the same fundamental frequency. A NLTL is a passive non-linear component and its output can be directly connected to an EOM. Using this technology, serrodyne frequency shifts from 200 MHz to 1.6 GHz and efficiencies up to 80% [Houtz 09, Johnson 10] were achieved.

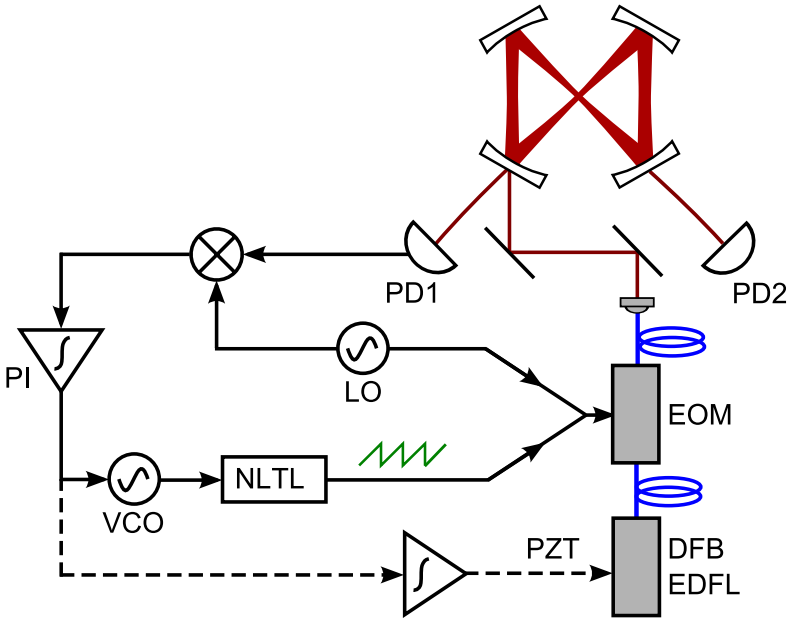

Figure 2.4.: Schematic overview of the laser stabilization on an optical cavity based on serrodyne frequency shifting. The optional feedback path on the piezo transducer (dashed lines) is used for long term drifts of the optical cavity.

2.3.4.3. Locking Scheme

We show now how serrodyne frequency shifting can be adopted for the stabilization of a laser on an optical cavity. The scheme is based on changing the frequency of the sinusoidal wave at the input of the NLTL, which tunes the frequency of the light after the EOM. A schematic overview of the stabilization setup is shown in Figure 2.4.

The feedback scheme is demonstrated with the dipole trap fiber laser at 1560 nm. The typical linewidth of the laser is a few kilohertz and therefore much smaller than the linewidth of the optical cavity equal to $\gamma = 546$ kHz. An active feedback system requires an error signal, which indicates by which distance and direction the system deviates from the target state. For the laser frequency stabilization on an optical cavity this error signal is usually derived with the Pound-Drever-Hall (PDH) method [Drever 83].

The method to generate a PDH signal is contained in Figure 2.4. An EOM (PM-0K5-00-PFA-PFA, Eospace) generates frequency sidebands with the help of

a local oscillator (LO, $f = 20$ MHz), and the carrier is injected in the optical cavity. The reflected light is detected on a photodiode (PD1, PDA10-CF from Thorlabs) and demodulated with a mixer. Each sideband beats with the optical carrier. Nevertheless, when the laser frequency is exactly resonant to the cavity, the beat-notes cancel each other because the sidebands have a relative phase π. When the carrier is not perfectly on cavity resonance, the carrier light in reflection is phase shifted with respect to the sidebands and the two beat-notes are asymmetric. After detection and demodulation, an error signal as in the bottom part of Figure 2.5 is obtained.

The error signal is converted by an electronic servo controller into a correction signal. It is then sent to a voltage controlled oscillator (VCO, ZX95-625-S+, Minicircuits, nominal frequency range 280 MHz to 625 MHz). The correction signal is added to a voltage offset that sets the central operation frequency of the VCO to 390 MHz. The output of the VCO is amplified by a radio frequency (RF) amplifier (ZHL-1-2W-S-09-SMA, Minicircuits, output power 33 dBm) and then attenuated to 26 dBm to optimize the serrodyne shifting efficiency. The RF field is fed into the NLTL (7112-110, Picosecond Pulse Labs, 300-700 MHz nominal input range) to generate the saw-tooth signal. The saw-tooth is combined with the signal from the LO for the generation of the PDH sidebands on the same EOM with a power combiner (ZX10R-14-S+, Minicircuits).

The total range over which the frequency of the light can be shifted is from 280 MHz (limited by the VCO) to 500 MHz (limited by high frequency cut-off of the RF amplifier before the NLTL). This corresponds to a span of 220 MHz, which is a correction range of about one magnitude higher than typically obtained with an AOM. The correction range is not limited by the EOM, but by the electronic components used to generate the saw-tooth form. To improve the performance of the servo control, one should adopt a NLTL, a VCO and a RF amplifier with a higher dynamic range. The cavity can drift outside the correction range of 220 MHz by long term thermal drifts. We added therefore a low frequency correction channel on the laser piezo transducer (PZT) for very large frequency deviations. The correction signal used for the piezo is an integrated version of the correction signal for the EOM, which ensures that the piezo always dominates for low frequencies.

An important technical feature of the feedback system is that both the

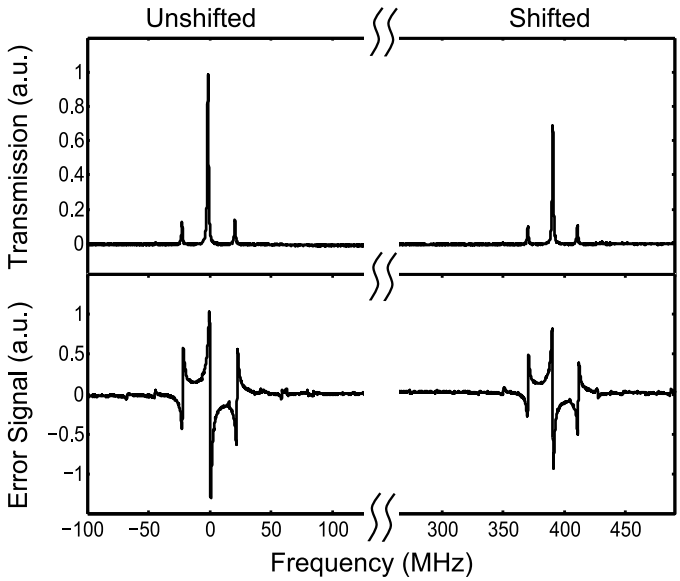

Figure 2.5.: Transmission signal (top) and error signal (bottom) when the frequency of the optical cavity is scanned. Both the transmission signal and the error signal are shifted by 390 MHz by the serrodyne modulation.

frequency shifting and the sideband modulation for the PDH signal are performed on the same EOM. Since one EOM is in any case needed to generate the PDH signal, this means that effectively no additional external modulator is needed. Only electronic components are added to perform the feedback. Both the laser and the EOM are fibered components, which results in low optical losses and a high robustness of the setup.

To demonstrate that we can both generate the frequency shifting and the optical sidebands on the same EOM, we observe the transmission of the optical cavity when we scan the resonator length in Figure 2.5. Both the transmission signal (top) and the error signal (bottom) are shifted by 390 MHz when the saw-tooth modulation is applied. The shifting efficiency for the transmission signal is 69% which is the only source of optical losses from the correction path. Light which is not frequency shifted either stays at the initial frequency (about 3%) or is diffracted to higher harmonics of the saw-tooth frequency (28%).

For our system the spurious frequency components do not pose a problem, since they are filtered by the optical cavity and we are only interested in the intracavity field. However, in other laser frequency stabilization schemes, only a small frac-

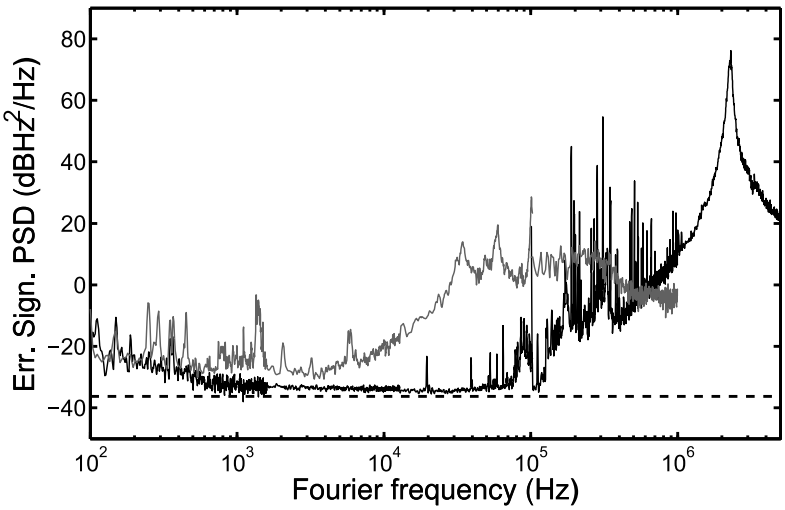

Figure 2.6.: Noise PSD of the error signal for the laser stabilized on the optical cavity with serrodyne frequency shifting (black) and an AOM in double pass (gray). The dashed line is the light shot noise limit on PD1.

tion of the light is used for the error signal on the optical cavity and feedback on the whole light field is performed. In this case, the spurious frequency components would stay in the beam. This is in general the main drawback of serrodyne frequency shifting schemes, also without an optical cavity, and limits its possible applications[8].

2.3.4.4. Lock Performance

The performance of the serrodyne technique in a closed feedback loop is analyzed by measuring the error signal. The fluctuations of the voltage of the error signal are taken after the mixer with a directional coupler and fed into fast-fourier transform (FFT) spectrum analyzer to measure the power-spectral density (PSD) of the noise. It is then converted to frequency noise with the slope of the Pound-Drever Hall signal and additionally corrected for the transfer function of the cavity of $(1+(2f/f_0)^2)^{-1}$ where $f_0 = 546$ kHz is the FWHM cavity linewidth.

The results are shown in Figure 2.6 in black. The bump of the PSD at 2.3 MHz indicates the bandwidth of the feedback system over which frequency fluctuations

[8] A solution to this problem could be to stabilize all the light of the laser on a Fabry-Perot cavity and take the transmission signal. If the length of the Fabry-Perot cavity is made tunable this would result in narrow linewidth tunable laser source.

cannot any more be corrected. It is limited for our system by phase shifts in the feedback controller at high frequencies, which brings the correction signal out of phase with the noise. The value of 2.3 MHz is about one magnitude higher what can be typically obtained with an AOM. The noise spectrum is from 2 kHz to 50 kHz close (within 3 dB) to the light shot noise on the photodiode. Below 2 kHz it is mainly limited by the voltage noise of the input operational amplifier (THS4601, Texas Instruments) of the electronic feedback controller board.

The same laser at 1560 nm was also stabilized on the optical cavity with a double pass AOM and the same photodiode. We can therefore compare the performance of the serrodyne lock with the one relying on a conventional double pass AOM as shown in gray in Figure 2.6. The bandwidth of the AOM system is only 250 kHz which is a factor 10 less than with the serrodyne scheme. The higher correction bandwidth gives the serrodyne method an advantage to reduce relative frequency noise, because the error signal can be started to be integrated one decade earlier. This leads to a higher feedback gain at low frequencies, which gives the serrodyne locking technique a better noise performance compared to a double pass AOM.

For the absolute frequency stabilization of lasers, the noise is mainly dominated by the length fluctuations of the ultra stable reference cavity. Feedback schemes with a higher correction bandwidth are therefore currently not required. Instead, the motivation for the serrodyne stabilization method was to design a lock that is very robust against perturbations from the environment. The bandwidth tells how fast the feedback system can correct against disturbances, whereas the correction range determines until which noise amplitudes the correction works. Both parameters, correction bandwidth and range, are very high for the serrodyne lock and could be even further extended.

To quantify the robustness of the locking system, we apply artificial external perturbations on the feedback loop. This is done by adding a sinusoidal voltage to the correction signal on the VCO. The maximal range until where perturbations on the frequency can be corrected for is defined as the position until where the relative noise between the laser and the cavity is the same as the cavity linewidth. We apply sinusoidal disturbances with different frequencies, and find for each frequency the maximal correction range, as shown in Figure 2.7 in black squares. From 1 kHz to 10 kHz, the maximal correction range corresponds to the dynam-

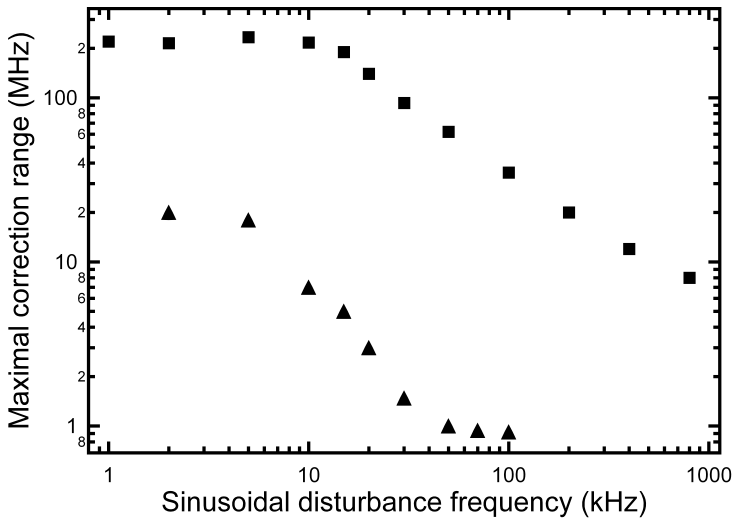

Figure 2.7.: Robustness of the stabilization system based on serrodyne (squares) or acousto-optic modulation (triangles).

ical range for the serrodyne frequency shifting of 220 MHz. Above 10 kHz, the feedback gain of the controller is not sufficient to keep the frequency fluctuations within the cavity linewidth and the maximal correction range decreases. Still, at 800 kHz the feedback controller can correct for maximal frequency shifts of 8 MHz.

We performed the same experiment with the double pass AOM system as shown in black triangles. The serrodyne technique can always correct for perturbations which are about one magnitude higher than as with the AOM technique. In addition, due to its higher bandwidth, it can still correct for fast perturbations for which the AOMs bandwidth would be not sufficient. We have not shown in Figure 2.7 the behaviour for frequencies below a few hundred Hz, because the correction in this range is applied in both system with a similar piezoelectric actuator.

The feedback method based on the serrodyne shifting technique performs better for all considered parameters (optical losses, bandwidth and robustness) than an AOM system. This is especially interesting if one considers that laser stabilization systems based on AOMs are mature technological components used in physics laboratories around the world, whereas we described here only a first experimental demonstration for the serrodyne technique. The demonstrated technique could be of interest for atomic physics experiments in harsh environments. For example, it could be used to operate a cavity enhanced dipole trap in an airplane for atom

interferometry experiments [Geiger 11].

In our experiment, we used the stabilization system not for the laser at 1560 nm for which we had already the AOM double pass system, but for a similar fiber laser at 1529 nm which was used for the light shift compensation method described in Section 2.6.1.

2.4. Dipole Trap Loading

2.4.1. AC Stark Shift

The interaction of atoms with light leads to an energy shift of the internal states of the atoms, called an alternating current (AC) Stark shift or light shift. The gradient of the energy shift leads to a force and it is this force which is used in an optical dipole trap. The energy shift by an external light field on the atoms is given by [Grimm 00]

$$U_{\text{dip}} = -\frac{1}{2}\left\langle \vec{p}\vec{E} \right\rangle = -\frac{1}{2\epsilon_0 c}\text{Re}(\alpha)I(r) \ , \tag{2.8}$$

where $\text{Re}(\alpha)$ is the real part of the atomic polarizability and $I(r)$ is the spatial dependent light intensity on the atoms which is for us Gaussian. The polarizability is defined over the induced dipole moment $\vec{p} = \alpha\vec{E}$ from the external light field $\vec{E}$. For brevity, the notation α is used instead of $\text{Re}(\alpha)$, because spontaneous emission in an optical dipole trap is usually negligible. We work with linearly polarized light far more detuned than the hyperfine splitting of the atomic states. The polarizability is

$$\alpha_\mu = \frac{1}{\hbar}\sum_k \frac{\left|\langle k\left|d\right|\mu\rangle\right|^2 \omega_{k,\mu}}{\omega_{k,\mu}^2 - \omega^2} \ , \tag{2.9}$$

where μ is the state for which the polarizability is calculated, k are all the states to which the light couples from μ, $\omega_{k,\mu}$ are the transition frequencies and $\langle k\left|d\right|\mu\rangle$ are the dipole moments. The dipole moments for the dominant transition frequencies in ^{87}Rb are summarized in Appendix C.

2.4.2. Loading Scheme

The light shift on the excited states affects the loading and probing of the atoms in the optical dipole trap. We load the cavity enhanced dipole trap with the

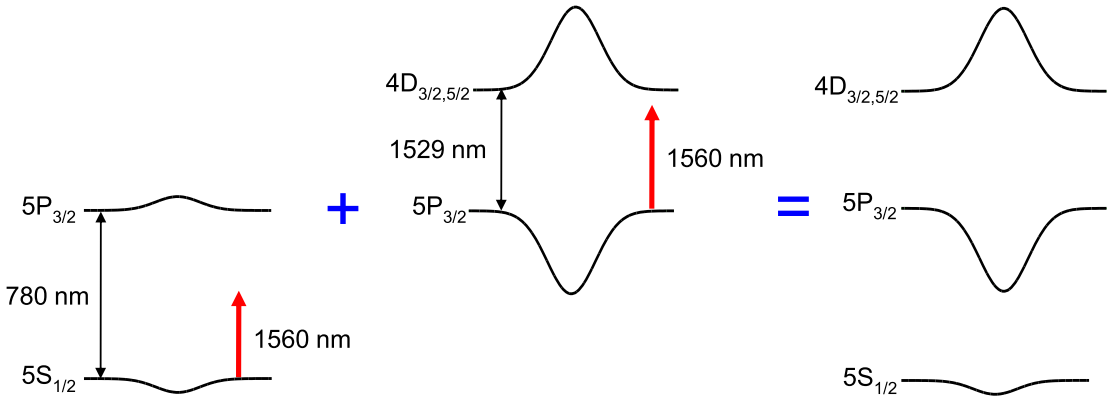

Figure 2.8.: Light shift on the D2 line ($5P_{3/2}$→$5P_{3/2}$) and on the $4D_{5/2,3/2}$ states by the dipole trap laser at 1560 nm.

atoms trapped in the 3D MOT. The maximal laser power is 200 W at 1560 nm per beam in the cavity. Because the dipole trap light is red detuned on the D2 line, the Gaussian beam lowers (red shifts) the energy of the $5S_{1/2}$ ground state of ^{87}Rb. This leads to an attractive potential at the center of the cavity with a depth of $U_0 = 1.4$ mK[9]. The trapping frequencies along the axis of the cavity beams in the plane of the cavity are $\omega_x/2\pi = \omega_y/2\pi = 1.2$ kHz and vertical to it $\omega_z/2\pi = 1.6$ kHz. The radiation from the dipole trap at 1560 nm introduces an exceptionally high light shift on the $5P_{3/2}$ state because it is close to the $5P_{3/2}$ →$4D_{5/2,3/2}$ transitions at 1529 nm, as seen in Figure 2.8.

At the center of the cavity, the light shift on the D2 line ($5S_{1/2}$→$5P_{3/2}$) brings both the cooling and the repumper radiation out of resonance, which has to be taken into account for the dipole trap loading. An efficient method to load a dipole trap at 1560 nm, based on a light shift induced dark MOT, has been developed in [Clément 09]. A similar version of the scheme is used in our experiment, and Figure 2.9 illustrates the atomic transition and laser frequencies in the adopted trap loading scheme.

We start with a cavity field with an initial trap depth of 100 μK to keep the light shift on the D2 line at 35 $\Gamma = 212$ MHz, such that it is smaller than the 267 MHz splitting between the $F' = 3$ and $F' = 2$ states. To make the loading more efficient, we need to at first compress the MOT. For this we increase the detuning of the

[9]The depth of an optical dipole trap is expressed in temperature units via $U_0 = k_0 T_0$

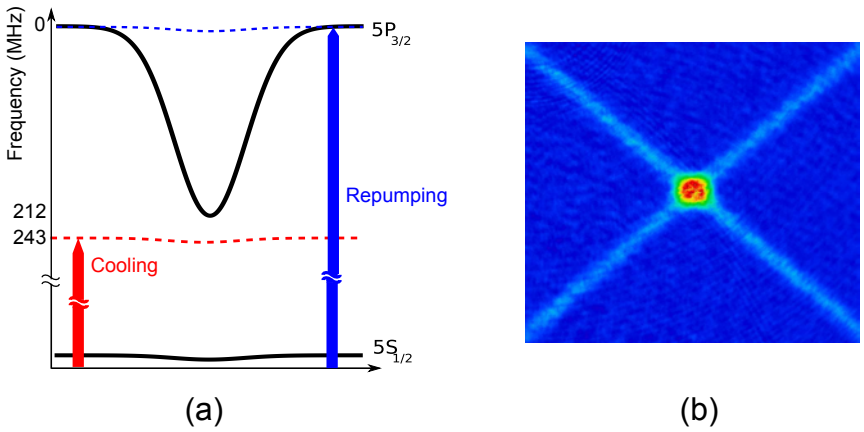

Figure 2.9.: (a) Loading with a light shift induced dark MOT. The cooling light is everywhere red-detuned with respect to the atomic transition, the cooling light is shifted out of resonance by the dipole trap. (b) Atoms imaged just after release from the dipole trap by absorption imaging. A part of the atoms is trapped in the cavity arms outside of the trap center.

cooling beams from 2.5 Γ to 5 Γ from the bare atomic transition. After that, we suddenly increase the detuning to 40 Γ for 100 ms[10]. The cooling light thus stays always on the red side of the atomic lines, also in the dipole trap region. In the dipole trap, the cooling beams are close to the $5P_{3/2} \rightarrow 5P_{3/2}$ cooling transition. The repumper frequency is unchanged during the whole loading process, and therefore out of resonance in the dipole trap. The atoms in the dipole trap region fall into the $F = 1$ state from which they cannot be repumped to $F = 2$. Neither the repumper or the cooling radiation then interact anymore with the atoms which have become "dark" and accumulate in the dipole trap.

2.4.3. Atom Number and Trap Lifetime

After the loading in the trap at a low cavity field power, the cooling radiation and the MOT coils are turned off and the dipole trap is ramped up to full power in 10 ms. Finally, 2×10^7 atoms at a temperature of 230 μK are trapped in the dipole trap. The temperature to trap ratio is $k_B T/U_0 \approx 6$. A major problem in the beginning of the experimental work was that the lifetime of the atoms in the dipole trap was only of the order of 100 ms. We found the problem to be

[10] Note that we do not switch off the magnetic field and there is therefore no Sisyphus cooling. The magnetic field cannot be switched off abruptly because the coils sit on the cavity mount and the servo control of the laser frequency on the cavity would unlock.

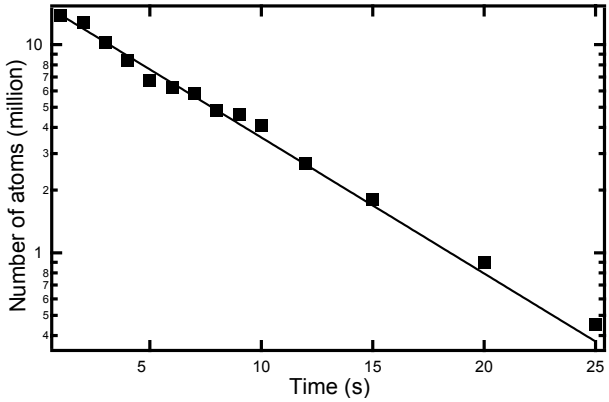

Figure 2.10.: Lifetime and atom number in the dipole trap after loading.

the back-reflection from diffusion in the optical cavity, where the back-reflected light interferes with the forward propagating light to form an optical lattice. In principle, the optical lattice should be no limitation for the atomic lifetime, but the optical cavity is not stabilized and therefore vibrates, which induces a motion of the lattice potential. To lower the effect, we reduced the fraction of the back-reflected light by changing slightly the alignment of the cavity mirrors. We could reach then lifetimes in the dipole trap of up to 6.6 s, as shown in Figure 2.10.

2.5. Evaporation and Bose-Einstein Condensation

2.5.1. Motivation

When an ensemble of Bosons is cooled down sufficiently, a large fraction of the atoms takes on the ground state wavefunction of the external potential. This means that the motional state of the single atoms cannot be distinguished anymore and the external state of the atomic ensemble can be regarded as a macroscopic quantum object. The main interest of such a Bose-Einstein condensate (BEC) for atom interferometry is in matter wave interferometry with the external atomic states. The temperature of a BEC of atoms is very low, typically in the tens of nK range, and the spread of the atomic cloud after a long interrogation time is therefore much lower than with a thermal atomic cloud with a temperature in the μK range. BECs are therefore used in new experiments such as in the drop tower experiments in Bremen [Müntinga 13] (where a whole experimental apparatus is dropped for 4.7 s) and fountain experiments with large interferometer arms [Dickerson 13]. One of the possible future directions of our experiment would be

to explore long interrogation times with BECs in an interferometer with bouncing schemes as in [Hughes 09].

On the other hand, experiments with BECs fall so far short in comparison with thermal clouds for absolute precision measurements. One main problem are the collisional interactions between the atoms in a BEC, which lead to systematic shifts of the energy of the internal states of $E_s = \mu/\hbar$, where μ is the chemical potential of the BEC. Furthermore, the preparation of a BEC takes usually several seconds, significantly increasing the cycle time in an atomic interferometer in comparison to the operation with thermal clouds. However, recently in [Stellmer 13] the direct Bose-Einstein condensation of strontium only by laser cooling was demonstrated. With this technique the condensation time could be significantly decreased and the cycle rate in a BEC atomic interferometer improved.

2.5.2. Evaporation and Condensation

It is shown now that with the cavity-enhanced dipole trap a BEC can be produced. For the evaporation, we ramp down the potential in the optical cavity. The goal is to increase the phase space density in the atomic cloud, given by

$$D = n_0 \lambda_{\mathrm{dB}}^3 = N_{\mathrm{at}} \left(\frac{\hbar \bar{\omega}}{k_B T} \right)^3 , \tag{2.10}$$

where n_0 is the atomic density, λ_{dB} is the thermal de Broglie wavelength, N_{at} is the number of atoms, $\bar{\omega} = (\omega_x \omega_y \omega_z)^{1/3}$ is the average trap frequency and T is the temperature of the atomic cloud. Above $D \approx 1$, the thermal de Broglie wavelength of the atoms becomes higher than the distance between the atoms and the gas becomes a BEC. During the evaporation process, the temperature T decreases by the release of hot atoms from the cloud and successive thermalization. In addition, also the trap frequencies decrease, since they are linked to the optical potential by

$$\omega_{x,y} = \sqrt{\frac{4U_0}{m\omega_{\parallel}^2}} , \quad \omega_z = \sqrt{\frac{8U_0}{m\omega_{\perp}^2}} , \tag{2.11}$$

where U_0 is the potential in one cavity arm, m is the mass of ^{87}Rb and the coordinate system is defined along the cavity axes. The ramp for the optical power is separated in several connected linear parts. Each part is optimized by choosing a final power level and then optimizing the ramp time. The time for

each ramp part is chosen as the point over which the phase space density does not increase anymore when the length of the ramp increases. Starting from this point, we start a new ramp and the process is iterated. With this procedure, we reached from the starting condition $D = 10^{-4}$ (T = 230 μK, $\bar{\omega} = 2\pi\times$ 790 Hz, $N_{\mathrm{at}} = 10^7$) a maximum phase space density of $D = 10^{-2}$, and therefore no BEC.

Nevertheless, from Equations (2.10) and (2.11) we see that the final phase space density is highly dependent on the beam waist of the dipole trap, and in addition a smaller beam waist leads to higher collision rate and therefore a more effective evaporation. Although our large beam waist of 100 μm in the dipole trap is practical for trapping a high number of atoms, it is less favorable for Bose-Einstein condensation. To nevertheless obtain a BEC, we add an additional beam at 1560 nm vertical to the cavity plane. This beam is called a dimple, and was at first used for the formation of BEC of cesium [Weber 03]. We use a dimple beam with an optical power of 200 mW and a small beam waist of 23 μm, and therefore with transversal frequencies of $\omega_x = \omega_y = 2\pi \times 550$ Hz. At full power of the dipole trap at the beginning of the ramp, the dimple potential is small with respect to the full field in the cavity. The cavity power is then ramped down to a frequency of $2\pi \times 50$ Hz in the vertical direction just sufficient to hold the atoms against gravity. At this low cavity power, the dimple potential is dominant in the transversal direction and the average trap frequency is $\bar{\omega} = 2\pi \times 250$ Hz. The phase space density in Equation (2.10) is therefore increased by a considerable factor of 125, due to the final frequency values. After a ramp of 3 s, we reach then a BEC of typically 5×10^4 atoms at a critical transition temperature of $T_c = 190$ nK. The phase phase space density is usually of the order $D \approx 4$.

2.5.3. Properties of BEC

In Figure 2.11, we see the density profile of the atomic cloud after a free time of flight (TOF) of 8 ms after switching off the dipole trap. To obtain the pictures, we used absorption imaging with a beam resonant on the $F = 2 \rightarrow F' = 3$ transition. The repumping light is switched on to ensure that the atoms are maintained in $F = 2$ and the absorption from the atoms follows the Beer-Lambert law. We observe the density profile for 3 different temperatures ($T = 0.8\ T_c$, $T = 0.7\ T_c$ and $T = 0.4\ T_c$ (74 nK)) and see an emerging double structure.

A BEC can be described as consisting of a thermal part which follows Maxwell-

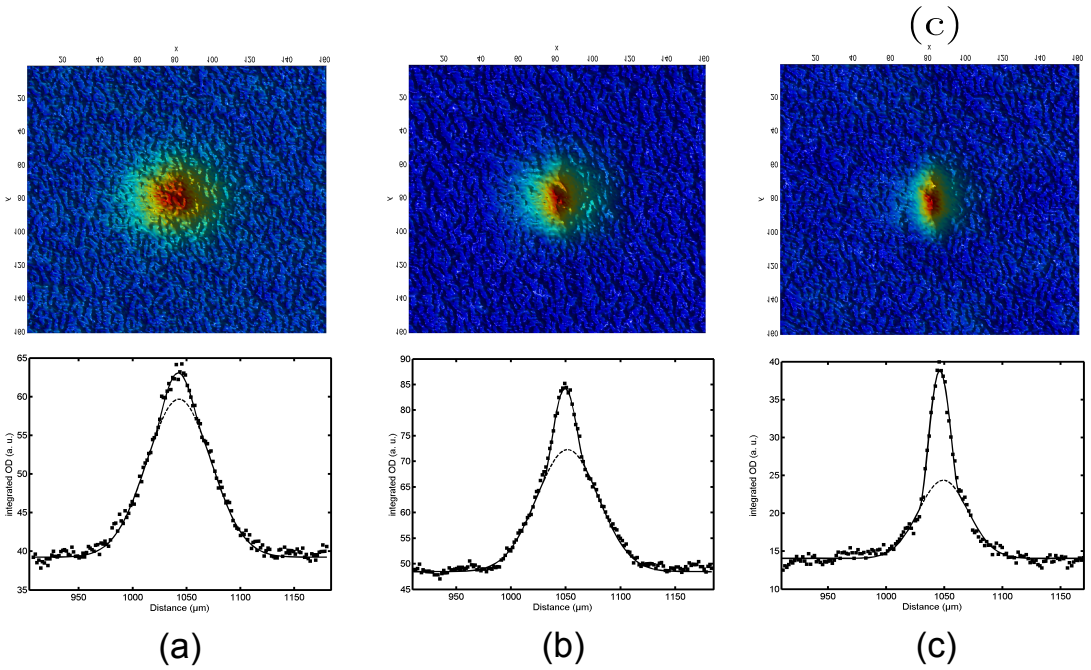

Figure 2.11.: Density profile of the BEC close to the critical transition temperature T_c after a time of flight of 8 ms . (Top) Color representation of the column density distribution. (Bottom) Density profile after integration of the previous images along the $y-$axis. The condensed part is fitted with a parabolic function and the thermal part with a Gaussian. The cloud temperatures T and condensed fraction η_c are from left to right (a) $T = 0.8\ T_c$ (145 nK), $\eta_c = 0.12$. (b) $T = 0.7\ T_c$ (131 nK), $\eta_c = 0.27$. (c) $T = 0.4\ T_c$ (74 nK), $\eta_c = 0.55$.

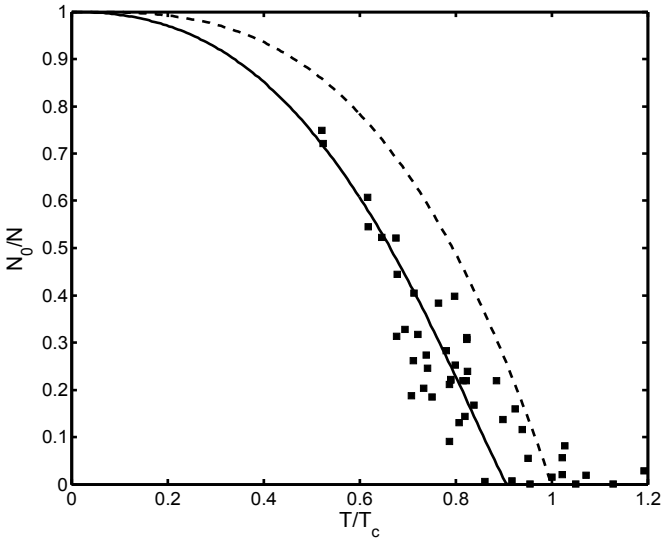

Figure 2.12.: Condensed fraction as a function of the temperature. The solid line is a fit with Equation (2.12) for a gas with interaction in the Thomas-Fermi regime, whereas the dotted line would be the result without interactions (μ=0)

Boltzmann statistics and a condensed part with the particles in the ground state of the trap. The density of the atomic cloud after the TOF describes the momentum distribution of the trapped cloud and consists therefore of two components. In the Thomas-Fermi approximation, the interaction energy is much larger than the kinetic energy. The condensed part then takes the form of the trap, which can be approximated by a parabola at its center. With a lower temperature the condensed fraction increases and a sharp peak appears. From the bimodal distribution the condensed fraction η_c=N_o/N_{at} can be determined as a function of the transition temperature, which is shown in Figure 2.12. The dependence of the condensed fraction on the temperature is given for a BEC with atomic interactions by [Dalfovo 99]

$$\frac{N_0}{N} = 1 - \left(\frac{T}{T_c}\right)^3 - \frac{\zeta(2)}{\zeta(3)}\frac{\mu}{k_b T_c}\left(\frac{T}{T_c}\right)^2 \left[1 - \left(\frac{T}{T_c}\right)^3\right]^{2/5}, \tag{2.12}$$

where ζ is the Riemann-zeta function. The chemical potential μ is the energy needed to add one extra particle. We fit the data in Figure 2.12 with Equation (2.12). The critical temperature as mentioned before is $T_c = 190$ nK and the

chemical potential is μ= h $\times$ 1.55 kHz.

2.5.4. Outlook with BEC

The finesse of $F = 1788$ of the optical cavity at 1560 nm is relatively modest, and can be easily increased by at least one order of magnitude. Only a few tens of mW of input power than have to be used to pump the optical cavity which could be derived from compact diode lasers at 1560 nm (e.g. with the PLANEX series from RIO). Combining optimized cavity parameters (i.e. a smaller beam waist) and a Sisyphus cooling phase, the dimple beam could be removed so that no laser amplifiers would be needed anymore. Such a setup could then serve as a cheap and compact all-optical BEC apparatus.

The number of atoms in the BEC of the order of 10^4 atoms is much lower than in a thermal cloud with up to 10^7 atoms. Since a higher atom number increases the signal-to-noise ratio and facilitates the nondestructive detection, we worked in all experiments with thermal atoms and not with a BEC. Nevertheless, based on the results of feedback control of atoms reported in this thesis, we propose in Section 5.7.1 a modification of a bouncing interferometer scheme for very long coherence times. Since the method would strongly benefit from atoms with ultracold temperatures, it is likely that for future work on the experimental setup BECs will be used.

2.6. Preparation of Internal States

2.6.1. Cancellation of Differential Light Shift

2.6.1.1. Compensation Method

The differential light shift from the dipole trap on the D2 line in ^{87}Rb was used for the loading of the atoms in the dipole trap. Unfortunately, the same differential light shift is a complication for other optical manipulation or probing techniques. The light shift is inhomogeneous in space and atoms at different position would therefore couple differently to incoming radiation. The compensation of the differential light shift by the dipole trap would therefore be preferential. To achieve this goal, we use a laser blue detuned to the $5P_{3/2} \rightarrow 4D_{5/2,3/2}$ transitions at 1529 nm. The light from this laser blue shifts the $5P_{3/2}$ state and can therefore compensate for the red shift from the 1560 laser. The principle of the compensation scheme is

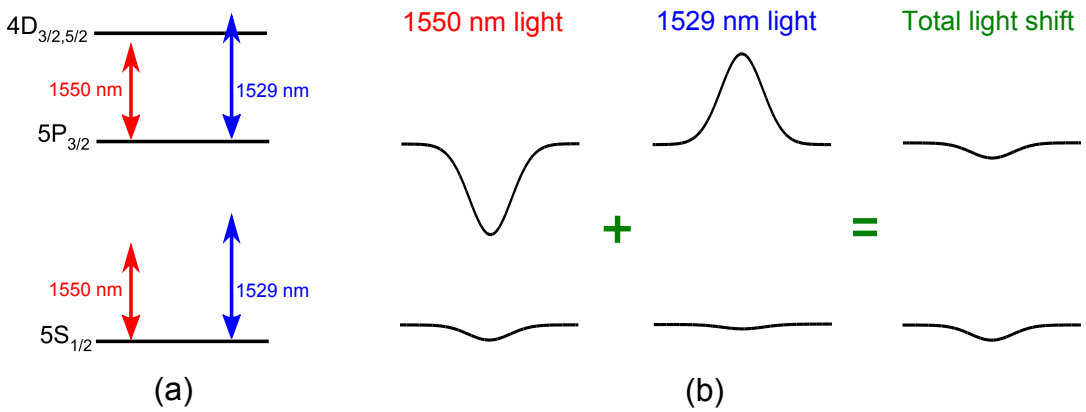

Figure 2.13.: Compensation scheme of the differential light shift from the dipole trap. A compensation laser at 1529 nm leads to an equal frequency difference for all spatial position on the D2 line while the ground state remains red shifted by the laser radiation.

shown in Figure 2.13.

Injecting both the dipole trap and the compensation laser in the fundamental mode of an optical cavity, a good mode overlap between the lasers is guaranteed, which allows a high spatial homogeneity. In the following we present the light shift compensation for a DFB EDFL at 1550 nm instead of a laser at 1560 nm. We repeatedly changed between fiber lasers at 1550 nm and 1560 nm because of technical problems (a broken laser piezo actuator) and because the laser at 1560 nm had a higher relative intensity noise than the laser at 1550 nm.

In Section 2.4, it was discussed that the light shift on the atomic levels is proportional to the atomic polarizability and the light intensity. Since the laser at 1529 nm is close to the $5P_{3/2} \rightarrow 4D_{5/2,3/2}$ transitions at 1529.261 nm and 1529.366 nm, its exact wavelength is crucial. We tuned the wavelength of the compensation laser to 1529.072 nm over the laser temperature and measured its wavelength with an optical spectrum analyzer. The atomic polarizabilities for our detunings are summarized in Table 2.2 and the calculation is described in Appendix C.

Since the polarizabilities for the $5P_{3/2}$ state have a different sign for the two wavelengths, it is possible to compensate the light shift on the excited state. In contrast, the light shift contributions add up for the ground state. As a condition

	$5S_{1/2}$	$5P_{3/2}$
1550 nm	6.79×10^{-39}	4.74×10^{-37}
1529 nm	6.8553×10^{-39}	-3.34×10^{-35}

Table 2.2.: Polarizability of the $5S_{1/2}$ and $5P_{3/2}$ states from the dipole trap and compensation laser. The unit of the polarizabilities is Jm^2/W.

for the light shift compensation, we set that the light shift at the center of the trap is equal both for the $5S_{1/2}$ and the $5P_{3/2}$ state. In this way, the transition frequency of the atoms at the trap center is the same as without a dipole trap. The compensation condition is fulfilled for

$$\frac{P_{1550}}{P_{1529}} = \frac{\alpha^{1529}_{P_{1/2}} - \alpha^{1529}_{S_{1/2}}}{\alpha^{1550}_{S_{1/2}} - \alpha^{1550}_{P_{3/2}}} \tag{2.13}$$

$$= 71.6\,. \tag{2.14}$$

2.6.1.2. Experimental implementation

We find experimentally the compensation position by scanning the power of the 1529 nm laser versus the power of the 1550 nm laser and imaging the atomic cloud when trapped in the dipole trap. For this we extinguish the 1529 nm laser from the cavity during the loading of the dipole trap[11], ramp the dipole trap power at 1550 nm in the cavity down to 6.4 W and switch on again the 1529 nm laser which is set at a different power level for each experimental run. The atomic cloud is imaged by absorption imaging. The result for the effective optical density in the trap as function of the 1529 laser power in the cavity is shown in Figure 2.14. The intracavity powers were calculated with Equation (2.5) from the output power of the cavity, where the finesse at 1529 nm was measured to be 10^3 by scanning over the cavity resonance with serrodyne frequency shifting.

The Lorentzian shape in Figure 2.14 is due to the line profile on the D2 transition. From the fit we find that the light shift from the dipole trap is compensated with the laser at 1529 nm with an intracavity power of 77 mW. The calculated power ratio from the lasers in the cavity is therefore 83, close to the

[11] The laser light is also serrodyne shifted out of the cavity resonance to ensure that no light enters the resonator during the loading.

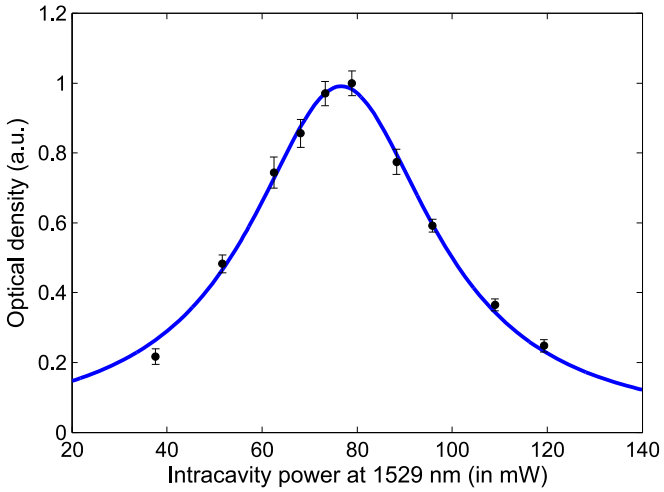

Figure 2.14.: Experimental compensation of the light shift in the dipole trap with the laser at 1529 nm. The light shift is canceled when the optical density of the cloud at the D2 line is maximal.

predicted value of 71.6. The deviation could be due to the cavity parameters at 1550 nm and 1529 nm, for which for example the contribution from light diffusion in the cavity is unknown. The direct measurement of the light shift compensation is therefore a better tool than just fixing the injection powers at 1529 nm and 1550 nm from the known properties of the optical cavity.

The differential light shift before the compensation is 60 MHz on the D2 line and is set by the 1529 nm laser to zero. Nevertheless, when the light shift at the center of the cavity is completely compensated, there is still a residual differential light shift in the trap from the different beam waists at 1529 nm and 1550 nm, as plotted in Figure 2.15. However, the highest absolute shift is less than 0.5 MHz over the size of the beams. This will be negligibly small for the large detunings chosen for the optical probe in Chapter 3.

The compensation method introduced here prevents that the atoms in the dipole trap are probed with spatially different couplings. Nevertheless, the presented method has some limitations for our experiment. Because the laser is stabilized on the optical cavity, we can set the laser frequency only in steps of 1 FSR≈1 GHz. The 1529 nm laser is only 24 GHz and 38 GHz detuned from the $5P_{3/2} \rightarrow 4D_{5/2,3/2}$ transitions, so that a change in the position of the cavity

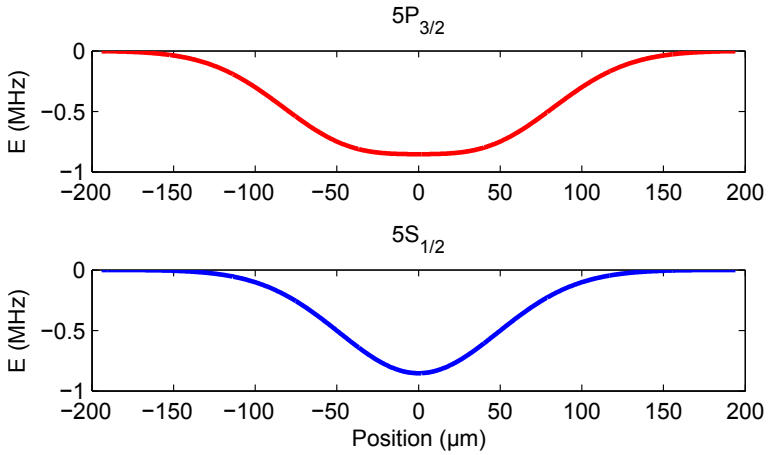

Figure 2.15.: Calculated light shift on the D2 line after compensation with the laser at 1529 nm. A residual light shift outside of the trap center remains because of the different beam sizes.

resonance changes the polarizability from the 1529 nm laser. The non-stabilized optical cavity is therefore the main weakness of the compensation scheme and the cavity should be actively stabilized[12]. An additional strategy to reduce the relative frequency fluctuations is to use a compensation laser with a higher power such that the laser detuning from the atomic transitions can be increased. Both the lasers at 1529 nm and 1550 nm were power stabilized on a bandwidth of 5 kHz and 100 kHz, respectively. The power fluctuations are negligibly small with respect to the frequency fluctuations of the cavity.

In general, the light shift manipulation with the laser at 1529 nm is an interesting tool to change the properties of the trapped atoms. It could be further explored by considering other loading schemes in the optical dipole trap. As an example, the dimple of Section 2.5 at 1560 nm could be replaced by a dimple at 1529 nm to invert the light shift on the D2 line and test loading schemes similar as in [Stellmer 13].

[12]The cavity could be stabilized by doubling the 1560 nm dipole laser, beating it with the repumper, and taking the error signal to act on the piezoelectric actuators controlling the length of the cavity.

2.6.2. State Purification

After the trap loading, the internal state of the atoms is a statistical mixture of the magnetic sublevels $m_F = 0, \pm 1$ of $F = 1$. Without any external magnetic field, the states are degenerate, but nevertheless couple differently to different polarizations of coherent microwave radiation at 6.835 GHz[13], which can drive the atoms into the magnetic substates $m_F = 0, \pm 1, \pm 2$ of $F = 2$. In an optics analog the state of the atoms is equivalent to different polarizations of an optical beam. We want to work with an atomic ensemble with internal states as pure as possible and therefore want to clean the "polarization" of the atoms and prepare all atoms in the atomic cloud in $|F = 1, m_F = 0\rangle$. The states $|F = 1, 2; m_F = 0\rangle$ are insensitive to first order to the Zeeman effect and are therefore the stable clock states in the optical dipole trap.

A conventional method to prepare the atoms in $m_F = 0$ consists in the direct optical pumping on the $F = 2 \rightarrow F' = 2$ transition with counter propagating linearly polarized light. Since all the excitation paths on $|F = 2, m_F = 0\rangle \rightarrow |F' = 2, m_F = 0\rangle$ interfere destructively, no atoms can be pumped back on this transition and the atoms accumulate in $|F = 2, m_F = 0\rangle$. Unfortunately, this procedure could not be applied in our experimental apparatus, because we start with a high density atomic cloud with typically $3{\times}10^6$ atoms in a cloud size of 50 μm after the ramp. In a very dense cloud, each scattered photon can excite again other atoms in the cloud. Since the polarization of the light is then not defined anymore, it can pump electrons back from $m_F = 0$ in the other m_F states and the optical pumping is inefficient (less than 30% in our case typically), and the state is not pure after the pumping[14].

The state can be cleaned by applying a π-pulse[15] on the $|F = 2, m_F = 0\rangle \rightarrow |F = 1, m_F = 0\rangle$ transition and sending a strong unidirectional σ_+, σ_--polarized "blast" pulse on the $F = 2 \rightarrow F' = 2$ transition to eject the remaining atoms in $F = 2$ from the trap. Nevertheless, also this procedure cannot completely clean the atomic state, because the blast light can still, although with a low probability,

[13] We use as a microwave source a frequency chain at 7 GHz derived from a 10 MHz blue top quartz crystal, mixed with a radio frequency generator at 165 MHz. The microwave radiation at 6.835 GHz is then amplified to 500 mW and send on the atoms with an antenna

[14] A detailed treatment on the limitations of optical pumping in a dense atomic cloud can be found in [Boyer 00]

[15] The degeneracy of the m_F states is lifted by the application of a magnetic field offset of 0.5 Gauss such that only the m_F=0 states are addressed by the microwave.

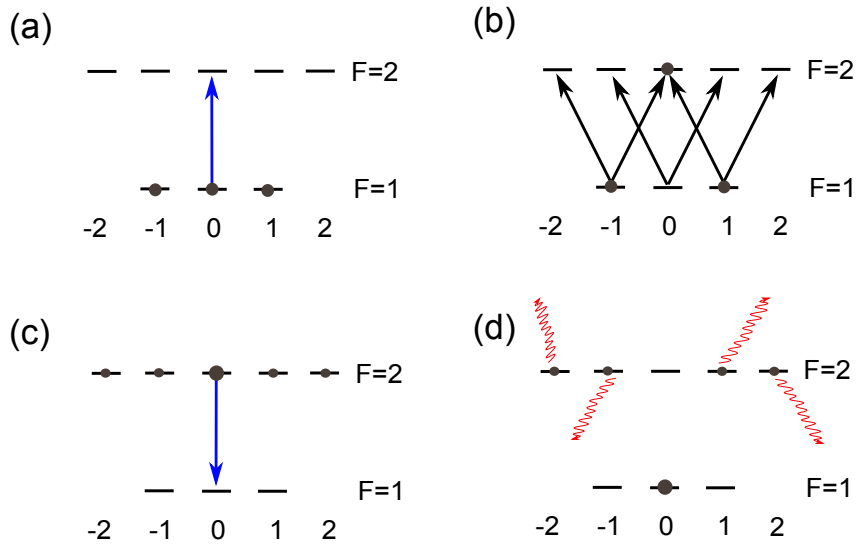

Figure 2.16.: State preparation scheme for a dense atomic cloud. The sequence consists of (a) a π-pulse, (b) repumping, (c) another π-pulse and (d) a blast pulse to remove atoms in $F = 2$. Steps (a) to (d) are repeated until the atomic state is pure.

excite the state $F' = 2$ from which the atoms can fall into $F = 1$. In a dense cloud, due to the rescattering of photons this effect is increased and the state after the blast is still not pure. The effect is enhanced when the atoms are in a deep trap since many recoils are needed in order go over the trap barriers.

To obtain nevertheless an atomic sample with pure internal states, we therefore developed a state preparation scheme based on the repeated purification of the internal states as shown in Figure 2.16. The state preparation starts with a π-pulse on the $|F = 1, m_F = 0\rangle \rightarrow |F = 2, m_F = 0\rangle$ transition and a repump pulse to pump the remaining atoms into $F = 2$. After that, slightly more than 1/3 of the atoms are in $|F = 2, m_F = 0\rangle$. We swap then the state from $|F = 2, m_F = 0\rangle$ to $|F = 1, m_F = 0\rangle$ with a π-pulse and blast away the atoms in $F = 2$. Then we repeat the procedure as often as necessary, typically 3 times, until there are no atoms anymore in the wrong m_F states.

The purity of the state is more than 99.9%, which was verified with absorption imaging. At first, we checked that there are no atoms in $F = 2$ after the

state preparation. In other experimental runs we transferred all atoms to $|F = 2, m_F = 0\rangle$ with a π-pulse, and measured the total atom number with and without radiation from the repumper. Because in both cases we measured the same atom numbers this proved that the atomic state was pure. With the presented state preparation method one can practically prepare atomic clouds of any density in a pure state in $m_F = 0$, but with an efficiency of only 30%.

After the state preparation and cleaning, we have an atomic ensemble with typically 8×10^5 to 10^6 atoms in the dipole trap with a cloud size of 50 μm and a temperature of 10 μK. The light shift compensation on the D2 line allows us to probe the atoms as if they are in free space. This configuration is kept for all results in the following chapters.

3. Nondestructive Detection System

3.1. Introduction

In this chapter, the development of our nondestructive detection system is described. Our goal was to construct a system where only a single beam passes through an atomic cloud in free space, measuring directly the population difference of two non-magnetic atomic states, while causing minimal spontaneous emission and no other spurious effects. The detection scheme relies on off-resonant dispersive probing of the atoms. In the development of nondestructive techniques to probe atoms, this approach has been very successful in the measurement of magnetic states by Faraday rotation (e.g. in [Smith 04, Takano 09, Koschorreck 10, Sewell 12]), and of non-magnetic states with an optical Mach-Zehnder interferometer [Appel 09b]. The most successful detection systems with the lowest probe-related decoherence rely on optical cavities to increase the atom-light interaction [Schleier-Smith 10, Chen 11, Bohnet 13].

Our nondestructive detection method is based on frequency modulation (FM) spectroscopy. A beam with several frequency components passes through an atomic cloud, and the components are dephased. This results in an amplitude modulation of the beam which is detected by a photodiode, and the demodulation of the beat-note signal gives information of the state population. The main interest of the method is that it represents until now the only solution to measure non-magnetic states with a single probe beam in free space, i.e. without an optical Mach-Zehnder interferometer. It can therefore be added to existing setups by the addition of only one beam.

In Section 3.2, an introduction of the basic principles of FM spectroscopy [Bjorklund 80] is given, with a focus on the design of a nondestructive detection system. In Section 3.3, our experimental setup is presented. Much room is then dedicated in Section 3.4 to the choice of the probe frequencies and powers, and to push the free space detection to its limits. In particular, an elegant solution

will be presented to avoid light shifts by the optical probe. First measurements with the nondestructive detection system are shown then in Section 3.5. We show, among others, the observation of Rabi-oscillations of the atoms in real time, and the measurement of the atomic projection noise.

3.2. FM Spectroscopy

FM spectroscopy has been first demonstrated by G. C. Bjorklund in 1980 [Bjorklund 80], and has since then become one of the main tools for precision measurements in atomic physics. The principles of FM spectroscopy applied to nondestructive measurements of atoms is outlined in the following.

3.2.1. Operation Principle

The operation principle of FM spectroscopy is shown in Figure 3.1. The light from a laser with carrier frequency ω_0 is phase modulated with a local oscillator (LO) of frequency Ω_m to form frequency sidebands, and passes through the atoms. Before the interaction with the atoms there is no amplitude modulation of the light, because the sidebands have phases of $\pm\frac{\pi}{2}$ and the beat-note of the upper sideband with the carrier cancels with the one of the lower sideband and the carrier. Asymmetric dephasing of the sidebands due to interaction with the atoms leads then to an amplitude modulation of the light, which is detected on a photodiode and demodulated with a mixer.

Since all probe light passes through the same optical path, the detection is robust against path length fluctuations. Furthermore, the detection of the beat-note is performed at microwave frequencies (between 3 GHz to 4 GHz), whereas typical stray light only has components in the low frequency or in the THz range. The detection can therefore be used in a fully illuminated room without any addition of noise in principle.

In our probe scheme, we will always set the frequencies and powers of the probe light such that one sideband interacts mainly with atomic populations in $F = 2$ and the other one with $F = 1$, giving a direct measurement of the population difference between the states. The optical carrier therefore only acts as a phase reference and the spontaneous emission is dominated by the frequency sidebands.

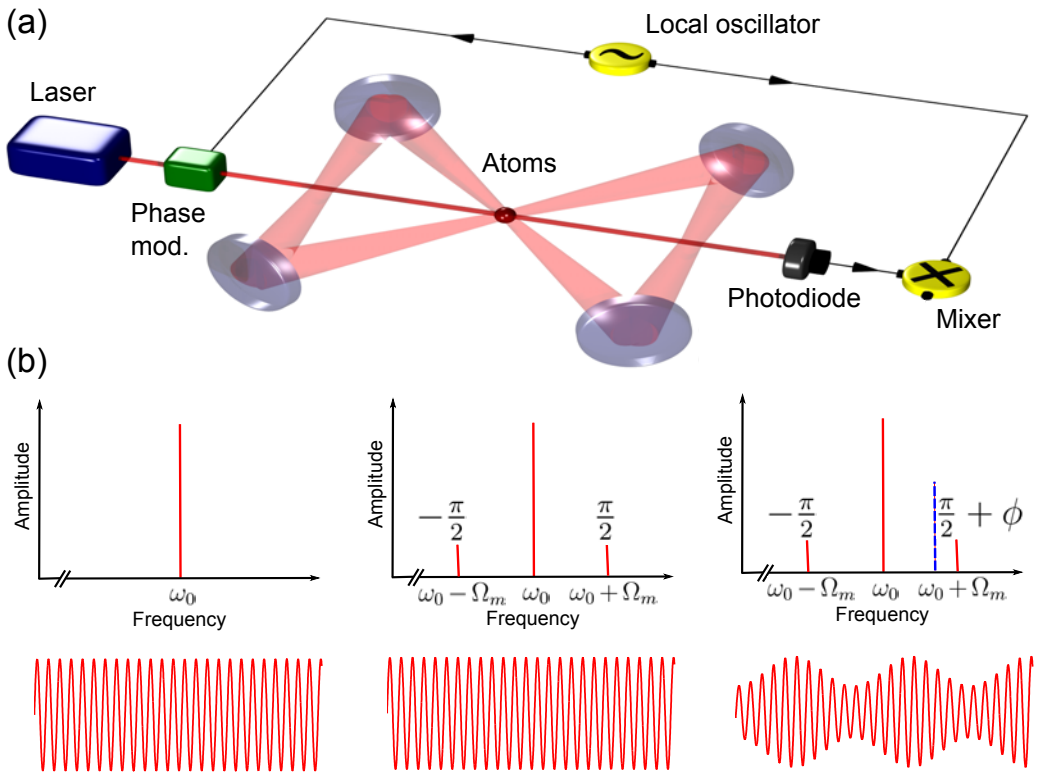

Figure 3.1.: Operation principle of FM spectroscopy with atoms trapped in our optical cavity. (a) Main components of detection system (details in main text). (b) Frequencies and phases in the probe light from left to right with no frequency sidebands, with freqency sidebands, and having passed through the atomic cloud. The corresponding light fields are sketched (exaggerated) below.

3.2.2. Detection Noise

In the state detection, the interference term between the electric fields of the carrier (power P_c) and the two sidebands (each with a power P_s) is recorded. The sidebands are coupled with the same coupling coefficient to an atomic transition and beat with the optical carrier. The maximal signal expressed as the electronic current after the photodetection is

$$S = \langle i_S \rangle = 2\frac{\eta_q e}{\hbar\nu}\sqrt{P_c}\sqrt{P_s}|\Phi_{\max}| \,, \tag{3.1}$$

where $|\Phi_{\max}|$ is the total phase shift when all atoms are in one of the probed states, η_q is the quantum efficiency of the detector, e the electronic charge, and ν is the

frequency of the light. The phase shift $\Phi_{\max}$ is the sum off all phase shifts from each atom in the addressed state,

$$\Phi = N_{\text{at}}|\phi| \ , \tag{3.2}$$

where N_{at} is the total number of atoms in the cloud and ϕ the phase shift for a single atom. Under the assumption that the detection noise is dominated by the shot noise of the carrier, the current noise after detection is given by

$$N = \langle i_N \rangle = \sqrt{2e\frac{\eta_q e}{\hbar\nu}P_c\Delta f} \ , \tag{3.3}$$

with the detection linewidth (inverse of the detection time) Δf. Calculating the signal-to-noise ratio (SNR) and expressing it in terms of the photon number N_s, one arrives at

$$\text{SNR} = \sqrt{2\eta_q N_s N_{\text{at}}}|\phi| \ . \tag{3.4}$$

The operator form of the quantum measurement can be directly derived from the SNR of the detection. Since the photonic shot noise is white (it is due to the interference with the fluctuations of the vacuum field), the measurement operator has a Gaussian profile. The inverse of the SNR, the NSR, is the precision of the measurement. If we translate the NSR to the spin basis, i.e. to a full scale value of $J = N_{\text{at}}/2$, the measurement uncertainty expressed in the Dicke state basis becomes

$$\sigma_{\text{det}} = \text{NSR} \times N_{\text{at}}/2 = \left(2\sqrt{2}\sqrt{\eta_q N_s}|\phi|\right)^{-1} \ , \tag{3.5}$$

and the measurement operator is as in Equation (1.75)

$$M_{m_0} = \left(2\pi\sigma_{\text{det}}^2\right)^{-1/4} e^{-\frac{1}{4\sigma_{\text{det}}^2}(J_z - m_0)^2} \ . \tag{3.6}$$

As discussed in Section 1.3.3.5, the relevant parameter for spin squeezing is the measurement strength

$$\kappa = \frac{\sigma_J}{\sigma_{\text{det}}} = \sqrt{2\eta_q N_s N_{\text{at}}}|\phi| \ . \tag{3.7}$$

The results from Equations (3.5)-(3.7) are valid only if the detection is limited by photonic shot noise. If this is not the case, and the additional noise is Gaussian, it should be added to the variance in Equation (3.3). For different additional noise sources, the measurement operator may no longer be an unbiased Gaussian estimator as in Equation (1.75), and the operator has to be modified.

The above derivation shows how a generalized measurement operator can be found with very simple means, where the only requirement is the knowledge about the noise spectrum of the detection. The presented procedure holds in general and can be applied to any nondestructive measurement system. A similar result as in Equations (3.5) and (3.6) has been found in [Vanderbruggen 11] with a photon-to-photon method, requiring a much longer derivation.

From Equations 3.4 and (3.7), it can be seen that the precision of a measurement can be improved by a better quantum efficiency η_q of the detector, a higher atom number N_{at}, more photons in the sidebands N_s and a higher phase shift per atom $|\phi|$. However, the relevant parameter for nondestructive detection is not the measurement precision alone, but the measurement precision for a given destructivity from the probe. In the next section, we will show that precision for a given destructivity is independent of the detuning of the probe frequencies as long as the detuning is larger than the linewidth of the probed atomic transition. The dependence of the SNR versus the destructivity as a function of the probe waist is discussed in Section 3.4.4.

3.2.3. Dispersive Probing

In this section, we give the expressions for the phase shift and the spontaneous emission in the semi-classical approximation for a two-level system. This gives an overview of the experimentally relevant parameters, and serves as a starting point for the choice of the probe frequencies. The full treatment with all atomic sublevels is introduced in Section 3.4.

First, we look at the elastically scattered light from the atoms to estimate its phase shift. The on-resonance scattering cross section of a two-level system is

$$\sigma_0 = \frac{3\lambda_0^2}{2\pi} , \tag{3.8}$$

where λ_0 is the wavelength of the transition on resonance. The fraction of the incoming light that is elastically scattered is therefore

$$\frac{\sigma_0}{A} = \frac{\frac{3\lambda_0^2}{2\pi}}{\pi w^2} = \frac{3}{2}\frac{\lambda_0^2}{\pi^2 w^2} . \tag{3.9}$$

Elastic scattering uses the Lorentz-model for a weakly driven oscillator. The phase lag of the oscillator with respect to the driving field is $\pi/2$ on resonance. Due to the geometrical overlap of the incoming Gaussian beam and the spherically emitted light field, another $\pi/2$ factor in the far field appears. Therefore, the light has a phase shift of π and interferes destructively with the incoming field. The Lorentzian line shape from this interference process is

$$L_d = -\frac{2\Delta\Gamma}{\Gamma^2 + 4\Delta^2} \,, \tag{3.10}$$

where $\Delta = \omega - \omega_0$, ω is the laser frequency, and ω_0 the transition frequency. When one multiplies this result with the scattered fraction of the incoming light (Equation (3.9)) on resonance, one arrives at the phase shift from one atom,

$$\phi = \frac{3}{2}\frac{\lambda_0^2}{\pi^2 w^2}\frac{2\Delta\Gamma}{\Gamma^2 + 4\Delta^2} \approx -\frac{3}{2}\frac{\lambda_0^2}{\pi^2 w^2}\frac{\Gamma}{2\Delta} \,. \tag{3.11}$$

For spontaneous emission, a relevant parameter is the excited state population. It is given by

$$\rho_{ee} = \frac{\Omega^2}{\Gamma^2 + 4\Delta^2} \approx \frac{(\frac{\Omega}{\Gamma})^2}{4(\frac{\Delta}{\Gamma})^2} = \frac{I}{2I_{\text{sat}}}\frac{\Gamma^2}{4\Delta^2} \,, \tag{3.12}$$

where Ω is the Rabi frequency and I_{sat} is defined *via*

$$\frac{I}{I_{\text{sat}}} = 2\left(\frac{\Omega}{\Delta}\right)^2 \,. \tag{3.13}$$

Spontaneous emission leads to decoherence, and the atomic state decays with a rate $\Gamma\rho_{ee}$. From the comparison of Equations (3.11) and (3.12), one might be misled that an increase of the detuning improves the measurement precision for the same destructivity, because the phase shift scales with $1/\Delta$ and the spontaneous emission with $1/\Delta^2$. However, to compensate the loss in SNR in Equation (3.4) by a lower phase shift, the photon number in the sidebands N_s has to be increased quadratically by the same amount. This in turn leads to the same spontaneous emission rate for the same measurement precision. As long as the detection is in the dispersive regime with $\Delta \gg \Gamma$, the obtained information for a given destructivity is independent of the detuning.

3.2.4. Stability Against Path Length Fluctuations

FM spectroscopy can be considered as a lock-in amplifier with a built-in optical interferometer. The latter is robust against fluctuations of its path length since the light is only split in frequency space. In the lock-in amplifier, the signal at frequency Ω_m is multiplied with the reference signal at Ω_m to obtain a DC voltage. If the two signals are preset to have the same phase, the output voltage is

$$V_{\text{out}} = V_d \cos\left(2\pi\frac{\Delta L}{\lambda_m}\right) \approx V_d\left[1 - 2\left(\pi\frac{\Delta L}{\lambda_m}\right)^2\right] , \tag{3.14}$$

where V_d ranges from $-V_{\text{max}}$ to $+V_{\text{max}}$ and $V_{\text{max}} \propto N_{\text{at}}$. The fluctuations in the microwave phase are denoted by ΔL and are usually dominated by fluctuations in the optical path. The maximal absolute output voltage of V_d corresponds to the case that all atoms are in one of the probed states, and is zero for no atoms or for a CSS on the equator of the Bloch sphere. When $V_d = V_{\text{max}}$, the absolute error in the estimation of the population difference from path length fluctuations is highest.

In a standard Mach-Zehnder interferometer, optical path length fluctuations of 1 μm would completely wash out the interference signal. Instead, at a modulation frequency of $\Omega_m = 3.42$ GHz, as used in our experimental work, the wavelength of the microwave radiation is $\lambda_m = 8.8$ cm. From Equation (3.14), we see that the error from path length fluctuations of 1 μm is then only 2.6×10^{-9}, and so completely negligible. The disadvantage of working at high modulation frequencies is that it can be technically very demanding to reach a detection which is limited by photonic shot noise, which is discussed in more detail in the next section.

3.3. Experimental Setup

3.3.1. Optical Bench

The experimental setup for our probe is shown in Figure 3.2. An extended-cavity diode laser (ECDL) is frequency offset locked with respect to the repumper radiation (i.e. $F = 1 \rightarrow F' = 2$ transition of the D2 line) to provide the carrier frequency. The error signal is obtained by detection of the beat-note between the probe laser and the repumper laser on a fast photodiode (G4176, from Hamamatsu, terminated on a 50Ω bias-T). The beat-note is amplified with two microwave amplifiers (LCA-0408, from Miteq), and sent to a phase detector (ADF4108,

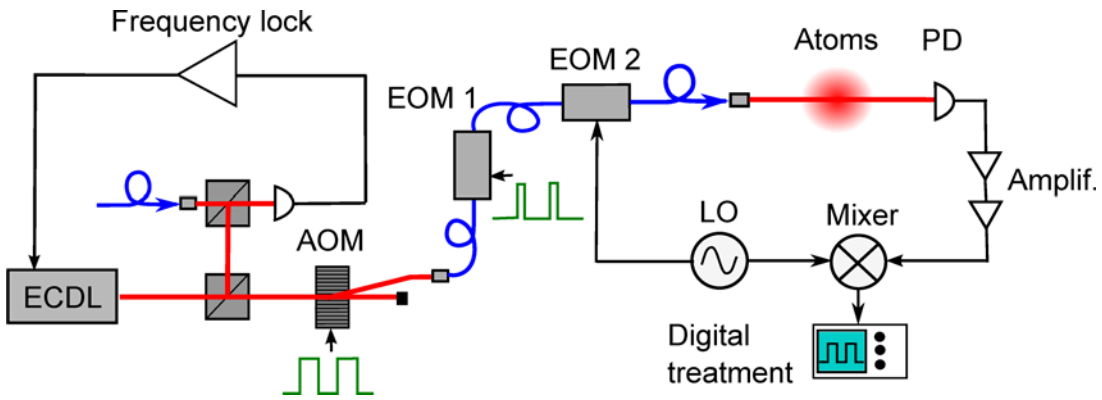

Figure 3.2.: Experimental system for the optical probe (details in main text). Light from an extended-cavity diode laser (ECDL) is frequency offset locked cia beat-note with repumper light and then sent with pulses from an AOM and EOM 1 through the atoms. The light is phase modulated using the local LO and EOM 2, and the beat-note is demodulated with a mixer and stored in a digital oscilloscope

from Analog Devices), following the method in [Appel 09a]. Feedback on the piezo and current of the ECDL is then performed to stabilize the carrier frequency.

Light pulses are sent by an acousto-optical modulator (AOM) with a rise time of 250 ns. Shorter pulses with a rise time of 1 ns can be sent with a Mach-Zehnder type amplitude EOM (NIR-MX800-LN-20, from Photline), and the outer AOM pulse window acts as a means for an additional probe attenuation. The short pulses for the EOM were derived from a pulse generator (33250A, from Agilent). The light is then phase modulated with an EOM (NIR-MPX800-LN-05, from Photline) with a LO (68017C, from Anritsu) in the microwave range, and the light is sent through the atoms.

Two different photodiodes were used for the experimental work in this thesis. The first one is a photodiode with integrated transimpedance amplifier (HFD3180-203, from Finisar) mounted on a homemade printed circuit board, which was used for all results in Chapter 4. The photodiode has the weakness of a depletion of the nondestructive signal under a sudden change of the power on the photodiode (we suspect as a reason the automatic gain control in the photodiode). We therefore added another light path on the PD (not shown in Figure 3.2), which was switched on when no pulses from the nondestructive detection were sent. In this way, the

light level on the photodiode was always constant.

The problem of the signal depletion was resolved by a different photodiode, used for all results in Chapter 5. This photodiode (1591 NF, from New Focus) is equipped with a fiber input. To avoid loosing a part of the signal, we dismantled the photodiode and focused the optical beam directly on the photodiode pin. The signal from the photodiode is amplified with two microwave amplifiers (716-PC7, from Hittite) and sent to a mixer (ZX05-73C-C+, from Minicircuits), where it is demodulated with the LO. The output signal is then stored in an oscilloscope (6100A, from LeCroy) for further treatment.

All the optics for the optical path were planned and designed with the ABCD matrix formalism for Gaussian beams and the beam waists on the atoms (245 μm for Chapter 4 and 47 μm for Chapter 5) were measured with a chopper wheel before adding the optics to the experimental setup. In Section 3.4, the choices for the locking position of the carrier and for the LO frequency and power are given.

3.3.2. Photodiode Characteristics

In order to avoid adding technical noise to the measurement, the photodiode noise spectrum at the detection frequency should be limited by the optical shot noise of the probe. We call the shot noise limit the light level for which the optical shot noise is at the same level as the electronic noise. The design of a photodiode with several GHz bandwidth and a low shot noise level is a demanding task. For example, we attempted to use a G4176 photodiode from Hamamatsu on a 50Ω bias-T, but were limited by the 50 Ω resistance converting the photocurrent to a shot noise limit of several mW. On the other hand, for photodiodes with transimpedance amplifiers, the bandwidth decreases when the transimpedance resistance increases. This limits the highest possible transimpedance resistance, and implies a reduced signal with respect to noise sources such as the Johnson noise of the transimpedance resistance. A low shot noise limit at high frequencies is therefore hard to reach.

We found a good solution with the photodiode 1591 NF (nominal bandwidth 4.5 GHz) from New Focus of which we removed the fibered input parts. We measured the shot noise limit as seen in Figure 3.3 at a frequency of Ω_m= 3.852 GHz. The signal was taken at the output of the mixer with a spectrum analyzer at a resolution bandwidth (RBW) of 300 kHz. By varying the optical power on the photodiode, we

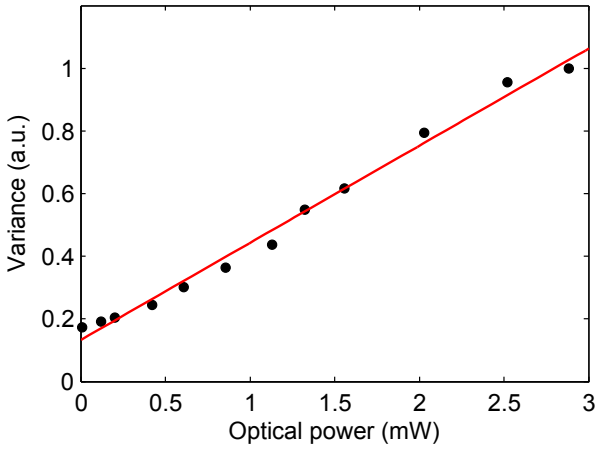

Figure 3.3.: Variance of the photodiode noise at 3.852 GHz as a function of the optical power on the photodiode. The linear part is from optical shot noise while the offset is the technical noise from the photodiode. The shot-noise limit is at 430 μW.

observe the change in the noise variance which increases linearly with the optical power. The linear slope proves that the light is dominated by white quantum noise[1], so that technical amplitude noise from the laser is negligible. We find from Figure 3.3 a shot noise limit of 430 μW. Most experimental results at modulation frequency of Ω_m= 3.852 GHz where performed at optical powers above this level.

3.4. Direct Population Measurement

The first results for the nondestructive detection were obtained by the probing of only one atomic level, and are explained in detail in the PhD thesis of Simon Bernon [Bernon 11a]. We are interested here in frequency configurations for the probe in which the population difference of two atomic states can be read out with a single pulse. At first, we give the scheme for the direct population measurement which is also used for the experimental results in Chapter 4. Several improvements of this scheme are presented, and the measurement of the atomic shot noise is reported. The updated probe scheme is used for the nondestructive measurements in Chapter 5.

[1]The variance of a light field with N_{ph} photons is $\sigma^2_{\mathrm{ph}} = N_{\mathrm{ph}}$.

3.4.1. Probe Scheme

In order to measure the population difference of the atomic levels $|F = 1, m_F = 0\rangle$ and $|F = 2, m_F = 0\rangle$, they should be probed with the same absolute couplings but with opposite sign. The strategy is to place the optical carrier between the hyperfine states and set the frequency sidebands close to the probed states. The frequency sidebands have to be on opposite sides of their respective dominating optical transitions. Since we want that the spontaneous emission induced by the carrier is negligible compared to that of the sidebands, it is reasonable to choose the modulation frequency Ω_m within the range 2.5 GHz - 4.5 GHz.

Our first probe scheme for the population difference measurement is shown in Figure 3.4. We placed one sideband close to the $F = 1 \rightarrow F' = 2$ transition, and

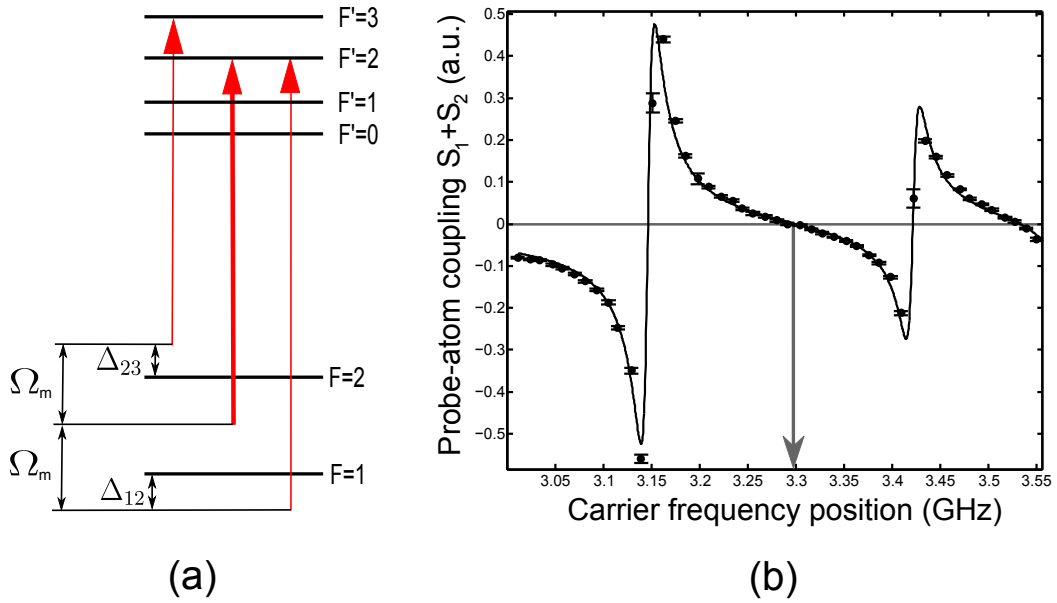

Figure 3.4.: (a) Hyperfine structure of the D_2 transition of ^{87}Rb with the frequency triplet from the optical probe. The bold arrow is the carrier and the thin arrows are the optical sidebands. The light is linearly polarized and only the m_F=0 states are populated in $F = 1$ and $F = 2$. (b) Dispersive signal when the position of the frequency triplet is scanned with respect to the atomic transitions. The x-axis is the frequency difference between the carrier and the $F = 1 \rightarrow F' = 2$ transition. The experimental points are shown in filled circles and the solid line is the calculation for the modulation frequency $\Omega_m = 3.421$ GHz.

the other one close to the $F = 2 \rightarrow F' = 3$ transition. The phase shift of the optical sidebands is proportional to S_F, which is the coupling coefficient from the probed hyperfine state F to all other excited states F'. It can be calculated by

$$S_F = \sum_{F'} \frac{\gamma \Delta_{FF'}}{\Delta_{FF'}^2 + \gamma^2 \left(1 + I/I_{\text{sat}}\right)} S_{FF'} \ , \tag{3.15}$$

where $S_{FF'}$ is here the coupling coefficient only for the transitions starting from $m_F = 0$ as taken from [Steck 01] and depicted in Table 3.1 for the relevant transitions.

S_{10}	S_{11}	S_{12}	S_{13}	S_{20}	S_{21}	S_{22}	S_{23}
$\frac{1}{6}$	0	$\frac{1}{6}$	0	0	$\frac{1}{30}$	0	$\frac{3}{10}$

Table 3.1.: Transition coefficients for π-polarized light for all hyperfine transitions on the D2 line from m_F=0. The transition coefficients for S_{11} and S_{22} are zero due to destructive interference of the excitation paths, whereas the transitions S_{13} and S_{20} are dipole forbidden.

For a direct population difference measurement, we must set $S_1 = -S_2$, i.e. the coupling coefficient from one sideband to the atoms should be opposite to the coupling coefficient from the other sideband. The condition of equal absolute couplings of the sidebands if fulfilled by adjusting the detunings $\Delta_{FF'}$ for each sideband. After demodulation of the beat-note, one obtains then a signal which is proportional to the population difference with $V_{\text{out}} \propto (N_1 - N_2) \propto J_z$.

Experimentally, we fix the modulation frequency $\Omega_m = 3.421$ GHz and prepare all atoms in an equal superposition of $|F = 1, m_F = 0\rangle$ and $|F = 2, m_F = 0\rangle$ with a $\pi/2$-microwave pulse. Since $N_1 = N_2$, we require that after demodulation we have $V_{\text{out}} = 0$. We scan the position of the carrier with respect to the $F = 1 \rightarrow F' = 2$ transition, which moves the three probe frequencies together. The experimental results are shown in Figure 3.4. They are in good agreement with the couplings calculated from Equation (3.15), and are drawn with a solid line. The carrier power for the measurement was 153 μW and a power per sideband of 7.1 μW. With a beam waist of the probe on the atomic sample of 245 μm, the intensity on the sample was 13.7 mW/cm^2. We take here for all transitions the saturation intensity for linearly polarized light on the D2 line of $I_{\text{sat}} = 2.503$ mW/cm^2

[Steck 01]. The condition $S_1 = -S_2$ is fulfilled when the carrier is 3.291 GHz away from the $F = 1 \rightarrow F' = 2$ transition, and the detunings of the sidebands to their closest transitions are Δ_{12} = -126.7 MHz and Δ_{23} = 148.5 MHz.

3.4.2. Suppression of Probe Light Shift

Besides spontaneous emission, another deteriorating effect that can affect the internal atomic states is the light shift from the optical probe. It can be split in two contributions, a global one, which describes how the total state is turned around the equator of the Bloch sphere, and an inhomogeneous part due the spatial variation of the probe intensity over the size of the cloud. In principle, both effects can be reversed by a spin-echo, i.e. π-pulse and a repetition of the probe pulse. However, experimentally, the time for the spin-echo cannot be chosen arbitrarily short, and the inhomogeneous contribution cannot be completely reversed, since the atoms move in the optical trap. The light shift from the probe represents then a source of decoherence.

Our three-frequency configuration allows to cancel the light shift from the optical probe. We can compensate the light shift from the strong carrier with the light shift from the optical sidebands. Since the sidebands and the carrier are perfectly overlapped spatially, the compensation is homogeneous. For the calculation of the required power in the sidebands, we use Equations (2.8) and (2.9) from Chapter 2 which are approximated as (see [Grimm 00], Equation 18)

$$\Delta E_F = \frac{3\pi c^2 \Gamma}{2\omega_0^3} \frac{I(r)}{h} \sum_{F'} \frac{S_{FF'}}{\Delta_{FF'}} \,. \tag{3.16}$$

The light shift on the atomic levels as a function of the probe power is shown in Figure 3.5. We assume for the calculation a carrier power of $P_c = 1$ mW and the frequency configuration from the previous section. The expected percentage of the power in the sidebands needed for the compensation is 5.3%.

Experimentally, we find the power in the sidebands for the light shift compensation by starting a Ramsey interferometer with a $\pi/2$-pulse, and then sending a probe pulse with a duration of 40 μs. The Ramsey interferometer is closed by another $\pi/2$-pulse. The results of the measurements are shown in Figure 3.6. The power in each sideband is changed from 2.4% to 7.5% of the power of the carrier

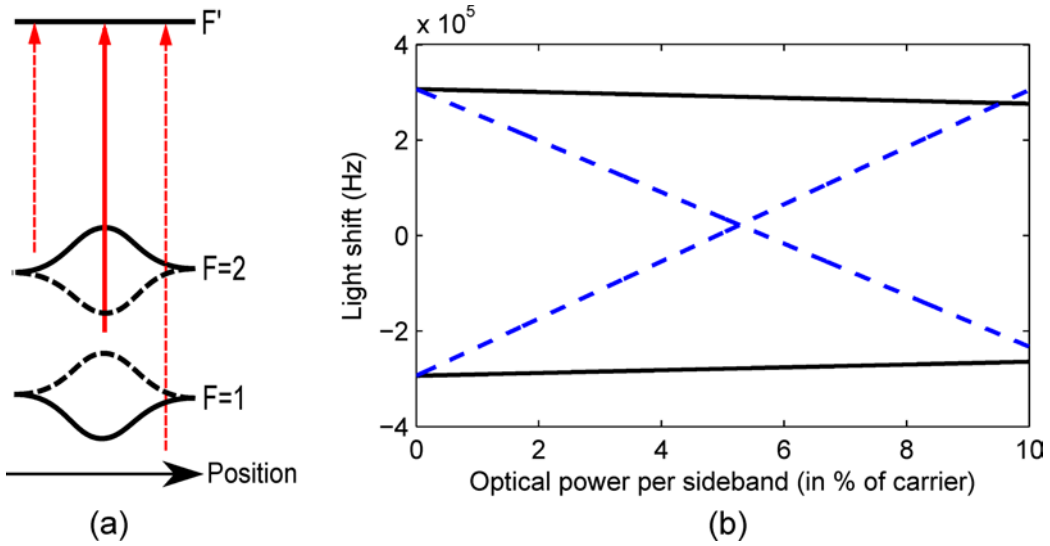

Figure 3.5.: (a) Principle of the light shift compensation scheme. The light shift from the sidebands cancels the light shift from the carrier. (b) Total light shift on the hyperfine states by the optical probe as a function of the sideband power. The black solid lines are the carrier light shift without sidebands, the blue dashed lines the light shift from both the carrier and the sidebands.

and a position with a maximal fringe contrast is found for 4.6%. The difference in power to the calculation could be due to the calibration of the sideband power from the phase modulation which was done at 2 GHz and not at 3.4 GHz. The sinusoidal form as a function of the sideband power is due to the rotation of the spin state around the equator of the Bloch sphere, induced by the light shift from the probe. The contrast of the signal decreases from the optimal light shift compensation point because of the inhomogeneous dephasing.

An additional drift in the Ramsey signal arises from optical pumping effects of the probe. From Figure 3.4(a), we can see that the upper sideband is close to the $F = 2 \rightarrow F' = 3$ transition, where the upper level can only decay to $F = 2$, whereas the lower sideband is close to the $F = 1 \rightarrow F' = 2$ transition, and the $F' = 2$ can both decay to $F = 1$ and $F = 2$. The probe therefore acts as a repumping beam and a long measurement pulse will cause an offset in the signal. The offset can be identified and systematically subtracted, but should be better avoided from the beginning. A probe scheme which can reject to first order the optical pumping effect is presented in the next section.

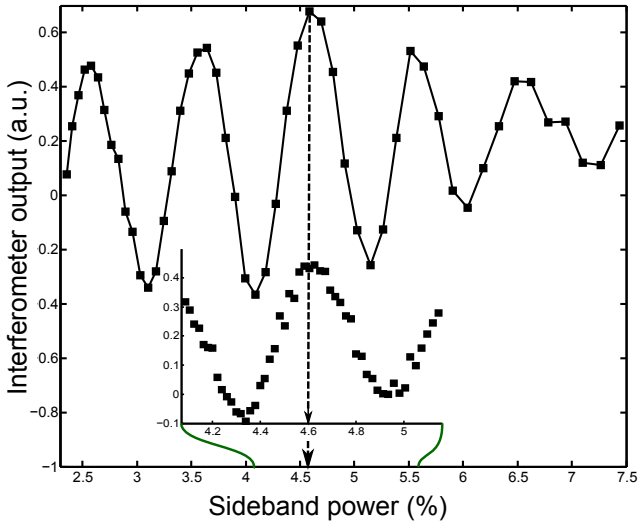

Figure 3.6.: Cancellation of the light shift due to the optical probe. The collective spin state rotates around the equator of the Bloch sphere and atoms dephase with respect to each other. For a minimal light shift from the optical probe, the contrast of the Ramsey interferometer is maximal. Inset: fringes for a longer pulse duration of 70 μs instead of 40 μs.

3.4.3. Balancing of Decoherence

Ideally, the population in each hyperfine state should remain the same under spontaneous emission. Furthermore, the hyperfine states should ideally not mix by spontaneous emission, which is a random process and therefore can add noise. However, we have the additional conditions for a direct population measurement ($S_1 = -S_2$) and for the cancellation of the probe light shift. We are therefore forced to keep a probe configuration similar as before, unless an additional light shift compensation beam should be superimposed with the probe. The population mixing during the measurement process is then inevitable. Nevertheless, the couplings can be set such that the decay is pointed towards the equatorial plane of the Bloch sphere, thus avoiding offsets.

For the calculation of the state redistribution from spontaneous emission, we approximate each transition as a separate two-level system, as it is valid in the limit of low excitations. The excited state population for each hyperfine state is

calculated from the stationary solution of the optical Bloch equations,

$$\rho_{ee} = \frac{1}{2} \frac{\frac{\mathrm{I}}{\mathrm{I}_{\mathrm{sat}}}}{1 + 4\left(\frac{\Delta}{\Gamma}\right)^2 + \frac{\mathrm{I}}{\mathrm{I}_{\mathrm{sat}}}} , \tag{3.17}$$

with

$$I_{\mathrm{sat}} = \frac{c\epsilon_0 \hbar^2 \Gamma^2}{4\mu^2 S_{FF'}} . \tag{3.18}$$

We consider only the initial distribution with atoms in the ground states in m_F=0, and the interaction with linearly polarized light, so that only the m_F=0 excited states are populated. Each excited state is then only populated by one separate transition (only S_{10},S_{12},S_{21} and S_{23} are nonzero). Since spontaneous emission is due to the interaction of the atoms with the unpolarized vacuum field, the atoms can decay with Δm=± 1 to the ground states. The branching ratio is calculated from the transition strengths $S_{FF'}$ on the D2 line and listed in Appendix C.

The optimal probe configuration is calculated iteratively by fixing each time

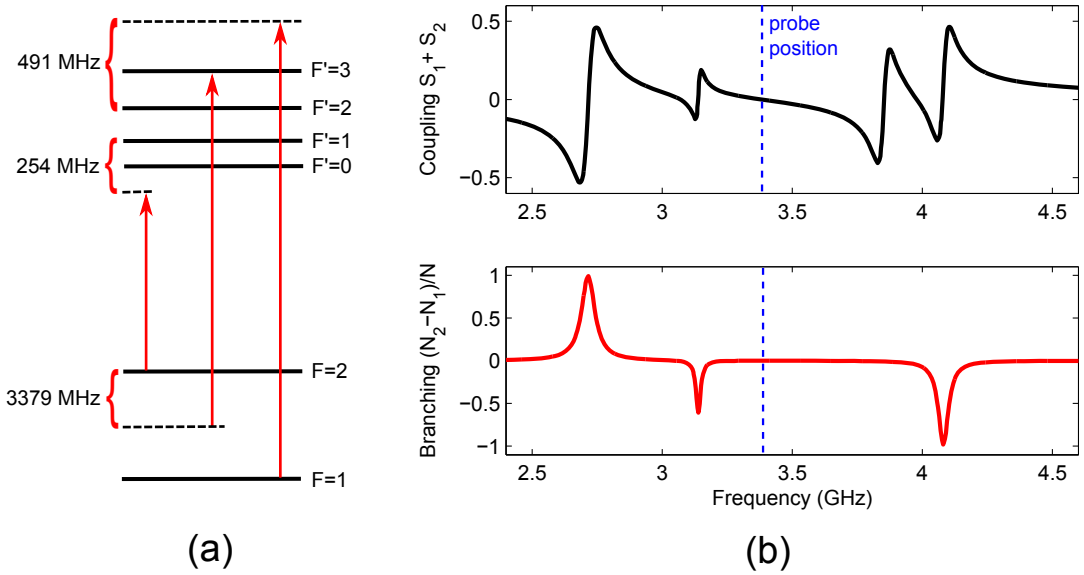

Figure 3.7.: Probe scheme with balanced decoherence. (a) Carrier and sideband frequencies. (b) Probe coupling and branching ratio to $F = 1$ and $F = 2$ as a function of the carrier detuning with respect to the $F = 1 \rightarrow F' = 2$ transition. A position with equal couplings and branching ratio is found at 3.379 GHz at a modulation frequency of 3.852 GHz.

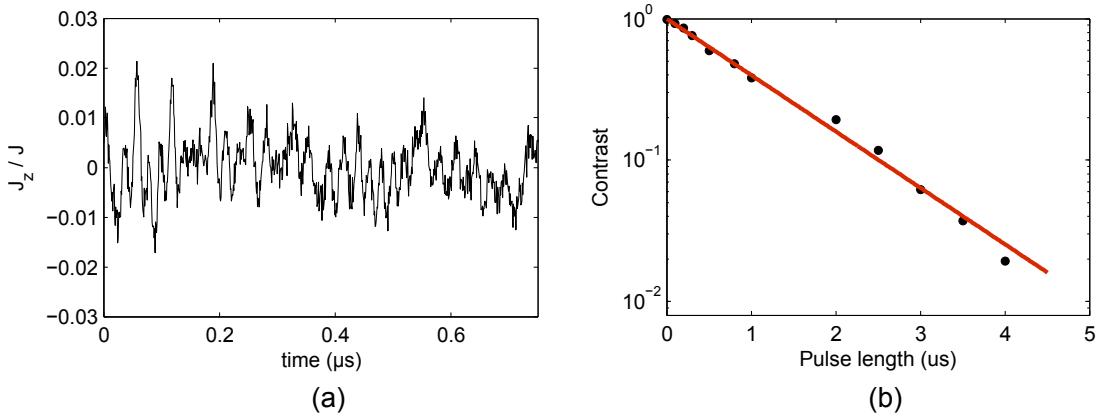

Figure 3.8.: Destruction of the atomic state by the optical probe. (a) Population difference measurement for a CSS prepared on the equator of the Bloch sphere. (b) Decay of state coherence measured with a Ramsey interefer-ometer.

the modulation frequency Ω_m, scanning the frequency triplet for the position of equal couplings, and calculating the spontaneous emission decay paths. When the two conditions of equal couplings and symmetric decoherence are fulfilled, the sideband power needed for the light shift compensation is calculated. It is then verified that the sideband power does not affect the found position for the probe frequencies. The configuration for which all conditions for the optical probe are fulfilled is at a modulation frequency of Ω_m= 3.852 GHz, a carrier lock position of 3.379 GHz and a modulation depth of 14.8%. The chosen frequency scheme is depicted in Figure 3.7(a), and the couplings and spontaneous emission branching is shown in Figure 3.7(b).

We show now that offsets are avoided in the new measurement scheme. For this we prepare a CSS on the equator of the Bloch sphere, and send a probe pulse at a power of 1.16 mW. The result is shown in Figure 3.8(a), where the signal is an average of 200 measurements. We use here a beam with a waist of 47 μm, which implies a high probe intensity. Together with the modulation index of 14.8%, this causes a decay of the state with a time of 1.18 μs, as seen in Figure 3.8(b). We see that the state stays close to J_z=0, even when more than 50% of the state coherence is destroyed. The fast decay of the state coherence is the reason for the amplitude EOM introduced in Section 3.3, with which probe pulses of only a few tens of ns length can be sent.

It is remarked that the mixing of the hyperfine states is still a constraint for the state measurements. The effect that the state decays towards the equatorial plane of the Bloch sphere implies that only short probe pulses can be used, or that the decay has to be fitted with an exponential. Moreover, when a CSS on the equator of the Bloch sphere is prepared, spontaneous emission leads to a random redistribution of the population difference, which counteracts measurement-induced spin squeezing. Another problem for precision measurements might be the redistribution of the m_F states. Since only the $m_F = 0$ states are coherently manipulated, an unequal distribution of the decay in the different m_F states leads to a changing background for high destructivities. The considered problems can in principle be overcome by preparing and probing the atoms on closed transitions such as $|F = 2, m_F = 2\rangle \rightarrow |F' = 3, m_F = 3\rangle$, but this cannot be combined with the condition of a direct population difference measurement, and not be performed with atoms in the $m_F = 0$ states.

3.4.4. Maximization of SNR for a Given Decoherence

The geometry of the probe should be chosen such that the SNR of the detection is the highest for a given destructivity. From Equations (3.4) and (3.11), we see that

$$\mathrm{SNR} \propto \sqrt{N_s} N_{\mathrm{at}} \frac{1}{w^2}\,, \tag{3.19}$$

while the destructivity scales as

$$\mathrm{destr.} \propto N_s \frac{1}{w^2}\,. \tag{3.20}$$

In order to keep the destructivity constant when the size of the of the probe waist w is multiplied by a factor ϵ, the number of photons has to be multiplied by ϵ^2. In Equation (3.19), the SNR is then changed by a factor ϵ^{-1}. However, the atom number N_{at} is then an effective atom number from the Gaussian overlap of the beam and the atoms, which is

$$N_{\mathrm{at}} = \frac{w^2}{w_{\mathrm{at}}^2 + w^2} N_{\mathrm{at}_0}\,. \tag{3.21}$$

If we set $w = w_{\mathrm{at}}$ in Equations (3.19) and (3.20) as the initial conditions so that $w = \epsilon w_{at}$, then the efficiency from the overlap of the probe and the cloud becomes

$$\eta_{\mathrm{w,SNR}} = \frac{\epsilon}{1 + \epsilon^2}\,. \tag{3.22}$$

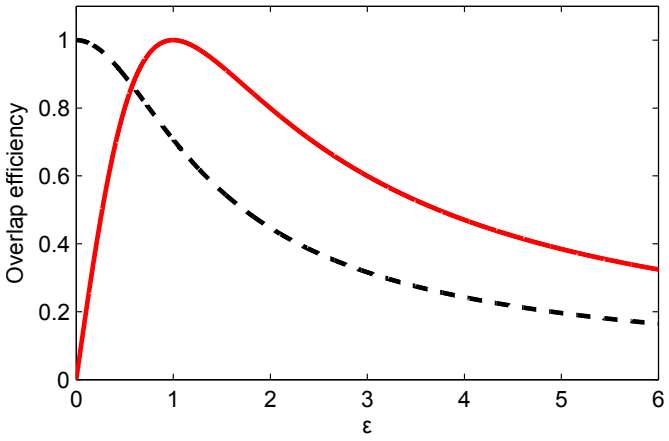

Figure 3.9.: Dependence of the signal-to-noise ratio (SNR, red line) or the projectivity (κ, black dashed line) on the ratio ϵ between the beam waist and the size of the atomic cloud

It should be noted, however, that if the criterion for the optimization is not the SNR, but the projectivity $\kappa \propto \sqrt{N_{\mathrm{at}}}$, the efficiency becomes

$$\eta_{\mathrm{w},\kappa} = \frac{1}{1+\epsilon^2} \tag{3.23}$$

The two formulas are plotted in Figure 3.9, normalized to their maximum values. Both formulas are only valid as long as $w \gg \lambda$. It can be seen from Figure 3.9 that for the SNR, there is a maximum at $\epsilon = 1$, while for κ it is always better to go to a smaller probe waist. Nevertheless, if the goal is real metrological gain, it is not beneficial to go below $\epsilon = 1$ because this reduces the SNR for the atomic interferometer due to a lower effective atom number. Note that the only demonstration so far on spin squeezing of nonmagnetic atomic states by free space probing in [Appel 09b] was performed by probing the column density of an atomic cloud with a beam waist of 27 μm.

We started our experiment with an initial beam waist of 245 μm, and then updated the experiment to a beam waist of 47 μm, which sets $\epsilon \approx 1$ and optimizes the SNR for a given destructivity. We measure the SNR by taking the full scale value after all atoms are pumped in $F = 2$, remove all atoms by a blast pulse, and take the measurement result without atoms. The pulse time is chosen such that the residual coherence is 98% after the pulse, so that we can compare the SNR for the same nominal destructivity. By repeating the experiment, we get a Gaussian

distribution of the measurement results which corresponds to the uncertainty of the measurement, shown in Figure 3.10. For a probe waist of 245 μm, we have a measurement uncertainty of 6.73%, and for a probe waist of 47 μm an uncertainty of 1.24%. The precision of the measurement is therefore increased by a factor 5.4 for the same destructivity. From Figure 3.9, we would have only expected an increase by a factor 2.6. The difference can be explained because in conjunction with the 47 μm prove waist we have also used the new photodiode, where we were are over the technical noise of the photodiode.

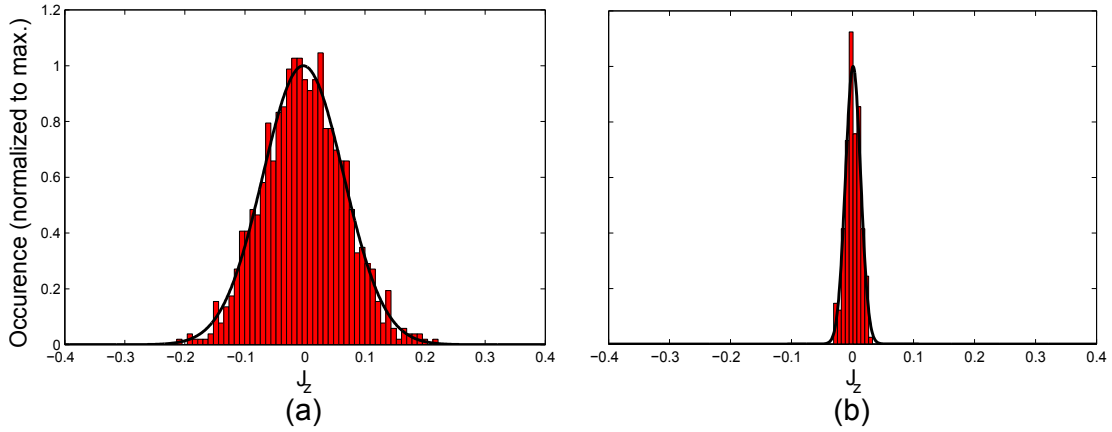

Figure 3.10.: Measurement uncertainty for a residual coherence of 98% (a) for a probe beam waist of 245 μm and (b) for a probe beam waist of 47 μm

3.5. FM Spectroscopy as a Calibration Tool

We show here some first results with our probe system. It is at first used as a tool to measure the frequency of Rabi oscillations induced by microwave radiation, and to precisely tune the microwave frequency on the clock transition. The main interest here is to use the FM spectroscopy as a fast calibration tool, since the cycle time for the experiment is up to a factor 10 shorter than with absorption imaging, which suffers from dead times because of the camera. We use then for the first time the nondestructive character of the measurements, and follow the Rabi oscillations in real time, which shows that the Rabi frequency can be approximately determined after only a single run of the experiment. Finally, we present the measurement of the atomic projection noise that shows the intrinsic quantum noise feature of the coherent spin state (CSS). Furthermore, it gives us a convenient method to

determine the effective atom number without the need to determine any couplings as for example in fluorescence imaging.

3.5.1. Characterization of Microwave Source

3.5.1.1. Measurement of Rabi Frequency

The measurement of the Rabi frequency is shown in Figure 3.11. The measurement was performed with the probe scheme from Section 3.4.3, with a beam power of 450 μW and a beam waist of 47 μm. The atoms start in $F = 1$ and cycle through the superposition states between $F = 1$ and $F = 2$ because they are shined with resonant microwave radiation. For each point in Figure 3.11, we change the length of the microwave radiation pulse, and destroy at the end with a long probe pulse the internal state of the atomic ensemble. We found here a Rabi period of 268.6(4) μs.

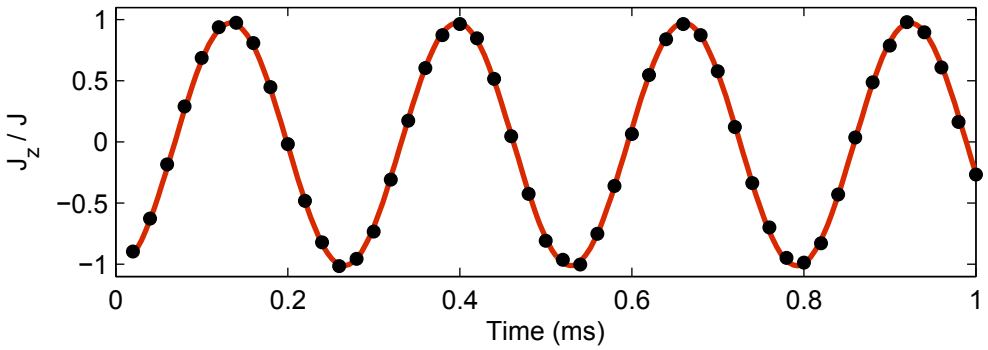

Figure 3.11.: Measurement of the Rabi frequency with FM spectroscopy. Each point was taken from 10 repetitions of the experiment

3.5.1.2. Setting of Microwave Detuning

In order to set the microwave frequency, we run a Ramsey interferometer with different interrogation times. We prepare all atoms on the equator of the Bloch sphere with a $\pi/2$-pulse, let them freely evolve during a Ramsey interrogation time T and read out the result with another $\pi/2$-pulse. The result can be found in Figure 3.12. We use here the probe scheme with sidebands generated by modulation at 3.4 GHz, and a probe pulse length of 10 μs with 1.1 mW beam power. The Ramsey interrogation time is 40 ms, and the position of zero microwave detuning was

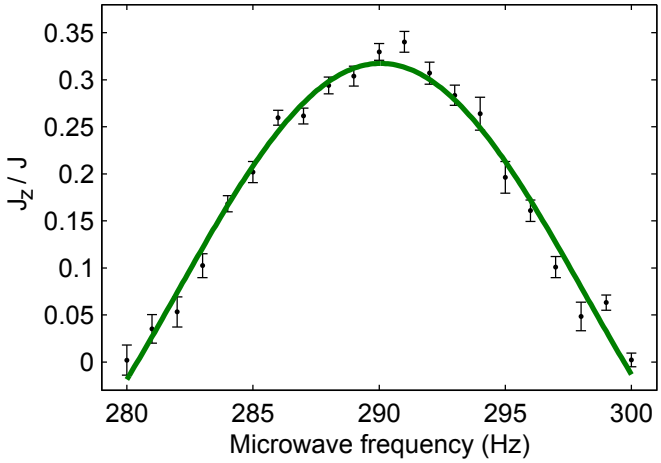

Figure 3.12.: Output of Ramsey interferometer after 40 ms interrogation time for a changing microwave frequency.

confirmed for other interrogation times. We could fix the microwave-atom detuning with 1 Hz precision, limited by the resolution of the RF generator (IFR2023A) mixed with the 7 GHz signal from the frequency chain to deliver the signal at 6.834 GHz[2].

3.5.2. Real Time Observation of Rabi Oscillations

The methods in the previous section did not use the nondestructive character of the measurements by FM spectroscopy. For a first demonstration of the interest of the non-demolition measurements, we observe in real time the Rabi oscillations of an atomic cloud in a single experimental run as shown in Figure 3.13. The results presented here are similar to those obtained in the group of E. Polzik [Windpassinger 08]. We use the probe scheme described in Section 3.4.3, with a beam power of 0.12 mW, a beam waist of 47 μm and pulses of 100 ns duration. The collective internal state of the atomic ensemble is read out every 1.1 ms and the period of the Rabi oscillations is 311 μs. After 200 measurements on the same state, the coherence of the internal state is still 45%. The nondestructive measurement allows therefore to interrogate the atomic state repeatedly during its coherent evolution. This tool will be used in Chapters 4 and 5 to either perform feedback on the atoms or on the LO in an atomic clock. In addition, the nondestructive detection is a useful tool for the precalibration of the Rabi

[2]The frequency of the chain was typically drifting a few Hz over one week. The frequency was therefore set periodically, especially before important measurements.

frequency and of the microwave frequency from the result of a single experimental run. The real time observation of the phase in a Ramsey interferometer will be shown in Chapter 5.

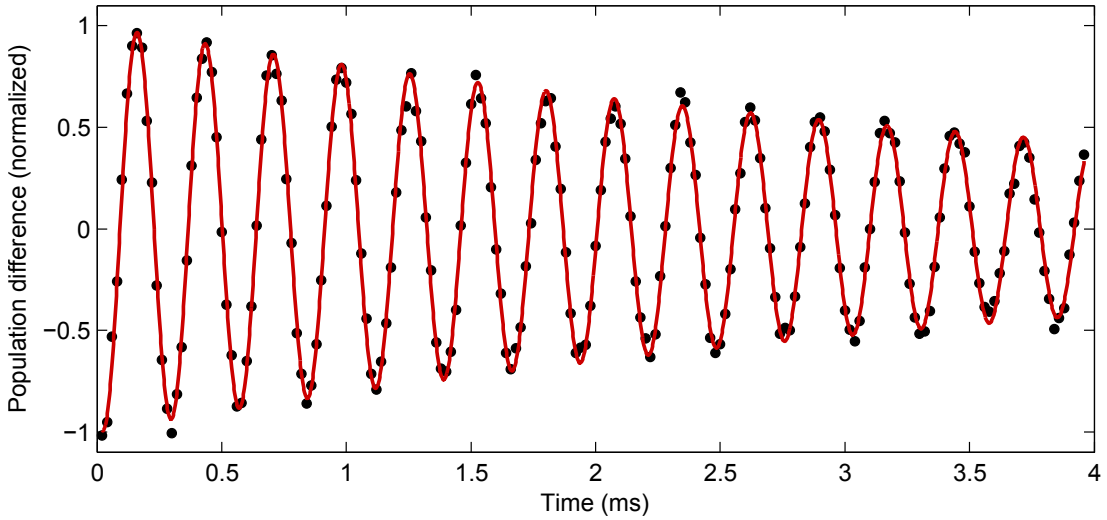

Figure 3.13.: Real time observation of Rabi oscillations in a single experimental run. Continuous microwave radiation coherently drives the transition between the clock states and the superposition state is read out approximately every 1.1 ms.

3.5.3. Observation of Atomic Projection Noise

3.5.3.1. Detection Scheme

We describe in this section the measurement of atomic projection noise, which serves as a calibration for the total atom number and can be seen as an intermediate step towards the realization of spin squeezing. For the preparation of a CSS on the equator of Bloch sphere, we apply a $\pi/2$-pulse around the x-axis, followed by a $\pi/2$-pulse around the y-axis to reject fluctuations in the power of the microwave source. The state is read out with a long detection pulse of 11 μs and a probe power of 1.1 mW. All atoms are repumped into $F = 2$ and the total atom number is measured. The probe power is chosen here with a lower probe power of 240 μW to avoid saturation of the demodulated signal. The atoms are then ejected from the trap by the application of a blast pulse with simultaneous repumping. After this, the background of the FM spectroscopy both for a high and low probe power is measured.

3.5.3.2. Data Treatment

For the detection of the atomic shot noise, all technical noise sources have to be below the projection noise limit. As an example, for an atom number of N_{at}=10^6, all technical noise contributions have to be below 0.1%. Such a stability level could not be obtained on our experiment for the total time of the measurements of several hours, and so we had to reject the technical noise below the required threshold with the data treatment. Below is a list of all noise rejection steps in the data treatment.

- **Background fluctuations** The background signal without atoms is subtracted from the signal for the projection noise measurement. This ensures that background fluctuations over one run do not add noise. The same is done for the full scale atom number measurement.
- **Atom number fluctuations** In each run, the projection noise measurement is normalized with respect to the full atom number. Furthermore, in the data treatment a filter of ±5% is used to reject runs with too high atom number fluctuations.
- **Probe frequency fluctuations** In some runs, the frequency lock of the probe laser jitters during the probe pulse for unknown reasons. We reject those runs by fitting each pulse of 11 μs with an exponential function[3] and reject all cases where the decay time is a factor of more then two away from the average value.
- **Probe power fluctuations** Runs with power fluctuations of more than ±5% of the average probe power are rejected.
- **Dipole trap fluctuations** We reject all runs in which the dipole trap power fluctuations are above 0.5% between succeeding experimental runs.
- **General rejection of long term fluctuations** We take the difference of the results from succeeding experimental runs, take the variance of the differences, and then divide it by two. For white noise (which is projection noise), this is equivalent of taking the variance of all measurements. In contrast, correlated noise (which technical noise usually is), is highly rejected with this two-point variance method.

[3]For very long probe pulses the atoms are slightly asymmetrically pumped to $F = 2$ which gives an exponential shape.

- **Manual rejection** We reject all runs in which we notice that the experiment does not operate as wanted. This is typically only the case when one of the dipole trap lasers unlocks from the optical cavity.

After the filtering, typically 50% to 80% of the runs are kept. All technical noise which spans more than two adjacent experimental runs is rejected by the two-point variance method. The other steps reduce the run-to-run fluctuations.

3.5.3.3. Results

In principle, the measurement of the atomic projection noise can be verified by preparing repeatedly a known number of atoms N_{at} in a CSS on the equator of the Bloch sphere, and verifying that the standard deviation in the number difference measurement is $\Delta N = \sqrt{N_{\mathrm{at}}}$. However, the probe beam has a waist similar to the size of the atomic cloud and therefore defines an effective atom number. We measure therefore the variance of the repeated CSS measurements as a function of the full scale signal. For the case of atomic shot noise, this should give a linear dependence.

The results of the measurements are shown in Figure 3.14. The probe pulse of 11 μs was cut such that only the first 1.5 μs are used for the CSS measurement. The power in the QND beam is 1.16 mW on the atoms and well over the photonic shot noise limit on the PD. Each experimental point in Figure 3.14 is the variance from 600-1100 experimental runs after filtering. The red line is a parabolic fit, the blue line is the linear contribution and the black line is the detection noise, which is independent of the atom number. The original data (not shown) contained only voltages for the full scale value (V_{at}) and the variance (V_{var}). The effective atom number was defined over the linear slope between V_{at} and V_{var},[4] which ensures the $\Delta N = \sqrt{N_{\mathrm{at}}}$ condition. The maximal effective atom number measured here is $N_{at} = 3.8 \times 10^5$,[5] which is consistent with typical atom numbers measured by absorption imaging from 8×10^5 to 10^6, and probe beam being of the size of the atomic cloud.

[4] In detail, we had $V_{\mathrm{var}} = P(1)V_{\mathrm{at}}^2 + P(2)V_{\mathrm{at}} + P(3)$. The atom number was defined via $N_{\mathrm{at}} = V_{\mathrm{at}}/P(2)$.

[5] Due to the significant number of experimental runs for Figure 3.14 ($\approx$ 15.000) the loading time of the dipole trap was chosen as short as possible. For a loading time as long as for absorption imaging we reached typically $N_{\mathrm{at}} = 5 \times 10^5$.

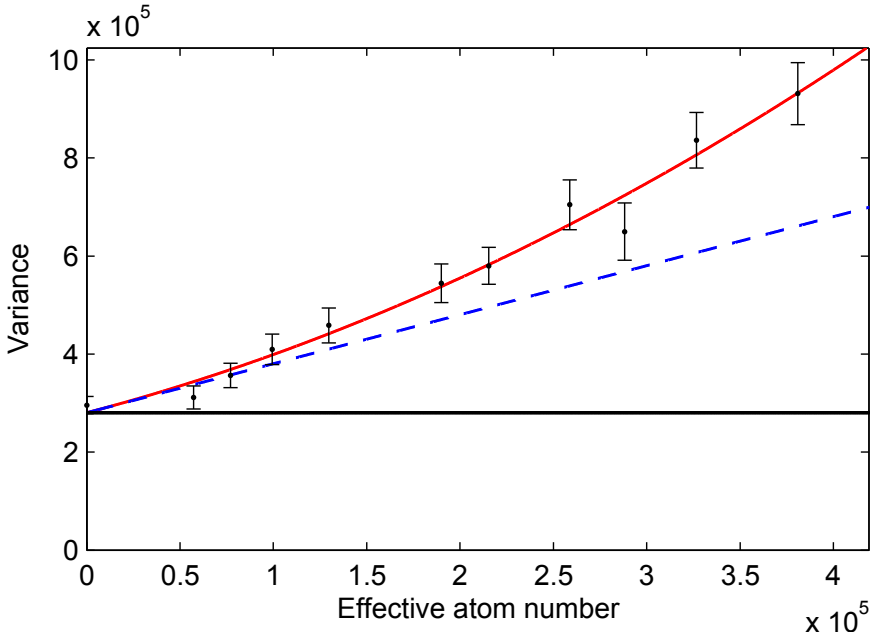

Figure 3.14.: Measurement of the atomic shot noise. The variance from the repeated measurement of CSSs on the equator of the Bloch sphere is plotted vs. the effective atom number. The black horizontal line is the detection noise dominated by the shot noise in the optical probe, the blue dashed line is the contribution from atomic shot noise, and the red line is a parabolic fit of the experimental data. The quadratic part in the scaling of the noise variance is due to technical noise.

From the quadratic contribution to the variance, we deduce a remaining technical noise level of $\sigma_{\mathrm{tec}} = 1.4 \times 10^{-3} N_{\mathrm{at}}$ from run to run which is not rejected. A likely candidate for this noise is the frequency lock of the probe laser. The beat-note of the probe laser with the repumper shows a noise spectrum with a width of a few MHz which is above the intrinsic typical linewidth of the ECDLs of 300 kHz. Since the bandwidth of the frequency lock is only 50 kHz, this indicates that the probe laser frequency can jitter in this range within the probe pulse time of 1.5 μs. A solution of this problem could consists in using a probe laser with a more narrow linewidth. An option is here to double a stable laser at 1560 nm, and to offset lock with a very small bandwidth on the repumer radiation.

The destructivity of the probe pulse of 1.5 μs leaves a residual coherence of 28%, which means that the largest part of the atomic state is destroyed after the long measurement pulse. We have at the maximum atom number a ratio between

atomic noise to shot noise of $\kappa = 1.16$ and therefore a reduction in the atomic shot noise by a factor $\xi = \sqrt{\frac{1}{1+\kappa^2}} = 0.65$. The decoherence for the given projectivity is therefore too high to either fulfill the Wineland or the Kitagawa-Ueda criterion for spin squeezing.

The treatment in this section has shown that one of the necessary conditions to obtain spin squeezing, the measurement of the atomic projection noise, can be fulfilled in our experiment. In the present configuration, spin squeezing could be reached by increasing the atom number but would at most lead to a few dB of squeezing. It is therefore planned to change to a cavity aided detection scheme. In an optical cavity, the photons interact several times with the atoms, while the photonic shot noise on the photodiode remains constant. With similar arguments as for the probe waist, then the shot noise from the light is reduced for the same destructivity. This improves the measurement by $\sqrt{F/\pi}$, the square root of the number of cycles in the cavity.

4. Feedback Control of Collective Spin States

4.1. Introduction

In this chapter, we show some of the first experimental demonstrations on the feedback control of the internal states of an atomic ensemble. Our work is similar to feedback schemes to prepare non-classical atomic states, as theoretically treated in [Thomsen 02], and with first experimental results in this direction in [Inoue 13] and [Behbood 13]. The main objective of our work instead is to present how with relative simple means a collective atomic quantum state can be protected against some of the dominating decoherence sources in atomic interferometers.

The class of decoherence we consider are random rotations of the collective pseudo-spin. Examples of corresponding noise sources are, depending on the experimental context, fluctuations of surrounding magnetic or electric fields, or also the phase noise of the local oscillator (LO) in an atomic clock. On the other hand, our feedback method is not able to prevent the decoherence from incoherent processes such as spontaneous emission.

In Section 4.2, we give a general description of the control problems which we will consider, and introduce different parameters that can be used to characterize our feedback system. The theoretical treatment is developed in close analogy to the description of the feedback control of a single qubit in [Brańczyk 07]. The experimental setup for the feedback control is described in Section 4.3.1.

We start in Section 4.3.2 with a simple noise model, where a coherent spin state (CSS) is rotated randomly either in one or another direction with a fixed angle and rotation axis. On this example, we derive analytical solutions for the controller efficiency in the weak measurement regime and give solutions for all the measurement strength regimes, also in the partially projective one, by Monte-Carlo simulations. From the theoretical treatment, we choose the state coherence as the best parameter to measure the efficiency of the experimental

feedback controller. We characterize the trade-off between gained information and destructivity, over which the feedback controller can be optimized. The noise action is then repeated on the same CSS, and it is demonstrated how the state can be preserved by feedback over time.

In Section 4.3.3, the noise model is extended to arbitrary angles in a given interval, which makes it more similar to a realistic disturbance. A short theoretical treatment in the weak measurement regime discusses the optimization of the feedback controller. After this, its ability to protect the coherence of a CSS is experimentally demonstrated. We discuss then in Section 4.3.3.3 in which scenarios the feedback scheme could be directly useful to increase the sensitivity of an atomic interferometer.

The work in this chapter shows that for particular quantum systems and noise models, a classical feedback approach can be efficient to protect a quantum system, in contrast to the case of a single qubit as in [Brańczyk 07]. This is the basis of the work in Chapter 5, where instead on performing feedback on the quantum system we perform feedback on its environment in order to prolong the coherence lifetime in an atomic clock.

4.2. General Description of the Control Problem

4.2.1. Decoherence by Collective Noise

We investigate noise which randomly rotates a collective spin around the Bloch sphere. At least one of the two rotation parameters, rotation axis or rotation angle, is random. Such noise creates a statistical mixture from a pure state, and the state decoheres. It transforms an initially pure CSS into a probabilistic mixture of CSSs and the output has to be described as a density matrix. We assume that the noise acts instantaneously and write the corresponding rotations as a set of Kraus operators of the form

$$N(\alpha,\gamma) = \sqrt{p(\alpha,\gamma)} R_x(\alpha) R_z(\gamma) , \tag{4.1}$$

where the rotation operators from Section 1.2.4 were taken, with $-\pi/2 \leq \alpha \leq +\pi/2$ and $-\pi \leq \gamma \leq +\pi$. We use here that the result of any rotation of a CSS on the Bloch sphere can be described with only two orthogonal rotations. The probability to perform such a rotation is then $p(\alpha,\gamma)$. The Kraus map of the

decoherence channel is

$$\mathcal{E}(\rho) = \int_{-\pi/2}^{+\pi/2} \int_{-\pi}^{+\pi} N(\alpha,\gamma)\, \rho N^{\dagger}(\alpha,\gamma)\; d\alpha\, d\gamma\ . \tag{4.2}$$

As discussed in the introduction, collective noise of this form can describe different decoherence sources in atomic interferometers. Most notably it can be used to describe the decoherence by the frequency noise of the LO in an atomic clock. Other decoherence sources could be intensity noise of the LO during the coherent manipulations on the Bloch sphere, or as well stray magnetic and microwave fields. The noise can be made time dependent by writing $p(\alpha,\gamma)$ as a function of time.

4.2.2. Feedback Control

We design now a general form of a feedback controller map as it might be used in an atomic interferometer. We want to describe a simple sequence, where an initially pure atomic state experiences collective noise, several measurements are taken, and a single feedback step is performed.

We assume that during the measurements that there are no state rotations. Only measurements the z-axis of the Bloch sphere with the measurement operator M_z can be performed directly in the experiment. Nevertheless, measurements along the x- and y-axis can be obtained by mapping the respective direction onto the z-axis, and turning the state back after the measurement. This is described with the generalized measurement operators

$$M_y = R_x(\pi/2)\, M_z R_x(-\pi/2)\ , \qquad M_x = R_x(\pi/2)\, M_z R_x(-\pi/2)\ . \tag{4.3}$$

The measurement operators M_x, M_y and M_z do not commute and their order and measurement strength has to be determined prior to the experiment. If we further assume that all measurements are taken in a row, then the full measurement operator can be written as $M_{x,y,z} \equiv M_x M_y M_z$. The conditional probability to measure the results $m = (x,y,z)$ given a noise with angles α and γ is $p(m|\alpha,\gamma)$. The feedback is performed with the rotations $C(\alpha',\gamma') = R_x(\alpha')\, R_z(\gamma')$. The dependence of the correction angles on the measurement results is called the controller law (e.g. $\alpha' = \alpha'(x,y,z)$), and has to be found and optimized with respect to a specific

feedback goal. We can write the full controller map including the noise action as

$$\mathcal{C}(\rho) = \int_{-\pi/2}^{+\pi/2} d\alpha \int_{-\pi}^{+\pi} d\gamma \int_{-\infty}^{+\infty} dm\; p(m|\alpha,\gamma) C\left(\alpha',\gamma'\right) M_m N\left(\alpha,\gamma\right) \times \rho N^{\dagger}\left(\alpha,\gamma\right) M_m^{\dagger} C^{\dagger}\left(\alpha',\gamma'\right) \ . \tag{4.4}$$

The feedback controller is in general a complex map which transforms one density matrix to another one. In Equation (4.4), several assumptions have been made such as successive noise and measurement operations, which are not fulfilled in most realistic situations. Nevertheless, the goal of this chapter is to obtain a simple set of easily comprehensible and testable models. This will be used to highlight the experimental and theoretical challenges for the active state control in an atomic interferometer, and point out the directions for further study. Note that dissipative processes, as for example the simple state re-preparation by optical pumping, are not considered in the feedback action in Equation (4.4), since in general the phase information in an atomic interferometer shall be preserved.

4.2.3. Feedback Efficiency

We set the feedback goal to recover the same state as before the noise action. A feedback controller can be optimized with respect to several parameters, and its exact form will therefore depend on the choice of the feedback criterion. We choose here to analyze the feedback efficiency via the fidelity, the von Neumann entropy and the coherence which are defined below.

Fidelity. The fidelity is defined as the projection of the output state ρ_{out} on the input one $|\psi_0\rangle$, $\mathcal{F}\left(\rho_{\text{out}}, |\psi_0\rangle\right) \equiv \langle\psi_0| \rho_{\text{out}} |\psi_0\rangle$. The feedback controller is efficient if the output state is closer to the input state than without feedback action. The fidelity is a commonly used parameter in quantum information science to characterize the performance of state operations.

Von Neumann entropy. The von Neumann entropy of a system with density operator ρ is $S(\rho) \equiv -\mathrm{Tr}\left(\rho \log_2 \rho\right)$. It is both used in quantum information to characterize the overall information content of a system and in general in quantum statistical mechanics. Similarly as in classical mechanics, the feedback controller is efficient if it reduces the entropy of the system.

Coherence. The coherence is defined as the norm of the mean Bloch vector

normalized to its maximal possible value: $\eta(\rho) \equiv \|\langle \mathbf{J} \rangle\| / J$, where $\langle \mathbf{J} \rangle = (\langle J_x \rangle, \langle J_y \rangle, \langle J_z \rangle)$ and $\langle J_k \rangle = \mathrm{Tr}(J_k \rho)$. Coherence is an essential feature of quantum systems and the performance of an atomic interferometer is directly proportional to the coherence of the atomic system, since a higher coherence implies a higher interferometric contrast. A feedback controller is therefore efficient if it increases the coherence of the atomic system.

In Section 4.3.2.1, the quantities above are used for a theoretical evaluation of the feedback control of collective spin states. The only parameter used for the experimental part will be the state coherence, because it is the one which can be most easily accessed experimentally.

4.3. Experimental Implementation

4.3.1. Experimental Setup

The experimental setup is updated with respect to the one in the previous chapter by the addition of a phase shifter on the LO to be able to rotate the atomic state in any direction around the x- and y-axis of the Bloch sphere, a quantum random number generator (QRNG) to set the random parameters of the noise, and a micro-controller to calculate and send the feedback signal. The complete experimental setup is shown in Figure 4.1.

The commercial QRNG (Quantis, from Id-Quantique) employs single photons on a 50/50 beam splitter and two photodiodes which detects transmission "1" or reflection "0" events. The random bits are sent with a bit rate of 4 Mbits/sec together with a clock counter. A single random bit is used to set the rotation direction, whereas N bits are combined to set the rotation angle. The phase shifter for the state rotations was originally designed for Quadrature Phase-Shift Keying (QPSK), which is a digital modulation technique used for data transfer, and which shifts the phase of a carrier wave to 4 different possible phase positions. A QPSK phase shifter at 165 MHz (AD8345, from Analog Devices) was soldered on a homemade electronic board and connected to the output from the RF generator before the mixing with the 7 GHz from the frequency chain.

As the feedback controller serves a micro-controller unit (MCU, ADuC814, from Analog Devices). It was chosen because of its on-board 12 bit analog-to-digital (ADC) and digital-to-analog convertors (DAC). Nevertheless, only integer

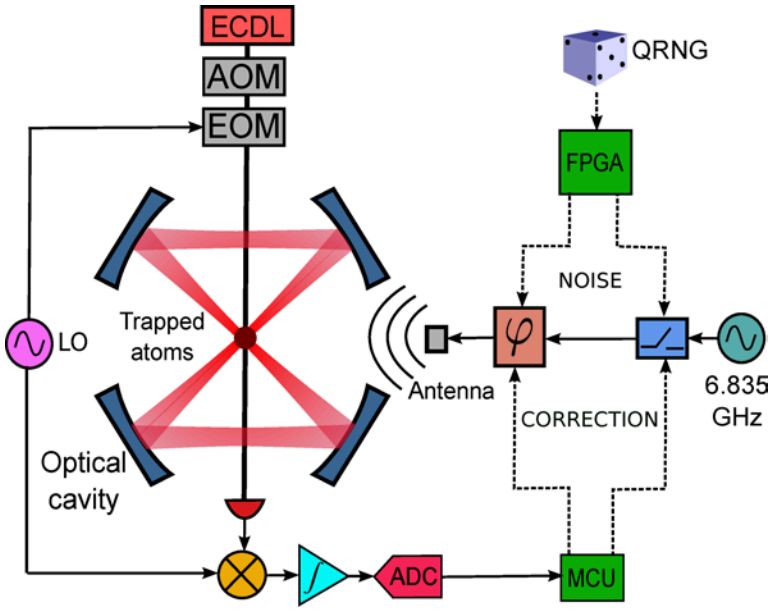

Figure 4.1.: Experimental setup. A FPGA (field-programmable gate array) card controls the amplitude and phase of microwave radiation shined onto the atoms, which is chosen from the input from a quantum random number generator (QRNG). The atomic state is measured with the nondestructive detection system, the result is analogically integrated and digitized with an analog-to-digital convertor (ADC), and sent to a micro-controller unit (MCU). Feedback is then performed with microwave pulses with a controlled phase.

operations with positive numbers could be directly programmed on the MCU, and the additional constraint of a low calculation speed of the micro-controller made the experimental work unnecessarily difficult. We therefore recommend for future feedback experiments in atom interferometry to use controllers which have a better performance and are more versatile, for example FPGAs equipped with external ADCs/DACs.

For the experimental results in this chapter, the beam size for the nondestructive measurements is 245 μm. The other parameters are the ones from Section 3.4.2, with the carrier locked at 3.291 GHz, a modulation frequency of 3.4213 GHz and a modulation depth of 5%.

4.3.2. Study of Binary Collective Noise

4.3.2.1. Theoretical Description

We consider at the beginning the decoherence by a simple noise model, a random rotation of the collective state around a fixed axis and a fixed angle, but whose rotation direction (up/down) is unknown. This represents both experimentally and theoretically an easy configuration, and lays the basis for the study of more complex situations. As seen in Figure 4.2 in the Bloch sphere picture, a superposition state is either rotated up or down, weakly measured, and finally rotated back to the initial state if the state was correctly measured. We study at first theoretically the efficiency limits of this process and then proceed to the experimental demonstration.

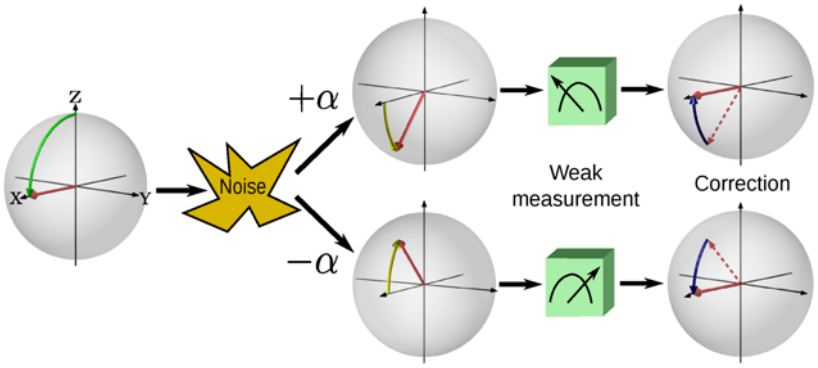

Figure 4.2.: Bloch sphere description of the feedback problem with binary collective noise. A CSS decoheres by binary collective noise and the feedback controller recovers the initial state.

The decoherence $\rho \mapsto \mathcal{E}_\alpha(\rho)$ by a binary random collective rotation of an angle α around the x-axis of the Bloch sphere is described by

$$\mathcal{E}_\alpha(\rho) = \frac{1}{2} R_x(\alpha)\, \rho R_x^\dagger(\alpha) + \frac{1}{2} R_x(-\alpha)\, \rho R_x^\dagger(-\alpha)\,. \tag{4.5}$$

If the noise acts on an initial CSS $|\psi_0\rangle \equiv |\pi/2\rangle$, the state will decohere into a statistical mixture of the states $|\pi/2+\alpha\rangle$ and $|\pi/2-\alpha\rangle$. The density operator after the noise action is therefore

$$\mathcal{E}_\alpha(\rho_0) = \frac{1}{2}\rho\left(\frac{\pi}{2}+\alpha\right) + \frac{1}{2}\rho\left(\frac{\pi}{2}-\alpha\right), \tag{4.6}$$

where $\rho_0 \equiv |\psi_0\rangle\langle\psi_0|$ and $\rho(\theta) \equiv |\theta\rangle\langle\theta|$.

For the feedback controller, it suffices to determine the hemisphere in which the CSS lies and to apply a rotation in the opposite direction. If the rotation is considered perfect, the limit for the feedback efficiency is then set by the properties of the measurement. A low measurement precision implies control errors, over which the state could be even further destroyed. On the other hand, the measurements can also directly destroy the atomic state, either by incoherent processes like spontaneous emission, or by (partial) projection. In the following analysis, we assume that spontaneous emission and dephasing are negligibly low. The feedback efficiency is then governed by a trade-off from the measurement precision to avoid both control errors and the projection of the state. The different feedback efficiency criteria from Section 4.2.3 are applied to this scenario to illustrate how the measurement back-action will ultimately limit the performance of the feedback controller.

The Gaussian measurement operator on the z-axis from Equation (3.6) is

$$M_{m_0} = \left(2\pi\sigma_{\mathrm{det}}^2\right)^{-1/4} e^{-\frac{1}{4\sigma_{\mathrm{det}}^2}(J_z - m_0)^2}, \tag{4.7}$$

where σ_{det} is the measurement uncertainty expressed in the angular momentum basis, and m_0 is the measurement result. The probability for the measurement result m_0 is given by

$$\begin{aligned} p(m_0|\theta,\varphi) &= \langle\theta,\varphi| M_{m_0}^\dagger M_{m_0} |\theta,\varphi\rangle & (4.8)\\ &= \frac{1}{\sqrt{2\pi}}\frac{\xi_\theta}{\sigma_{\mathrm{det}}} \exp\left[-\frac{\xi_\theta^2 (m_0 - J\cos\theta)^2}{2\sigma_{\mathrm{det}}^2}\right]. & (4.9) \end{aligned}$$

As defined in Chapter 1, $\kappa^2 = \sigma_J^2/\sigma_{\mathrm{det}}^2$ is the squared measurement strength and $\xi_\theta^2 = 1/\left(1 + \kappa^2 \sin^2\theta\right)$ is the squared squeezing factor. The probability to determine the right hemisphere is then the integral of the probability of all measurement results m_0 which have the same sign as the mean spin vector,

$$\begin{aligned} p_s &= \int_0^\infty p(m_0|-\alpha)\, dm_0 & (4.10)\\ &= \frac{1}{2}\left[1 + \mathrm{erf}\left(\sqrt{J\xi_{\pi/2-\alpha}^2\kappa^2}\sin\alpha\right)\right]. & (4.11) \end{aligned}$$

According to the measurement result, the feedback controller rotates the state up or down. The full feedback controller action is described by the map

$$\begin{aligned}\mathcal{C}_\alpha(\rho) &= \frac{1}{2}\int_{-\infty}^{0} dm_0 \Big\{ p(m_0|+\alpha)\, R_x(-\alpha)\, M_{m_0} R_x(+\alpha)\, \rho R_x(+\alpha)^\dagger\, M_{m_0}^\dagger R_x^\dagger(-\alpha) \\ &\qquad + p(m_0|-\alpha)\, R_x(-\alpha)\, M_{m_0} R_x(-\alpha)\, \rho R_x^\dagger(-\alpha)\, M_{m_0}^\dagger R_x^\dagger(-\alpha) \Big\} \\ &\quad + \frac{1}{2}\int_{0}^{\infty} dm_0 \Big\{ p(m_0|-\alpha)\, R_x(\alpha)\, M_{m_0} R_x(-\alpha)\, \rho R_x^\dagger(-\alpha)\, M_{m_0}^\dagger R_x^\dagger(+\alpha) \\ &\qquad + p(m_0|+\alpha)\, R_x(+\alpha)\, M_{m_0} R_x(+\alpha)\, \rho R_x^\dagger(+\alpha)\, M_{m_0}^\dagger R_x^\dagger(+\alpha) \Big\}\end{aligned} \tag{4.12}$$

In the weak measurement limit, analytical expressions for the feedback efficiency can be obtained. With Equation (4.11) and assuming a negligible projectivity ($M_{m_0} \sim 1$), the controller map becomes

$$\mathcal{C}_\alpha(\rho) \sim p_s \rho + \frac{1-p_s}{2}\left[R_x(2\alpha)\,\rho R_x^\dagger(2\alpha) + R_x(-2\alpha)\,\rho R_x^\dagger(-2\alpha)\right]. \tag{4.13}$$

In other words, the feedback controller recovers the initial state with a probability p_s or doubles the initial angle θ with a probability 1-p_s. The controller map can be inserted into the definitions of the von Neumann entropy, fidelity and coherence from Section 4.2.3 to evaluate the efficiency of the controller. The results for the different parameters are summarized in Table 4.1. The full derivation of the expressions in Table 4.1 can be found in Appendix E.

	$\|\psi_0\rangle$	$\mathcal{E}_\alpha(\rho_0)$	$\mathcal{C}_\alpha(\rho_0)$
Fidelity	1	$e^{-2J\alpha^2}$	$p_s + (1-p_s)\, e^{-2J\alpha^2}$
Entropy	0	1	$-p_s \log_2 p_s + (1-p_s)\,[1 - \log_2(1-p_s)]$
Coherence	1	$\lvert\cos\alpha\rvert$	$p_s + (1-p_s)\cos 2\alpha$

Table 4.1.: Coherence, entropy and fidelity for a CSS after the noise action ($\mathcal{E}_\alpha(\rho_0)$) and after the feedback ($\rho_{\text{out}} = \mathcal{C}_\alpha(\rho_0)$) in the weak measurement regime and assuming no other decoherence sources than the collective noise.

Without any other decoherence sources than the collective noise, the different feedback efficiency criteria only depend on the success probability p_s. The evolution

of the fidelity, entropy and coherence is illustrated in Figure 4.3 for a fixed noise angle of $\alpha{=}\frac{\pi}{4}$.

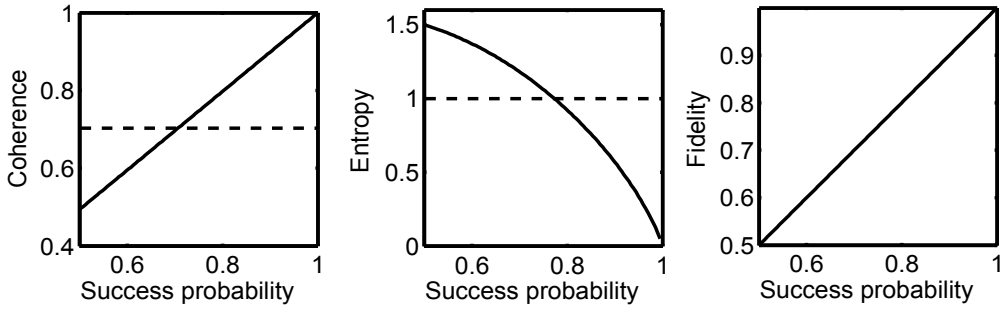

Figure 4.3.: Coherence, von Neumann entropy and fidelity after the feedback versus the success probability for a noise angle of $\alpha = \pi/4$ and in the limit of a large atom number ($N_{\mathrm{at}} \to \infty$), i.e. always in the weak measurement regime. The dotted lines are the values after the noise but without feedback and are therefore the limit above which the controller is efficient.

For the specific noise and feedback controller model, the fidelity always increases and approaches a value of one for $p_s \to 1$ because the initial state is fully recovered. Similarly, for $p_s \to 1$, the entropy approaches 0 and the coherence 1 as expected for a pure state. In contrast, for too low values of p_s, the feedback controller decreases the coherence of the state, and increases the entropy.

To compare the different parameters, we can define the critical success probabilities $\bar{p_s}^{(e)}(\alpha)$ (entropy),$\bar{p_s}^{(f)}(\alpha)$ (fidelity) and $\bar{p_s}^{(c)}(\alpha)$ (coherence), above which the feedback controller is efficient for the corresponding quantities. For the fidelity criterion, $\bar{p}_s^{(f)} = 0$ and the feedback controller is always efficient, because it suffices that only sometimes the initial state is recovered. Also, the critical success probability for the entropy is independent of the noise angle α with a value $\bar{p}_s^{(e)} \sim 0.77$. The critical success probability for the coherence with $\pi/2 \leq \alpha \leq \pi/2$ is

$$\bar{p}_s^{(c)}(\alpha) = \frac{\cos\alpha - \cos 2\alpha}{2\sin^2\alpha}. \tag{4.14}$$

For $\alpha = \pi/2$, $\bar{p}_s^{(c)} = 1/2$, and it increases to $\bar{p}_s^{(c)} = 3/4$ when $\alpha = 0$. The feedback controller is therefore efficient in different parameter regimes with $\bar{p}_s^{(f)} < \bar{p}_s^{(c)}(\alpha) < \bar{p}_s^{(e)}$ and the entropy efficiency criterion is the hardest to fulfill.

The above results are only valid for no decoherence by the state detection and negligible measurement backaction. For a finite number of particles, the latter condition cannot be fulfilled for all values of the success probability p_s. Instead of the success probability p_s, the measurement strength $\kappa = \frac{\sigma_J}{\sigma_{\mathrm{det}}}$ becomes then the critical parameter, which defines both the success probability *via* Equation (4.11) and the projectivity of the measurements. Since the measurement modifies the state as described in Chapter 1, it can be expected that the feedback efficiency criteria reaches an optimum for values of $\kappa < \infty$ and therefore for success probabilities which are smaller than one.

Instead of attempting an analytical solutions, a Monte-Carlo simulation is used to study the controller action for a fixed number of particles $N_{\mathrm{at}} = 100$, and two different noise angles $\alpha = \frac{\pi}{4}$ and $\alpha = \frac{\pi}{8}$. The simulation starts by preparing an initial $|\psi_0\rangle = |\pi/2\rangle$, which randomly experiences a rotation $R_x(\alpha)$ or $R_x(-\alpha)$ calculated from Equation (1.26) for collective rotations. The probability distribution for the measurement outcome m_0 is calculated from Equation (4.9) and a random value from the distribution is drawn. The measurement operator from Equation (4.7) is then applied to determine the state after the measurement, and finally from the sign of m_0 the direction for the correction by the feedback controller is chosen to be up or down.

In Figure 4.4, examples for one feedback cycle are shown for $\alpha = \frac{\pi}{4}$ and different measurement strengths. For low measurement strengths (e.g. κ=10^{-3}), the wavefunction always stays approximately Gaussian but the probability of a wrong feedback correction is close to 50% and the state can be rotated to the poles of the Bloch sphere leading to a delta-Dirac shaped wavefunction. For high measurement strengths (e.g. κ=50), the state is wrapped by the measurement backaction in a Banana-like shape around the Bloch sphere as expected for squeezed spin states (SSS). The feedback controller almost always applies the right counter rotation but the rotation creates a non-Gaussian wavefunction from the squeezed spin state. Since the length of the mean spin vector is reduced for a SSS with respect to a CSS, the coherence of the state is reduced. Furthermore, but not contained in the coherence criterion, the uncertainty along the z-axis is increased with respect to a CSS, which would additionally decrease the sensitivity in an atomic interferometer.

The simulation is repeated for 1000 trajectories for different measurements strengths. The coherence is calculated from the mean spin length averaged over all

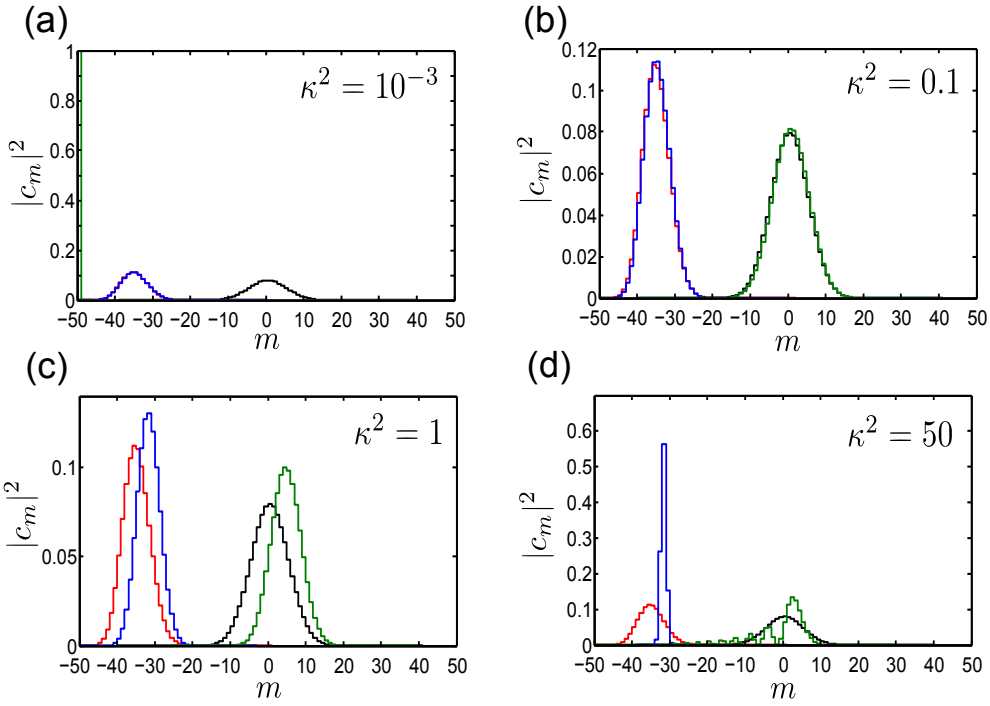

Figure 4.4.: Example distributions of the atomic wavefunction in the basis $\{|m\rangle\}$ for different values of κ^2 with $\alpha = \pi/4$ and $N_{\mathrm{at}} = 100$. One sees the initial CSS (black), the state after the noise action (red), after the measurement (blue) and after the correction (green). (a) The measurement does not modify the state, but the feedback controller rotates the state by mistake on the south-pole of the Bloch sphere. (b) The state is projected only very weakly and rotated back. (c) The state is partially projected and rotated back. (d) The state is strongly projected and is spread over the z-axis of the Bloch sphere after the feedback.

trajectories and the fidelity is the average from the projection of each final state on the initial CSS. The von Neumann entropy is $S = -\mathrm{Tr}(\overline{\rho_{\mathrm{out}}} \log_2 \overline{\rho_{\mathrm{out}}})$ with

$$\overline{\rho_{\mathrm{out}}} = \frac{1}{N_{\mathrm{traj}}} \sum_{k=1}^{N_{\mathrm{traj}}} |\psi_{\mathrm{out}}(k)\rangle \langle\psi_{\mathrm{out}}(k)| \,, \tag{4.15}$$

where N_{traj} is the number of simulated trajectories and $|\psi_{\mathrm{out}}(k)\rangle$ is the output state for each trajectory. The results for the different feedback efficiency criteria for measurement strengths from κ=10^{-5} to κ=10^2 are shown in Figure 4.5 for an angle of $\alpha = \frac{\pi}{4}$ (black squares) and $\alpha = \frac{\pi}{8}$ (blue triangles) and $N_{\mathrm{at}} = 100$.

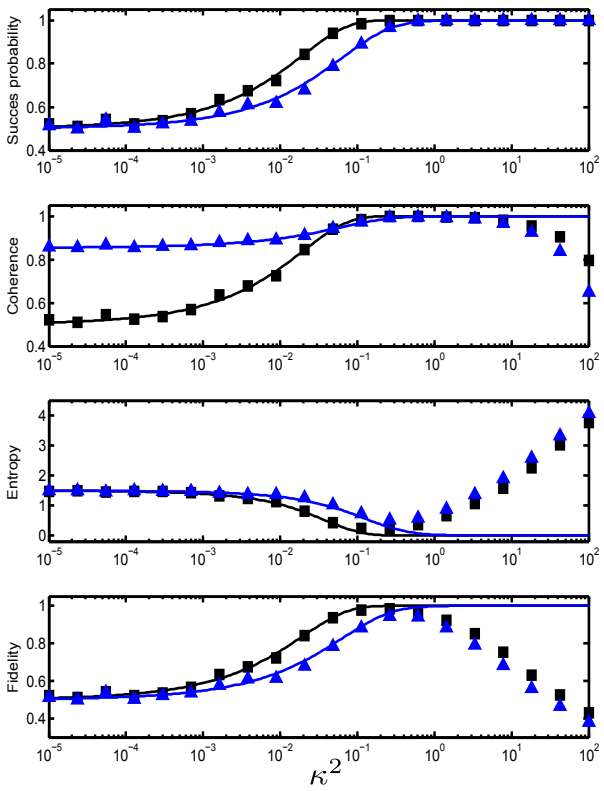

Figure 4.5.: Success probability, coherence, entropy and the fidelity after the feedback as a function of the squared measurement strength κ^2 for $\alpha = \pi/4$ (black squares) and $\alpha = \pi/8$ (blue triangles). In the Monte-Carlo simulation $N_{\mathrm{at}} = 100$ atoms were used and the results are the average from 1000 trajectories. The solid lines are the analytical results from the weak measurement limit and are therefore not valid outside ($\kappa^2 > 1$).

In Figure 4.5, the analytical solution from the weak measurement regime is drawn in solid black and blue lines. Instead of increasing efficiencies with higher measurement strengths and therefore higher success probabilities, optima are reached for a finite measurement strengths. Furthermore, the optima for the different parameters are close to each other in the region of $1 < \kappa^2 < 10$, and therefore in the partially projective regime. Only the success probability follows the analytical solution in all the measurement regimes, since the result is independent of the measurement backaction. Interestingly, for our specific noise model and feedback controller, the fidelity and entropy of the output state are

always more favorable for a higher noise amplitude than for a smaller one ($\alpha = \frac{\pi}{4}$ instead of $\alpha = \frac{\pi}{8}$), since both parameters are strongly dependent on the success probability, which is higher for a high noise angle for the same measurement strength.

The main result from Figure 4.5 is that even in the absence of additional decoherence sources related to the state measurement, the state projection prevents for the presented feedback scheme that an initial CSS can be perfectly stabilized against the noise from the environment. The question is if a better feedback controller can at least partially overcome this limitation. A possibility could be here to apply strategies close to weak measurement reversal methods. It could be for example interesting to attempt a partially projective measurement of a SSS along its elongated axis and so to "unsqueeze" it in accordance with the Schrödinger-Robertson uncertainty relation. In this way the state could be restored close to the initial CSS.

4.3.2.2. Experimental Results

All experimental results presented in the following are obtained in the weak measurement regime, where the back-action from the measurements can be neglected. We consider only the coherence as an efficiency criterion for the feedback controller since the it can be easily measured experimentally. We take the concept of the coherence measurement from optics, where the fringe contrast after an interferometer corresponds to the coherence of the output state. Equivalently, we take the atomic coherence from the fringe contrast at the end of a Ramsey interferometer. The crucial parameter for the feedback action is the success probability. In the weak measurement regime, Equation (4.11) becomes

$$p_s = \int_0^\infty p(m_0|-\alpha)\,\mathrm{d}m_0 = \frac{1}{2}\left[1 + \mathrm{erf}\left(\frac{J\sin\alpha}{\sqrt{2}\sigma_{\mathrm{det}}}\right)\right] , \tag{4.16}$$

where it is important to note that σ_{det} is expressed in the units of the spin variables. The analytical solution for coherence in the weak measurement regime in the previous section should be modified for the decoherence from the optical probe, and the output coherence after the feedback action becomes

$$\eta_\alpha^{\mathrm{out}} = \left[p_s + (1-p_s)\cos(2\alpha)\right]\ e^{-\gamma N_{\mathrm{ph}}} , \tag{4.17}$$

where the atomic state decays exponentially with a decay constant γ because of the spontaneous emission induced by N_{ph} probe photons. Since both the decay by spontaneous emission and the measurement uncertainty are a function of the photon number, there will be an optimal photon number where the coherence is maximal for a given noise angle.

We experimentally study the error-destructivity trade-off for $\alpha = \pi/4$. We first prepare the initial CSS $|\,\theta = \pi/2\,\rangle$ by optically pumping the atoms in $|\,0\,\rangle$ and applying a $\pi/2$ microwave pulse of duration $\tau_{\pi/2} = 75.6(2)$ μs. The noise is sent as a $\alpha = \pi/4$ microwave pulse, but with a random direction, chosen with the QRNG. The measurement contains a 1.5 μs long probe pulse with a varying photon number. The voltage after demodulation is analogically integrated and given to the input of the analog-to-digital convertor of the MCU. After a comparison with the background value, obtained from the average over 16 measurements in the previous run and saved in the MCU, the rotation direction for the feedback is decided by the controller and a $\pi/4$ correction pulse is sent. To determine the coherence of the atomic state at the end of the cycle, we send a second $\pi/2$-pulse to close the Ramsey interferometer. The direction of the last $\pi/2$-pulse is chosen alternately from run-to-run down or up to measure either the minimum or maximum of the fringe. The atoms are then repumped into $F = 2$ to measure the full atom number and the output of the Ramsey interferometer is normalized to this value in each run to reject atom number fluctuations.

In Figure 4.6 the result of the measurement of the residual coherence as a function of the photon number per sideband is shown. The measured points (solid squares) are obtained from 50 repetitions of the contrast measurement, and the error bars are the standard error of the measurement. The curve is fitted from Equation (4.17) with

$$\eta_{\pi/4}^{\mathrm{out}} = p_s \; e^{-\gamma N_{\mathrm{ph}}} \; , \tag{4.18}$$

where p_s is the success probability from Equation (4.16). The shape of the coherence curve has two main contributions, one an error function from the success probability, dominating at low photon numbers, and the second an exponential decay from spontaneous emission dominating at high photon numbers. The weak measurements were in this experiment not limited by photon shot noise but by technical noise, most likely due to amplitude noise of the detection laser in the experiment. The measurement uncertainty in Equation (4.16)

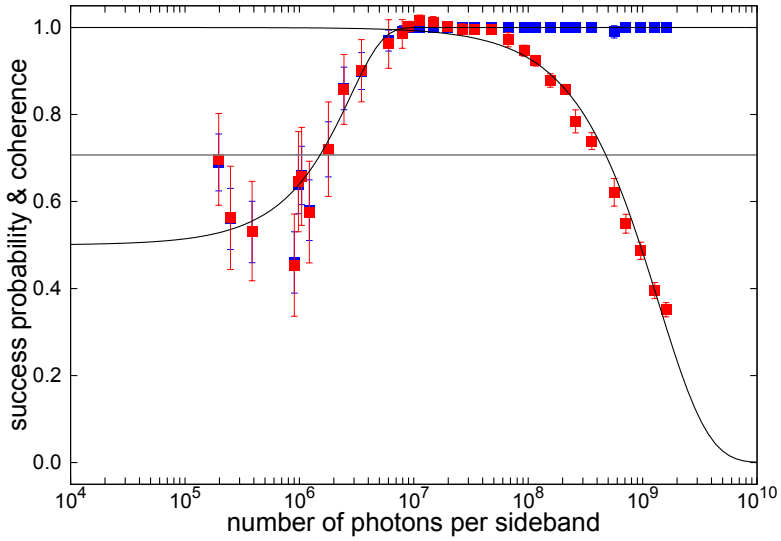

Figure 4.6.: Coherence of the atomic state after feedback as a function of the number of photons in the optical probe. The coherence (red squares) shows a trade-off between the information gained from the optical probe and its destructivity. The success probability for the feedback controller to make the right rotation is shown in blue squares and always increases with the photon number. For low photon numbers, it overlaps with the directly measured coherence.

is therefore inversely proportional to the photon number and the fit gives a value of $\sigma = 9.6(5) \times 10^{11}/N_{\mathrm{ph}}$, consistent with the value directly measured in Section (3.4.4). The state decay by spontaneous emission per probe photon from the fit is $\gamma = 7.6(4) \times 10^{-10}$. From the trade-off between the decoherence by spontaneous emission and the measurement uncertainty a maximum output coherence of 0.993(1) is reached for 9.1×10^6 photons per sideband. The feedback scheme is efficient for a wide range of photon numbers, and exceeds the coherence without feedback of $\eta_{\pi/4} = 1/\sqrt{2}$ from 2×10^6 to 5×10^8 photons.

To further confirm Equation 4.17, we measured the success probability p_s independently: the rotation directions set by the noise and by the feedback controller were saved during several experimental repetitions, and p_s was calculated off-line from how often the feedback controller took the right decision. The result is shown with blue squares in Figure 4.6 and fitted with Equation (4.16). Since $\eta_{\pi/4}^{\mathrm{out}} = p_s$ without other decoherence sources, one sees directly that the output coherence

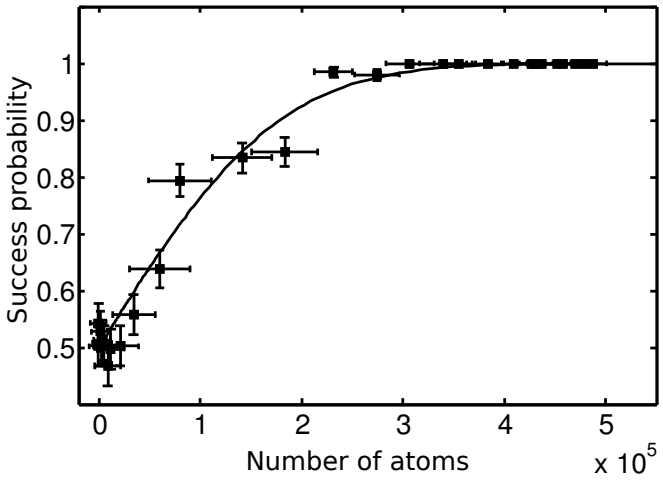

Figure 4.7.: Success probability versus the number of atoms for 1.4×10^7 photons per sideband and $\alpha = \pi/4$.

fits to the simple model developed in Section 4.3.2.1 when it is multiplied with the decoherence from spontaneous emission.

The success probability and therefore the output coherence is not only a function of the photon number, but as well of the atom number N_{at}. The photon number fixes the measurement uncertainty which has to be compared to the full scale value of the atomic spin which is proportional to the atom number. For $\alpha = \pi/4$, the success probability scales from Equation (4.16) as

$$p_s = \frac{1}{2}\left[1 + \mathrm{erf}\left(\frac{N_{\mathrm{at}}}{4\sigma_{\mathrm{det}}}\right)\right] , \tag{4.19}$$

which is confirmed in Figure 4.7 by scanning the success probability vs. the number of atoms. The photon number was fixed to 2.8×10^7 photons per sideband. To change the atom number, the repumper power in the MOT phase was varied while keeping all the other experimental parameters are constant. The measurement uncertainty obtained at this photon number is $\sigma_{\mathrm{det}} = 4.9 \times 10^4$, consistent with the result obtained in Figure 4.6.

So far, we only treated situations consisting of a single cycle of decoherence and successive correction. It is interesting to see how a feedback controller can protect

the coherence of an atomic state against a decoherence source over time. To design a simple scenario of this form we iterate the cycle binary noise - measurement - correction several times for a noise angle of $\alpha = \pi/4$ with a repetition time of 140 μs. A direct measurement of the state coherence for each number of noise and correction cycles would be experimentally too time consuming. We therefore instead only record the rotation directions for 200 experimental repetitions. This allows us to reconstruct the average population for each possible mean spin direction for each iteration and therefore the evolution of the coherence, once the other decoherence sources are characterized.

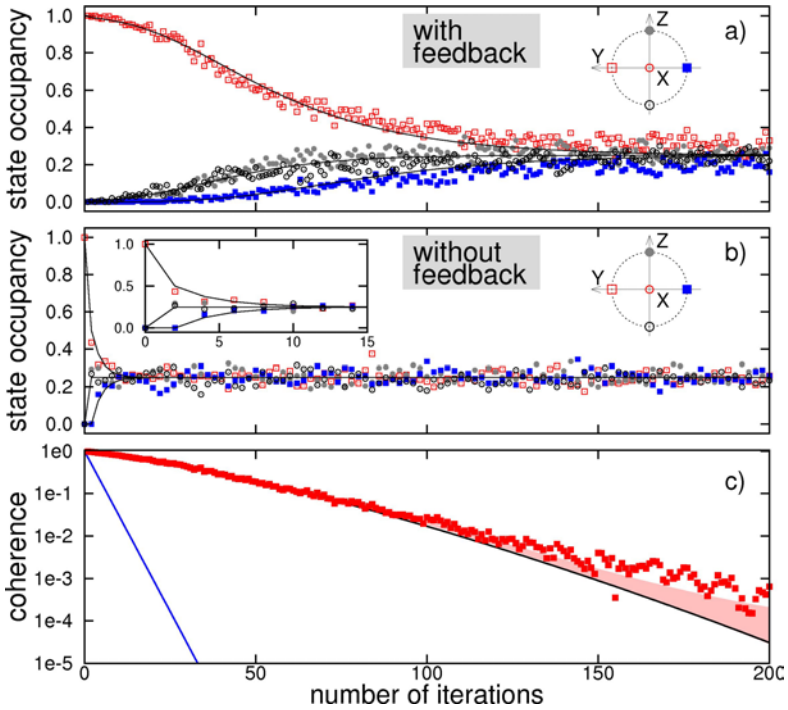

Figure 4.8.: State and coherence evolution with and without feedback. (a) State occupancy with feedback versus the number of cycles for the state $|0\rangle$ (solid circles), $|\pi/2\rangle$ (open squares), $|\pi\rangle$ (open circles) and $|3\pi/2\rangle$ (solid squares). (b) State occupancy without feedback correction. Inset: State occupancy for the first 15 cycles. The solid lines with and without feedback are drawn from the return probabilities at each cycle. (c) State coherence with (black line) and without (blue line) feedback. The experimental points with feedback are above the black line because of a limited statistical sample size of 200 runs.

The population of the atomic states with feedback is shown in Figure 4.8(a). After the feedback correction, only the states $|\pi/2\rangle$, $|0\rangle$, $|\pi\rangle$, and $|3\pi/2\rangle$ are populated. Without any other decoherence sources, a steady state population of the different angular positions would be expected, corresponding to the probabilities of the return paths to each position. Nevertheless, at each cycle p_s decreases because of the decoherence from the dephasing in the dipole trap and due to the spontaneous emission induced by the measurement probe, and therefore the probability to return to the initial state $|\pi/2\rangle$ is reduced for each iteration. The solid lines are drawn taking into account the initial measurement uncertainty and the decrease of p_s for each cycle.

Without feedback, the state vector diffuses quickly around the Bloch sphere (Figure 4.8(b)) under the action of the collective noise. For even iterations, only the states $\{|0\rangle, |\pi/2\rangle, |\pi\rangle, |3\pi/2\rangle\}$ are occupied and for odd iterations the states $\{|\pi/4\rangle, |3\pi/4\rangle, |5\pi/4\rangle, |7\pi/4\rangle\}$. The coherence of the state with and without feedback can be calculated from the norm of the mean spin directions multiplied with the residual coherence after dephasing and spontaneous emission. The coherence $\eta(\rho)$ is calculated from the measured probability p_k to occupy each angular position,

$$\eta(\rho) = \sqrt{\left(\sum_k p_k \sin\theta_k\right)^2 + \left(\sum_k p_k \cos\theta_k\right)^2}, \tag{4.20}$$

which gives the mean spin length of the statistical mixture. The residual coherence taking all decoherence sources into account is shown in Figure 4.8. Without feedback, the coherence decays with ${\eta_{\pi/4}}^N = 1/2^{N/2}$ and the Gaussian decoherence from the trap. With feedback, the coherence of the state is strongly increased and the coherence lifetime of the state is improved by one order of magnitude. For example for 10 iterations the coherence is increased from 0.03 to 0.77.

4.3.3. Study of Analog Collective Noise

4.3.3.1. Theoretical Description

The binary noise model in the previous section is now extended to arbitrary noise angles, but still with a fixed rotation axis. We treat only the case where all measurements are in the weak measurement regime as in our experimental configuration, and only investigate the coherence criterion. As a decoherence model, we set the noise angle α to be uniformly distributed in $[-\pi/2, +\pi/2]$. The set of

Kraus operators related to this decoherence channel is

$$E(\alpha) = R_x(\alpha)/\sqrt{\pi},\ -\pi/2 \leq \alpha \leq +\pi/2\ , \tag{4.21}$$

which generates the map

$$\mathcal{E}(\rho) = \frac{1}{\pi}\int_{-\pi/2}^{+\pi/2} R_x(\alpha)\,\rho R_x^{\dagger}(\alpha)\ d\alpha\ , \tag{4.22}$$

where the prefactor arises from the completeness condition $\int_{-\pi/2}^{+\pi/2} E(\alpha)\,E^{\dagger}(\alpha) = 1$. As in the previous section, we choose $|\pi/2\rangle$ as the initial state. After the decoherence action from Equation (4.22), the output state is

$$\mathcal{E}(|\pi/2\rangle) = \frac{1}{\pi}\int_{-\pi/2}^{+\pi/2} \rho(\pi/2+\alpha)\ d\alpha\ , \tag{4.23}$$

and the coherence of this statistical mixture is (see derivation in Appendix E)

$$\eta\left[\mathcal{E}(|\pi/2\rangle)\right] = \frac{1}{\pi}\left|\int_{-\pi/2}^{+\pi/2} e^{i\alpha}\,d\alpha\right| = \frac{2}{\pi} \approx 0.63\ . \tag{4.24}$$

The controller can be described by summing over all possible noise angles α and all possible measurement outcomes that decide the feedback action

$$\mathcal{C}(\rho) = \int_{-\pi/2}^{+\pi/2}\frac{d\alpha}{\pi}\int_{-\infty}^{+\infty} dz\ p(z|\alpha)\,R_x(\Theta_g(z))\,M_z R_x(\alpha)\,\rho R_x^{\dagger}(\alpha)\,M_z^{\dagger}R_x^{\dagger}(\Theta_g(z))\ , \tag{4.25}$$

where $z \equiv m_0/J$ is the measurement output normalized to the Bloch sphere radius, and $\Theta_g(z)$ is the correction angle depending on the measurement result z. The conditional probability to measure z given that the state has been rotated by an angle α around the x-axis is obtained from Equation (4.9),

$$p(z|\alpha) = \frac{1}{\sqrt{2\pi\sigma_{\text{det}}^2}}\exp\left[-\frac{(z-\sin\alpha)^2}{2\sigma_{\text{det}}^2}\right]\ . \tag{4.26}$$

The probability to have $|z| > 1$ is non-zero due to the measurement uncertainty, but we cannot directly assign an angle to values outside of the Bloch sphere. A

feedback correction strategy which takes this problem into account is

$$\Theta_g(z) = \begin{cases} -g \arcsin z & \text{for} \quad |z| \leq 1 \\ -g\pi/2 & \text{for} \quad z > 1 \\ +g\pi/2 & \text{for} \quad z < 1 \end{cases} , \tag{4.27}$$

where g is the feedback gain. In the case of binary noise, there was no feedback gain because the feedback angle was preset. The feedback controller might have a maximum efficiency for different values of the feedback gain for different feedback strengths. Assuming that we are in the weak measurement regime with $M_z \sim 1$, the output state after feedback is

$$\rho_{\text{out}} = \frac{1}{\pi} \int_{-\pi/2}^{+\pi/2} d\alpha \int_{-\infty}^{+\infty} dz \; p(z|\alpha) \rho \left(\frac{\pi}{2} + \Theta_g(z) + \alpha \right) , \tag{4.28}$$

with an output coherence of (see Appendix E)

$$\eta_{\text{out}} = \left| \frac{1}{\pi} \int_{-\pi/2}^{+\pi/2} d\alpha \int_{-\infty}^{+\infty} dz \; p(z|\alpha) e^{i(\alpha + \Theta_g(z))} \right| . \tag{4.29}$$

If one assumes $N_{\text{at}} \to \infty$, we have ($\sigma \to 0$) even though $\kappa \ll 1$ and the conditional probability is $p(z|\alpha) = \delta(z - \sin\alpha)$. In this case, the output coherence becomes

$$\eta_{\text{out}}(g) \approx \frac{2}{\pi} \frac{\cos(\pi g/2)}{1-g} , \tag{4.30}$$

and a coherence close to unity is reached for an optimal gain of $g = 1$. In general, the output coherence is from Equation 4.29 a function of the measurement uncertainty and the coherence does usually not reach unity. In Figure 4.9(a), the output coherence is shown as a function of the measurement uncertainty for different gains. The feedback gain determines the maximal output coherence and in a region close to $\sigma = 1$ a roll-off occurs and the coherence decreases rapidly because of the random feedback controller action.

The optimal gain is not at unity for a measurement resolution larger than zero, as shown in Figure 4.9(b). This is due to the curvature of the Bloch sphere together with the measurement uncertainty, which causes that there is a higher probability to estimate a too large angle than a too small one. The optimal

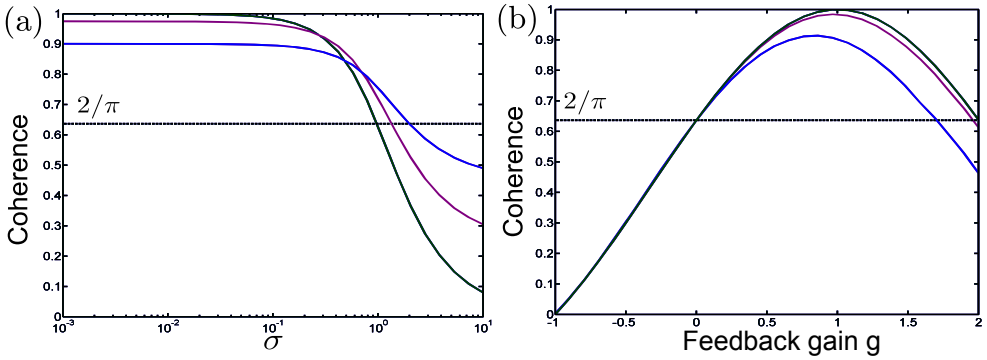

Figure 4.9.: (a) Coherence after feedback vs. the measurement resolution σ for $g = 1$ (dark green), $g = 3/4$ (violet) and $g = 1/2$ (blue). (b) Coherence after feedback vs. the feedback gain g for $\sigma = 0$ (dark green), $\sigma = 1/10$ (violet) and $\sigma = 1/3$ (blue). For both graphs, the dashed line is the coherence directly after the noise action.

feedback gain is therefore below unity. For example, if $\sigma = 1/3$, a maximum output coherence of about 0.85 is reached for $g \sim 0.75$.

A feedback strategy which is easier to implement experimentally consists in the application of a correction rotation with an angle proportional to the measurement output: $\Theta_g(z) = -gz$, since no correction for the curvature of the Bloch sphere has to be calculated in the feedback controller. Moreover, the saturation problem for $|z| > 1$ is avoided. A comparison of this correction strategy with the previous strategy is presented in Figure 4.10 for $\sigma = 0.14$. Interestingly, the second strategy leads to a better result: with the previous strategy a coherence of 0.975 is recovered for an optimum gain $g = 0.95$, whereas it reaches 0.979 for $g = 1.22$ with the second strategy.

The optimal gain for the proportional strategy is larger than unity since $|z| = |\sin\alpha| \leq |\alpha|$. Experimentally, the overall gain factors of the feedback system might not be known. A strategy to optimize the feedback gain consists in fixing a noise angle and maximizing the coherence of the output state by changing the feedback gain. The angle α_0 which should be chosen to optimize the gain satisfies $\alpha_0 - gz_0 = 0$ and since $z_0 = \sin\alpha_0$

$$g = \frac{\alpha_0}{\sin\alpha_0}. \tag{4.31}$$

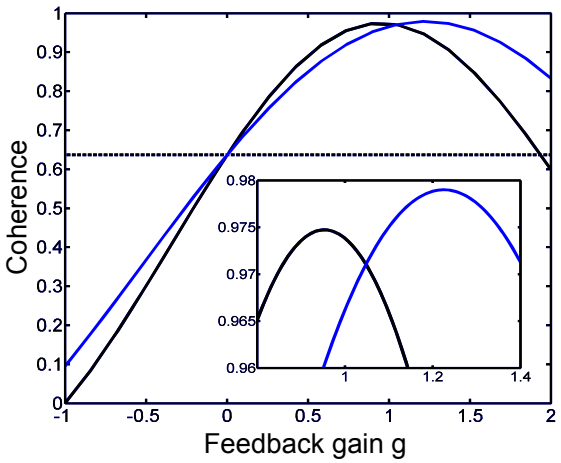

Figure 4.10.: Coherence after feedback versus the feedback gain for the two different correction strategies for a fixed detection resolution of $\sigma = 0.14$. The solid black line corresponds to the scheme with the correction for the curvature of the Bloch sphere while the solid blue line corresponds to the scheme where the correction angle is proportional to the measurement. The pointed line is the coherence directly after the noise. Inset: zoom at the optimum position.

For $g = 1.22$, we find $\alpha_0 \sim \pi/2.9$.

4.3.3.2. Experimental Results

For the analog noise, both the noise and the feedback have to be able to take continuous values in addition to the decision for the rotation directions. The random noise pulse is set with a stream of bits from the QRNG, which generates an integer number corresponding to a time in the FPGA card. The FPGA card then sends a TTL pulse to the LO to send a microwave pulse. Similarly, for the feedback, the MCU sends a TTL pulse to the LO and sets in addition the phase of the LO with the QPSK phase shifter for the rotation direction. The signals from the FPGA and MCU are combined with logical XORs before the LO.

We use 2.8×10^7 photons in the probe pulse, and the length of the microwave feedback pulses is proportional to J_z. We choose a fixed noise angle of $\pi/3$ close to the value proposed in the theoretical part and optimize the gain factor in the micro-controller in such a way that the length of the noise pulse and of the feedback pulse is on average equal.

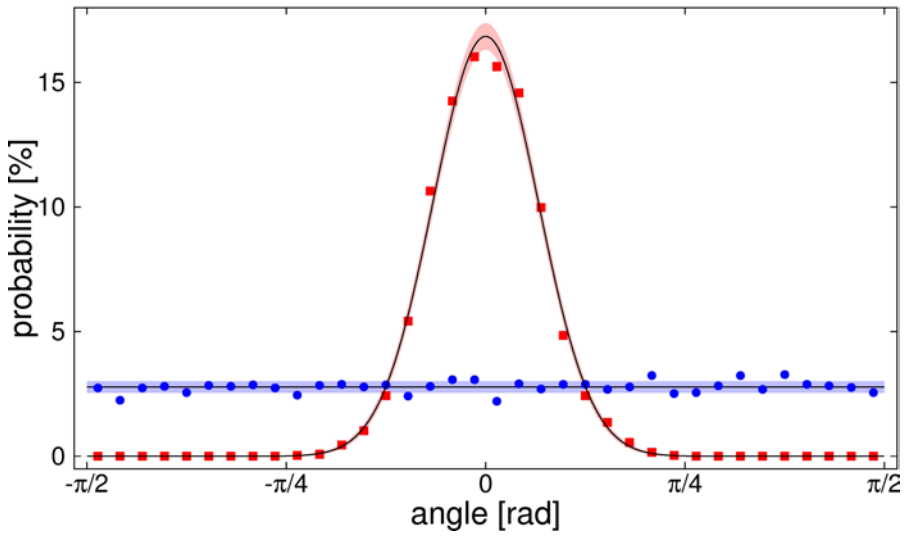

Figure 4.11.: Angular distribution for the collective spin right after application of the analog noise (blue circles) and after the succesive measurement and feedback (red squares).

We measure the coherence with and without feedback directly from the fringe contrast of a Ramsey interferometer from the average of 400 experimental repetitions. We find without feedback a coherence of 0.63(3), consistent with the expected value of $2/\pi \approx 0.637$, and with feedback 0.964(5). The feedback therefore greatly enhances the coherence of the state, also when we extend the noise model from Section 4.3.2 to arbitrary angles.

To see how the feedback controller corrects for the collective noise, we record the noise and controller rotations for 5000 repetitions, and plot the angular distribution with (θ_C) and without (θ_N) feedback, as presented in Figure 4.11. Without feedback, θ_N is uniformly distributed over $[-\pi/2, +\pi/2]$, whereas with feedback θ_C is well described by a Gaussian distribution centered at zero and of standard deviation 207(10) mrad. The angular spread is twice as big as expected for 2.8×10^7 probe photons (corresponding to a measurement uncertainty of 6.8%), and this was mainly due to digitization losses by bit shifts in the micro-controller. Considering only the spread of the spins without feedback, the coherence of the output state would be 0.979(2), but the probe induced decoherence reduces the coherence by another factor 0.979(1). The total residual coherence from the multiplication of

the two factors is therefore 0.958(2), which is consistent with the directly measured coherence of 0.964(5).

4.3.3.3. Applications

The feedback scheme demonstrated here with feedback on the atomic population difference could be directly used to reduce the read-out noise in an atomic interferometer. As an example, collective noise can increase the projection noise of highly squeezed input states which can then give an even worse interferometric performance than with a CSS. This problem was pointed out for the first time by D. Wineland in the appendix of [Wineland 98] and treated thoroughly in [André 04]. It corresponds to the observation made in Section 4.4 for $\kappa \gg 1$, that after unitary rotations the entangled state has a larger spread on the z-axis, opposed to the initial motivation for spin squeezing. Nevertheless, as only proposed recently in [Borregaard 13b], a lower uncertainty on z-axis can be recovered by turning the state back on the equator by a weak measurement and feedback. The scheme is depicted in Figure 4.12, which is a higher quality picture from [Borregaard 13b] and was kindly provided by J. Borregaard. With this scheme, the decoherence by the collective noise can be reversed, and near-Heisenberg scaling of the interferometer sensitivity can be reached.

The feedback scheme could be also used if the measurement uncertainty is above projection noise. The angular sensitivity from the J_z measurement then decreases as the spin vector gets closer to the poles of the Bloch sphere, and so the read-out noise increases. As before, it can be therefore beneficial to apply a weak measurement, rotate the state back on the equator of the Bloch sphere, and then apply the final measurement. One of the crucial points in the feedback method here, the saving of the correction angle for later reconstruction of the total angle, will also be used in our feedback control protocol to increase the interrogation time in an atomic clock in the next chapter.

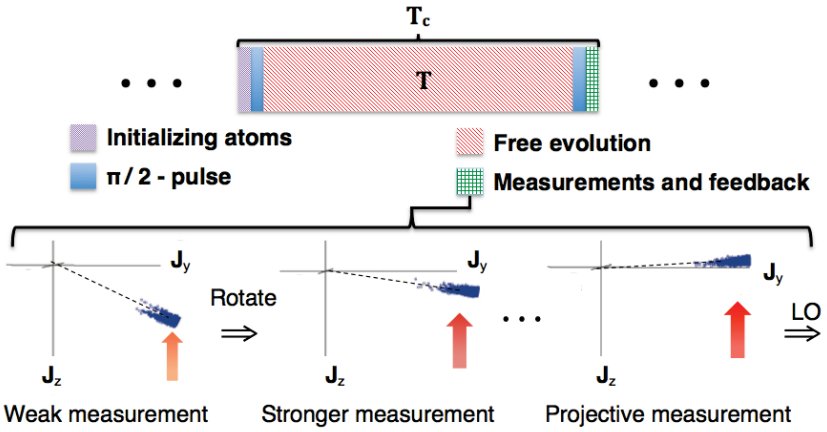

Figure 4.12.: Feedback scheme to reduce the read-out noise in an atomic interferometer, taken from [Borregaard 13b]. The position of the spin state is weakly read out and the state is turned back on the equator of the Bloch sphere. The total angle is then the finally measured angle minus the correction angle from the feedback controller.

5. Atomic Phase Lock

5.1. Introduction

In this chapter, we investigate how the tools introduced in this thesis can be used to improve atomic interferometers. As a model system, we consider an atomic clock. Atomic clocks are frequency locks, where the frequency of an electromagnetic wave (the local oscillator LO) is stabilized on the frequency of an atomic transition. Atomic frequency references offer the advantage of being universally comparable since the transition frequencies of the same atomic species are always and everywhere equal (as far as we know). Furthermore, atomic samples reach unprecedented high Q factors[1], since they can be trapped in vacuum and cooled to ultra-low temperatures. The stabilization of the LO on the atomic resonance is typically performed by either maximizing the contrast of Rabi oscillations or with the Ramsey interrogation scheme. The translation to the time domain is then obtained with a counter which counts the number of oscillation periods. We will focus here on the Ramsey interrogation scheme which has a higher sensitivity to phase drifts.

A main function of atomic clocks is the definition of time. The second is at the moment defined *via* the transition frequency of ^{133}Cs [Parker 10] and the redefinition of the second with optical lattice clocks is under discussion [Le Targat 13]. Recently, atomic clocks have reached a 10^{-18} precision [Hinkley 13, Bloom 13], which makes them susceptible to the gravitational red shift at the 1 cm level. These clocks have the potential to revolutionize geodesy applications with the mapping of gravitational fields at the highest precision. Furthermore, atomic clocks are at the forefront of fundamental physics tests, the comparison of clocks with different atomic species tests whether fundamental constants are changing over time [Marion 03]. So far, any improvement in the performance of atomic clocks has lead to unpredicted technological applications and is a backbone of

[1] The Q factor is defined as the ratio of the resonator frequency, for us ω_{LO}, to its linewidth $\Delta\omega_{\mathrm{LO}}$.

technological advance.

An atomic clock relies on the repeated comparison of the atomic frequency and the LO frequency. The longer the two frequencies can be compared, the more precise the frequency error can be estimated and feedback on the LO can be performed. In the Ramsey scheme, the atoms are in a superposition state during the interrogation, and the time for the comparison is limited by its coherence lifetime. In many atomic clocks, the frequency drift of the LO is the main decoherence source, and limits the interrogation time. In this chapter, we develop a feedback protocol to remove the decoherence caused by the LO and to increase the interrogation time in an atomic clock.

In Section 5.2, the standard Ramsey scheme for a conventional atomic clock is recalled. The detection noise and Dick limit are then introduced as the stability limits. In Section 5.3, we introduce the idea of the atomic phase lock. The proposal to lock the LO on the phase of the atomic ensemble came from two Japanese researchers, N. Shiga and M. Takeuchi, and is presented here. A drawback in their feedback scheme led to our formulation of a new protocol which is presented thereafter. We stabilize then the phase of the classical LO on the phase of a collective superposition state, and show the potential of the technique to improve atomic clocks (Section 5.4). Finally, we discuss then possible variation of our feedback scheme (Section 5.5) and the application of the atomic phase lock to inertial sensors (Section 5.7).

5.2. Atomic Clock Operated with the Standard Ramsey Protocol

5.2.1. Operation Principle

An atomic clock can be operated with a Ramsey interferometer. The pulse sequence is shown in Figure 5.1. At first, a superposition state is prepared with a $\pi/2$-pulse around the y-axis of the Bloch sphere. During a free interrogation time T, the relative phase between the atoms and the LO evolves because of the LO frequency noise. The phase is read out with another $\pi/2$-pulse, where the rotation is chosen to be around the x-axis to increase the sensitivity in case the detection is not at the atomic shot noise limit. From the phase drift during the interrogation time T, a frequency error is deduced and feedback on the frequency of the LO is

performed. The repetition of the basic feedback cycle ensures that the LO is kept frequency locked on the transition frequency of the atoms.

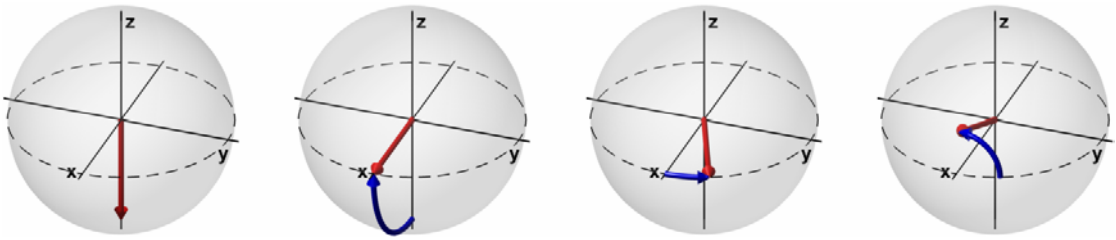

Figure 5.1.: Standard Ramsey protocol for an atomic clock. The last $\pi/2$-pulse is applied around the x-axis of the Bloch sphere such that the output state is closer to the equator of the Bloch sphere.

5.2.2. Stability Limits

The performance of atomic clocks is characterized in terms of their accuracy and stability. Accuracy can be understood as a systematic error between the LO and the bare atomic frequency. Stability refers to the fluctuations of the LO frequency in time. It defines how much time error an atomic clock would accumulate over a given period of time if it is referenced to itself. The most accurate and stable atomic clock, at the time of writing, is a strontium optical lattice clock with a value at the 10^{-18} level for both parameters [Bloom 13]. An atomic clock can never be more accurate than it is stable, and we will focus in this chapter on the stability of atomic clocks.

5.2.2.1. Allan deviation

The difficulty of determining the stability of an atomic clock lies typically in the problem that no absolute reference of higher stability is available. D. W. Allan therefore introduced the concept of the so called Allan deviation [Allan 66], where the frequency of the clock oscillator is compared to itself after a time delay.

The concept of the Allan deviation can be most easily understood by considering the fractional frequency error $y = \frac{\Delta f_{\mathrm{LO}}}{f_{\mathrm{LO}}}$ of a clock oscillator as shown in Figure 5.2. The Allan deviation is a function of an averaging time τ in which a frequency error is determined. It is calculated by taking the means y_n,y_{n+1} of y in two subsequent intervals n of length τ and subtracting the results to $\Delta y_n = y_{n+1} - y_n$. The

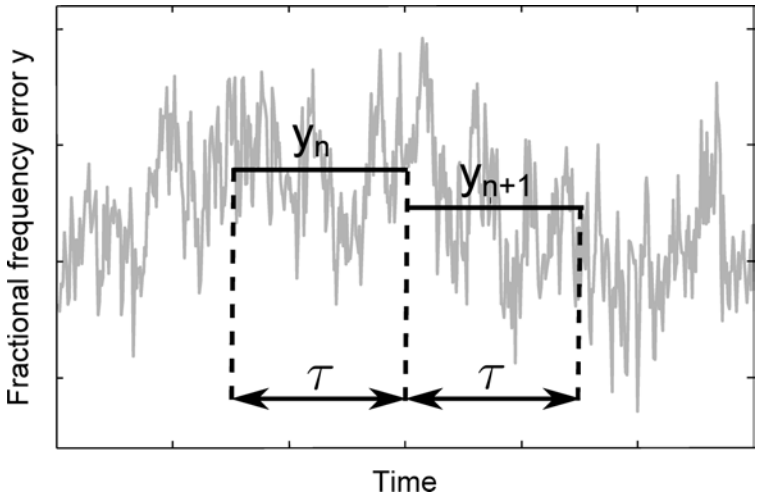

Figure 5.2.: Variables for the calculation of the Allan deviation. In gray the evolution of the fractional frequency error y over time is shown, which is characterized with the mean fractional frequency errors y_n and y_{n+1} for an integration time τ.

procedure is repeated for all neighboring intervals τ and the standard deviation for all Δy_n is taken

$$\sigma_y = \frac{1}{\sqrt{2}} \sqrt{\left\langle (y_{n+1} - y_n)^2 \right\rangle} \ . \tag{5.1}$$

The factor $\frac{1}{\sqrt{2}}$ arises from the comparison with an oscillator with white frequency noise where the subtraction of two random variables y_{n+1}, y_n would overestimate the variance by a factor two. If only the time error $x(t)$ is given then y_n is calculated by

$$y_n = \frac{x_{n+1} - x_n}{\tau} \ . \tag{5.2}$$

In other words, for a time sequence $x(t)$ the elements y_n are the slope of $x(t)$ in an interval τ.

5.2.2.2. Detection Noise Limit

In principle, any feedback control system can suppress the noise of a system until a white noise level is reached. In a conventional atomic clock, where the frequency of a LO is stabilized on an atomic frequency reference, this white noise limit is white frequency noise. There are no frequency correlations in time, and the feedback

controller cannot decrease the noise level further. Such a white frequency noise level appears in atomic clocks with the (Gaussian) uncertainty in the final state readout. The uncertainty can be dominated by the detection system itself, for example by photon shot noise ($\kappa = \frac{\sigma_J}{\sigma_{\text{det}}} \ll 1$), or by the atomic projection noise ($\kappa \gg 1$). It leads to the addition of a white noise level by the feedback on the frequency. The detection noise limit can be expressed as

$$\sigma_{y,\text{det}} = \frac{1}{\omega_{\text{LO}}} \frac{1}{\text{SNR}} \frac{1}{T} \sqrt{\frac{T_C}{\tau}} \,, \tag{5.3}$$

where SNR is the signal-to-noise ratio for each measurement of the relative phase, ω_{LO} the frequency of the LO and τ the averaging time over which the relative frequency error was determined. T denotes the interrogation time and $T_C = T + T_D$ is the time for one clock cycle, consisting of the interrogation phase and the dead time T_D. The dead time is the interval needed to prepare a new coherent spin state after its destruction by the optical readout.

The first terms in Equation (5.3) can be understood in terms of the frequency noise added by the controller in each clock cycle, which is given by the product of the frequency equivalent of the interrogation time $f_T = \frac{1}{T}$ and the measurement uncertainty of the phase $\Delta\phi = \frac{1}{\text{SNR}}$. The introduced noise is then averaged down with the square root of the number of clock cycles $1/\sqrt{N_C} = \sqrt{T_C/\tau}$. The detection noise limit is the dominating noise limit in ion clocks [Rosenband 08] and can be as well reached in atomic fountain clocks [Santarelli 99] and in optical lattice clocks [Takamoto 11].

5.2.3. Dick Limit

The periodic interrogation of the atomic reference can lead to a degradation of the clock stability by frequency drifts which were undetected (for example during a dead time) or only detected with a low sensitivity (for example during Rabi pulses). High frequency components in the free running LO with spectral density S_y^{LO} are then sampled down over the action of the feedback controller as in an aliasing effect. This effect was first theoretically described by G. J. Dick in 1987 [Dick 87] and summarized in the expression

$$\sigma_{y,\text{Dick}} = \sqrt{\frac{1}{\tau} \sum_{n=1}^{\infty} \frac{g_{n,1}^2 + g_{n,2}^2}{g_0^2} S_y^{LO}\left(n f_c\right)} \,, \tag{5.4}$$

where $f_c = 1/T_c$ and the coefficients g_0,$g_{n,1}$ and $g_{n,2}$ are the Fourier components of the sensitivity function $g(t)$, with

$$g(t) = 2 \lim_{\delta\phi \to 0} \frac{\delta P(\delta\phi, t)}{\delta\phi} \ , \tag{5.5}$$

$$g_0 = \frac{2}{T_C} \int_0^{T_C} g(t) dt \ , \tag{5.6}$$

$$g_{n,1} = \frac{2}{T_C} \int_0^{T_C} g(t) \cos\left(2\pi n t f_c\right) dt \ , \tag{5.7}$$

$$g_{n,2} = \frac{2}{T_C} \int_0^{T_C} g(t) \sin\left(2\pi n t f_c\right) dt \ . \tag{5.8}$$

The sensitivity function $g(t)$ describes the sensitivity of the interferometer to an infinitesimal phase change of the LO. It is maximal during the interrogation time T and zero during the dead time. The sensitivity function under Ramsey interrogation with two $\pi/2$-pulses of time $\tau_{\pi/2}$ takes the form

$$g(t) = \begin{cases} \sin\left(\frac{\pi}{2} \frac{t}{\tau_{\pi/2}}\right) & 0 \leq t \leq \tau_{\pi/2} \\ 1 & \tau_{\pi/2} \leq t \leq T + \tau_{\pi/2} \\ \sin\left(\frac{\pi}{2} \frac{(t-T)}{\tau_{\pi/2}}\right) & T + \tau_{\pi/2} \leq t \leq T + 2\tau_{\pi/2} \\ 0 & T + 2\tau_{\pi/2} \leq t \leq T_C \end{cases} . \tag{5.9}$$

It is illustrated in Figure 5.3. In the case that the LO only has white frequency noise and $\tau_{\pi/2} \ll T_C$, there is an analytical solution of the Dick limit [Santarelli 96, Quessada 03],

$$\sigma^2_{y,\mathrm{Dick}} = \frac{h_0}{\tau} \left(\frac{T_C}{T} - 1 \right) = \frac{h_0}{\tau} \frac{T_D}{T} \ , \tag{5.10}$$

where h_0 is the constant (fractional) spectral density of the white noise. From Equation (5.10), one sees that the Dick limit is decreasing with a longer interrogation time. The same holds for a more realistic noise model, $1/f$ frequency noise, as it is treated in Appendix F.

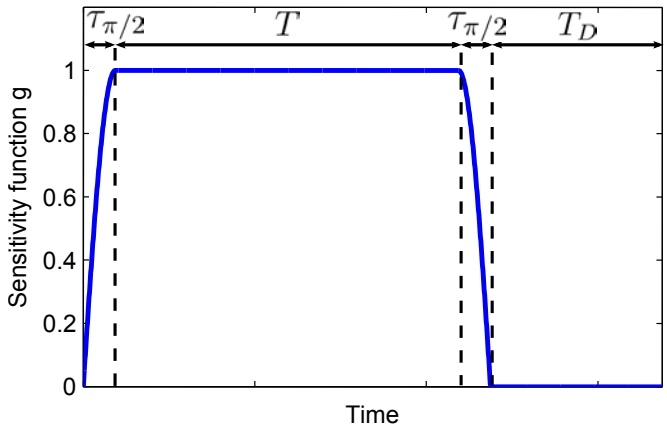

Figure 5.3.: Sensitivity function for a Ramsey interferometer.

5.3. Concept of Atomic Phase Lock

5.3.1. The Proposal by N. Shiga and M. Takeuchi

The proposal to lock a LO on the phase of a collective atomic quantum state was published in 2012 by N. Shiga and M. Takeuchi [Shiga 12]. In their paper, they noted that although some of the most stable locks are phase locks, that an atomic clock is a frequency lock. The question therefore arises if an atomic clock could be improved if it would be operated as a phase lock instead.

In a phase lock, the phase of an oscillator is locked on the one of another oscillator. The crucial point here is the stabilization on a phase reference. In an atomic clock, one reads out the phase difference of the LO and a reference, which is the oscillating phase of a superposition state. Nevertheless, after the interrogation the atomic phase reference is destroyed in the read-out (usually a fluorescence measurement). The only common property of the atomic reference between experimental runs is therefore the atomic transition frequency. This is the reason why an atomic clock is a frequency lock, and not a phase lock.

To operate an atomic clock as a phase lock, it would be necessary to read out the phase between the LO and the atoms without destroying the atomic phase. Weak measurements as described in this manuscript provide just the right tool to do so, where the state after the measurement is practically the same as the one before. The proposed scheme of N. Shiga and M. Takeuchi to use weak measurements in

an atomic clock is shown in Figure 5.4.

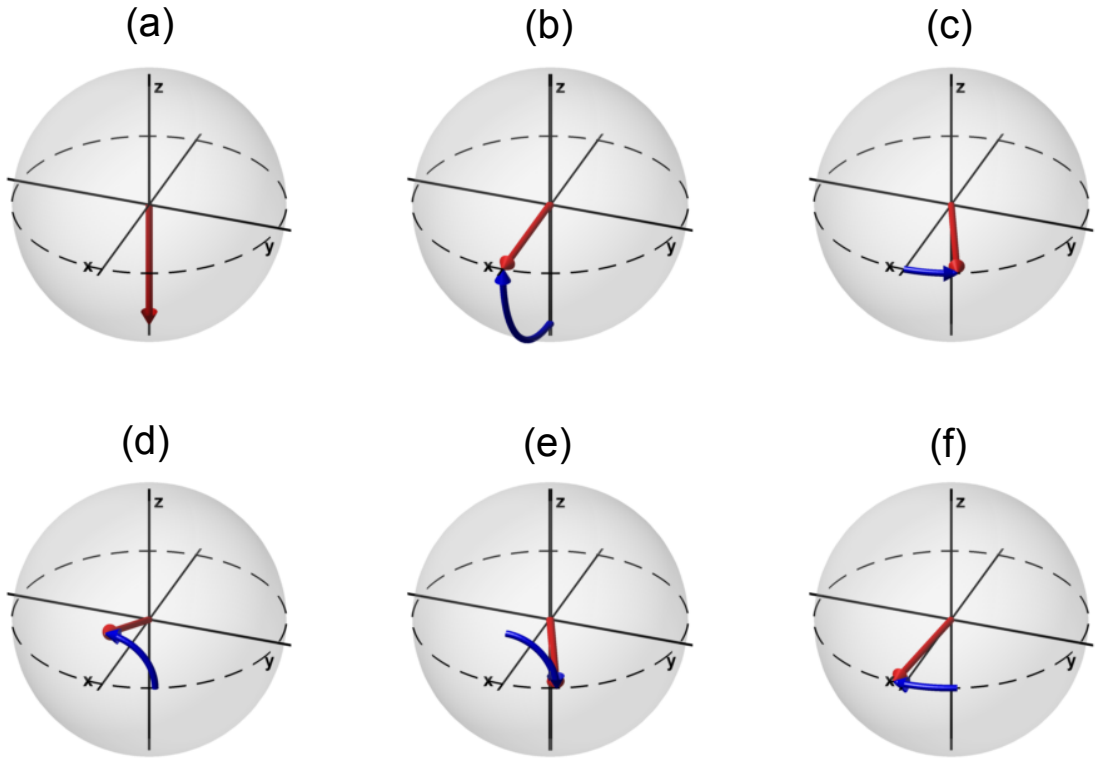

Figure 5.4.: Atomic phase lock scheme: (a) Initial state. (b) Preparation of superposition state. (c) Free evolution. (d) Mapping on z-axis and read out with a weak measurement. (e) Reinsertion of atomic state into interferometer. (f) Feedback to reduce phase difference between atoms and LO.

The first four steps (a) - (d) are the same as in the standard Ramsey protocol, with the difference that the state is read out with a weak measurement. After the phase read out, the state is reinserted into the interferometer (e). The information from the weak measurement is then used to perform feedback on the frequency of the LO (f) such that after the next free evolution, the phase error is reduced. Steps (c) to (f) are repeated. The feedback law is [Shiga 12]

$$\omega_{\mathrm{LO}}^{(N)} = \omega_{\mathrm{LO}}^{(N-1)} - g_f \frac{\phi^{(N)} - \phi^{(N-1)}}{T_{\mathrm{FE}}}, \tag{5.11}$$

where $\omega_{\mathrm{LO}}^{(N)}$ is the angular frequency of the LO after feedback, and T_{FE} is the free evolution time. The phases $\phi^{(N)}$ include the uncertainty of the weak measurement

and $\phi^{(0)} = 0$ is set by the initialization of the state. The gain factor g_f is typically chosen to be one or slightly less.

The essential point of the atomic phase lock is that errors from the uncertainty of the weak measurement propagate to the next cycle where they can be corrected again. This can be reflected in the Allan deviation, which according to Equation (5.1), can be written as

$$\sigma_y(\tau) = \frac{\delta_\phi(\tau)}{\omega_{\mathrm{LO}}\,\tau}\,, \tag{5.12}$$

with

$$\delta_\phi(\tau) = \sqrt{\left\langle [\phi(t+\tau) - \phi(\tau)]^2 \right\rangle}\,. \tag{5.13}$$

It was assumed here that the clock is not limited by the Dick effect but by the detection noise. Since errors from the uncertainty of the weak measurements always propagate to the next measurements, the only overall phase error $\delta_\phi(\tau)$ comes from the SNR_w of a single weak measurement,

$$\delta_\phi(\tau) = \frac{1}{\mathrm{SNR}_w}. \tag{5.14}$$

The scaling of the Allan deviation is therefore

$$\sigma_y(\tau) = \frac{1}{\mathrm{SNR}_w\,\omega_{\mathrm{LO}}\,\tau}\,. \tag{5.15}$$

From a first view, because of the $\frac{1}{\tau}$-scaling of the Allan deviation, the phase lock scheme appears to be strongly superior than a conventional atomic clock for large τ. However, the CSS can only be maintained for a restricted number of repetitions, for practical reasons such as the destructivity or projectivity[2] from the weak measurements, dephasing of the trapped atoms, vacuum lifetime or even the lifetime of the excited states.

When the coherence of the probed quantum state is lost, a new state has to be prepared for which the phase is uncorrelated with the one of the previous state. For $\tau > T_C$, the system is then equivalent again to a conventional atomic clock. The phase lock operation corresponds then to a normal interrogation with a time

[2] Many weak measurements on the same state correspond to a strong projective measurement. In our case, this can be understood from a multiplication of all Gaussian measurement functions.

$T = N\,T_{\mathrm{FE}}$ and the clock instability for $\tau > T_C$ is

$$\sigma_{y,\mathrm{det}} = \frac{1}{\omega_{\mathrm{LO}}} \frac{1}{\mathrm{SNR}_w} \frac{1}{NT_{\mathrm{FE}}} \sqrt{\frac{T_D + NT_{\mathrm{FE}}}{\tau}} \,. \tag{5.16}$$

The effect of the phase lock is therefore to increase the interrogation time from $T = T_{\mathrm{FE}}$ to $T = N\,T_{\mathrm{FE}}$.

An obvious question to raise is why one could not simply increase directly the interrogation time instead of applying the phase lock. A problem often encountered in trapped atomic clocks is that the LO itself limits the interrogation time as depicted in Figure 5.5.

In a Ramsey interferometer, the phase drift during an interrogation time T can only be determined without any ambiguity if the phase difference stays within the $\left[-\frac{\pi}{2}, \frac{\pi}{2}\right]$ interval. If this condition is not given, any read-out result could correspond to a minimum of two different phase drifts and the feedback controller would introduce errors. In practice, one therefore chooses a short enough interrogation time such that the probability that the phase drift leaves the inversion region is negligible. If one chooses the standard deviation of the phase drift to be $\sigma_\phi \leq \frac{\pi}{12}$, then the probability to leave the inversion region is a 6-sigma event. Because of this constraint, we can set $T = T_{\mathrm{FE}}$ in the comparison of the phase lock and a conventional atomic clock. The atomic phase lock changes then the instability of

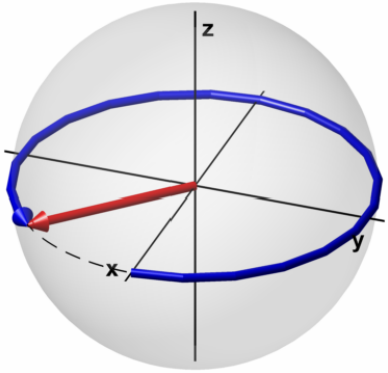

Figure 5.5.: Inversion problem on the Bloch sphere. When the phase drift leaves the $\left[-\frac{\pi}{2}, \frac{\pi}{2}\right]$ interval it cannot be unambiguously determined anymore. The inversion problem is the main motivation for the atomic phase lock from a metrological perspective.

an atomic clock by a factor

$$\xi_{\mathrm{ST}} = \frac{\mathrm{SNR}_0}{\mathrm{SNR}_w}\frac{1}{N}\sqrt{\frac{T_D + NT}{T_D + T}}\ , \tag{5.17}$$

where the subscript "ST" stands for Shiga-Takeuchi. From Equation (5.17), one sees that there is a metrological gain due to a longer interrogation time, but there is also a loss because instead of the SNR_0 of the strong measurement the SNR_w of the weak measurement is used. The low SNR from the weak measurements therefore constitutes a significant drawback in the original proposal of N. Shiga and M. Takeuchi. If $\mathrm{SNR}_0 \gg \mathrm{SNR}_{\mathrm{w}}$, an atomic clock operated with atomic phase lock might perform with this protocol even worse than an atomic clock operated with the standard Ramsey scheme.

5.3.2. Our Feedback Protocol

We developed a different protocol for the atomic phase lock with the intention to prolong the effective interrogation time while suffering from any disadvantage of the lower $\mathrm{SNR}_{\mathrm{w}}$ of the weak measurement. The state rotations are the same as in Figure 5.4. The steps in the feedback controller are:

1. **Feedback on the LO phase.** During the interrogation time, feedback on the phase of the LO is applied. The control law is

$$\phi_{\mathrm{LO}}^{(N)} = \phi_{\mathrm{LO}}^{(N-1)} + \phi_{\mathrm{FB}}^{(N)} \tag{5.18}$$

$$= \phi_{\mathrm{LO}}^{(N-1)} + g_\phi \phi^{(N)}\ , \tag{5.19}$$

   where we recall that $\phi^{(N)}$ is the estimated phase difference between the LO and the atoms at a cycle N and $\phi_{\mathrm{LO}}^{(N)}$ is the phase of the LO only. The values of $\phi_{\mathrm{FB}}^{(N)} = g_\phi \phi^{(N)}$ are saved in the feedback controller and typically a gain $g_\phi = -1$ is chosen.

2. **Precise final readout.** At a number of phase lock cycles N_{max}, no weak measurement but a strong (possibly destructive) measurement of the phase is performed. The phase $\phi^{(N_{\mathrm{max}})}$ of the atomic state is then determined with the highest possible precision.

3. **Feedback on the LO frequency.** The result of the final precise measurement and of the saved phase shifts on the LO are taken to reconstruct the

full phase drift between the LO and the atoms in the interrogation time T. One then performs feedback on the frequency as in a conventional atomic clock,

$$\omega_{\mathrm{LO}}^{(N_C)} = \omega_{\mathrm{LO}}^{(N_C-1)} + \omega_{\mathrm{FB}}^{(N_C)} \tag{5.20}$$

$$= \omega_{\mathrm{LO}}^{(N_C-1)} + g_f \frac{\phi_{\mathrm{tot}}^{(N_C)}}{T}\,, \tag{5.21}$$

where

$$\phi_{\mathrm{tot}}^{(N_C)} = \phi^{(N_{\max})} - \sum_N \phi_{\mathrm{FB}}^{(N)} \tag{5.22}$$

$$= \phi^{(N_{\max})} - \sum_N g_\phi \phi^{(N)}\,. \tag{5.23}$$

In addition, all phase shifts by the feedback controller are reset to zero at the end, so that after one cycle there is no effective feedback on the LO phase

$$\phi_{\mathrm{LO}}^{(N_C)} = \phi_{\mathrm{LO}}^{(0)}\,. \tag{5.24}$$

A schematic representation of the feedback control scheme is given in Figure 5.6. The important feature of the feedback controller is that the feedback actions on the LO oscillator phase during the interrogation time are saved. They are then

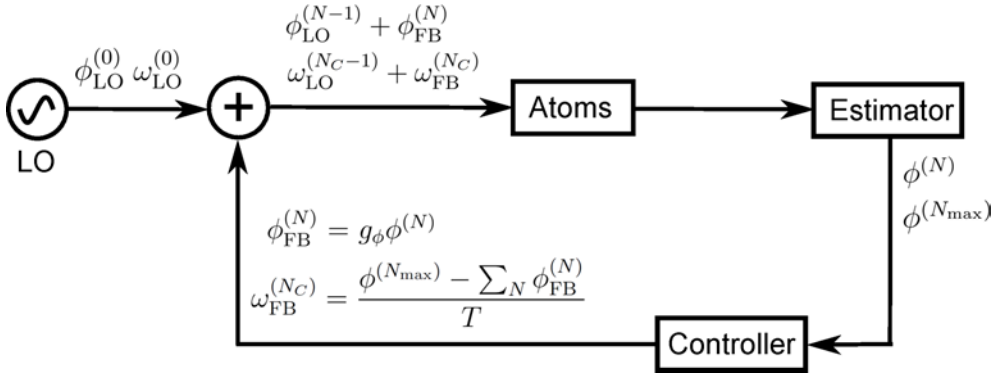

Figure 5.6.: Schematic representation of the feedback protocol. The feedback controller consists of two stages, one for the phase lock (N repetitions) and one for the frequency lock (N_C repetitions). The reset of the feedback on the phase of the LO after the final measurement is not indicated.

used with the output of the precise measurement to determine the total phase drift. There is no drawback from the uncertainty of the weak measurements, since any feedback errors are detected with the precise final measurement at the end.

The presented feedback control scheme therefore resolves the inversion problem while keeping a high SNR of the final precise measurement. It is therefore equivalent to a normal atomic clock where the interrogation time is prolonged. The problem can be also seen from a perspective that the feedback controller removes the decoherence from the LO and therefore allows a longer interrogation time. However, since the phase drift is the signal itself, it has to be saved in the feedback controller. The metrological gain from the feedback controller is

$$\xi_{\mathrm{PL}} = \frac{\mathrm{SNR}_0}{\mathrm{SNR}_{\mathrm{PL}}} \frac{1}{N} \sqrt{\frac{T_D + NT}{T_D + T}}, \tag{5.25}$$

where $\mathrm{SNR}_{\mathrm{PL}}$ is the SNR from the final precise measurement at the end of the phase lock. For the potential metrological gain of the feedback controller, consider the example of the real time observation of Rabi oscillations in Section 3.5.2. We have seen there that as result of the decoherence induced by the probe, the contrast is still 45% after 200 measurements. If we assume no other decoherence sources and a ratio of initial dead time to interrogation time $\frac{T_D}{T} = 1$, we have then from Equation (5.25) a gain of $\xi_{\mathrm{PL}}^{-1} \approx 13.4$. In practice, a limitation to reach such gains will be the vacuum lifetime of the trapped atoms. If we assume an initial interrogation time of $T = 0.5$ s limited by the inversion problem, the total interrogation time would be 100 s. Such vacuum lifetimes are typically not reached in current setups. Nevertheless, with improved trap lifetimes, a gain of about one magnitude with phase lock appears to be well within reach.

Our feedback scheme can be combined with squeezed input states, which improve the $\mathrm{SNR}_{\mathrm{PL}}$ of the final measurement. This is an additional advantage over the Shiga-Takeuchi scheme, in which squeezed input states would bring no metrological gain. An atomic clock equipped with a nondestructive detection system could therefore win twice, on one hand by improving the SNR, and on the other hand by a longer interrogation time. We remark that the technical requirements for the nondestructive measurement system for the atomic phase lock are much lower than those for spin squeezing, which could facilitate its implementation in existing systems.

The above discussion about metrological gains only concerns the detection noise limit but not the Dick limit. Intuitively, one could argue that by an improved ratio of interrogation time to dead time, less information on the phase drift of the LO is lost, so that the Dick limit is reduced. However, the validity of Equation (5.4) has so far only been proved for phase drifts $\sigma_\phi < 10°$. This condition is not fulfilled in the atomic phase lock, where the total phase drift could even turn several times around the equator of the Bloch sphere. The dependence of the Dick effect as a function of the prolongation of the effective interrogation time therefore needs further study.

5.4. Experimental Results

5.4.1. Real Time Observation of the Phase in a Ramsey Interferometer

We work as before with the $|0\rangle \equiv |F = 1, m_F = 0\rangle$ and $|1\rangle \equiv |F = 2, m_F = 0\rangle$ clock states in ^{87}Rb. The LO is derived from a frequency chain at 7 GHz mixed with a RF generator at 165 MHz, which is phase controlled with a QPSK phase shifter for the state rotations. An additional digital phase shifter, which can introduce a 2π phase shift using a 6 bit control, is added to the setup for the feedback on the LO phase. The length of a $\pi/2$-pulse is $\tau_{\pi/2} = 47$ μs.

We use the probe configuration introduced in Section 3.4.3, with the carrier locked at 3.377 GHz from the $F = 1 \rightarrow F' = 2$ transition and frequency sidebands at a modulation frequency of 3.853 GHz. The modulation depth is 14.8% and the probe power 480 μW. The pulse length is 60 ns and the beam is matched to the 50 μm size of the atomic cloud. Only after completion of taking the experimental data, we realized that the nondestructive measurements suffered from a loss in SNR due to a 30 ns rise time in the response of the PD, which we cannot explain at the moment. However, since our feedback protocol is largely independent of the SNR_w of the weak measurements, this only minimally affects the results below.

At the beginning, we do not apply feedback on the LO but only perform steps (a) - (e) in Figure 5.4, where the steps (c)-(e) are repeated. We apply a frequency offset of 100 Hz on the LO such that the phase between the LO and the atoms drifts at a constant rate. The phase difference is read out after an interrogation time of $T = 1$ ms by applying a $\pi/2$-pulse around the x-axis of the Bloch sphere. To obtain a J_y measurement, the results of the weak

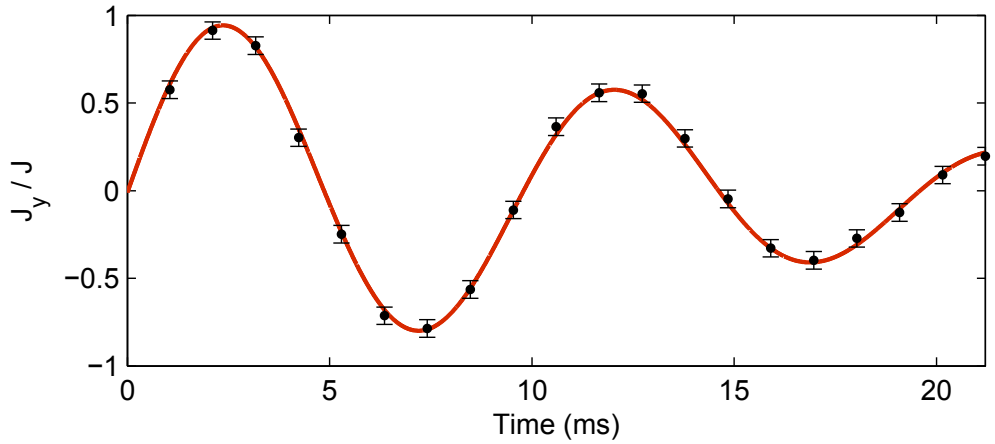

Figure 5.7.: Real time observation of the relative phase between the atoms and the LO for a frequency offset on the LO of 100 Hz.

measurements are normalized to the full scale signal when all atoms are repumped to $F = 2$. The measured points for a single experimental run are shown in black circles in Figure 5.7, and the error bars are from the SNR of the weak measurement.

At full coherence, the SNR of the weak measurements is 20. The state rotates several times around the z-axis of the Bloch sphere resulting in a sinusoidal J_y signal, which is fitted with a red solid line. The decay of the atomic state is due to dephasing in the dipole trap and the destructivity of each measurement pulse, which destroys the atomic state by 2% each time. The signal is less favorable than the Rabi oscillations from Section 3.5.2 because of the state decay induced by the dipole trap.

The dephasing from the dipole trap is a far stronger decoherence source than the bare frequency noise of the LO in our experiment. The initial condition for a metrological gain from the atomic phase lock is therefore not given, because the interrogation time in an atomic clock would be not limited by the LO. Dephasing is not a limitation in optical lattice clocks, because of the choice of a "magic wavelength" of the dipole trap, where there is no differential light shift between the clock states [Takamoto 05]. For rubidium atoms, the effect of trap inhomogeneities can be also removed by the so called "spin-self rephasing" effect [Deutsch 10]. In those systems, the atomic phase lock is a realistic solution to overcome the LO noise. The purpose of our experimental work is to demonstrate

basic operation principles, and to indicate directions which could be taken in state-of-the-art atomic clocks. In our own experiment, we might later apply the atomic phase lock to inertial sensors (see Section 5.7.1), where the atoms are not trapped and dephasing is not a limitation.

5.4.2. Stabilization of LO Phase on Atomic Phase

From the measurement of J_y and the known decay factors, the phase difference can be deduced by simply taking the arcsin. If we have more information on the noise, for example that it is only a frequency offset, the phase can also be reconstructed even if it leaves the $\left[-\frac{\pi}{2}, \frac{\pi}{2}\right]$ region. This was used in the red line in Figure 5.8 to reconstruct the phase drift from the data in Figure 5.7. The black circles are the deduced phase values and the error bars are obtained from the error propagation of the uncertainty from the weak measurements.

In general, such *a priori* information is not available, and the phase drift cannot

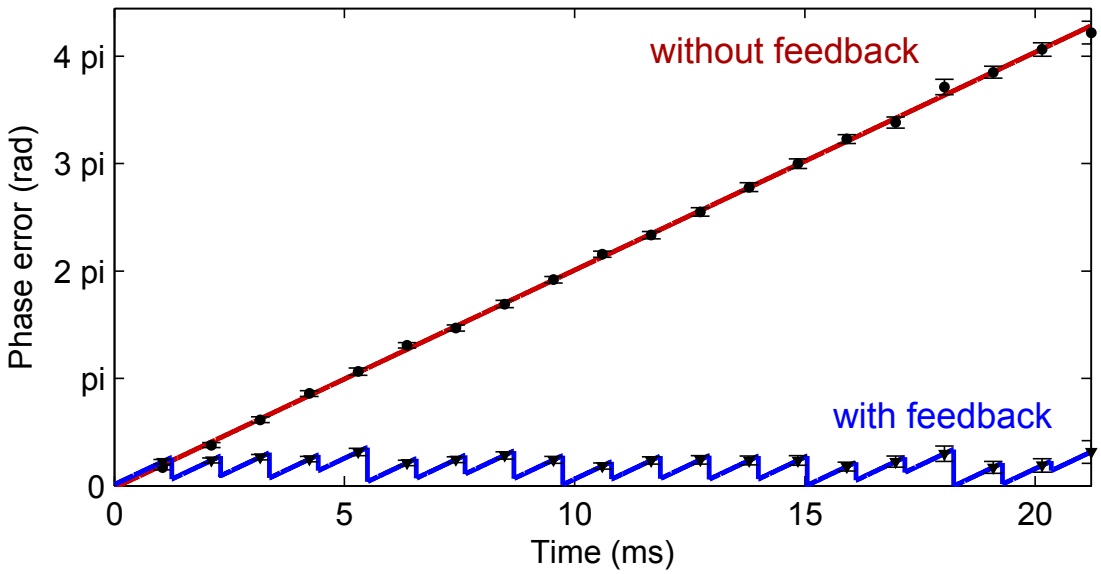

Figure 5.8.: Phase drift between LO for frequency offset of Δf=100 Hz without (red) and with (blue) feedback. Without feedback, the phase drift leaves the inversion region in which without additional information the phase cannot be unambiguously determined.

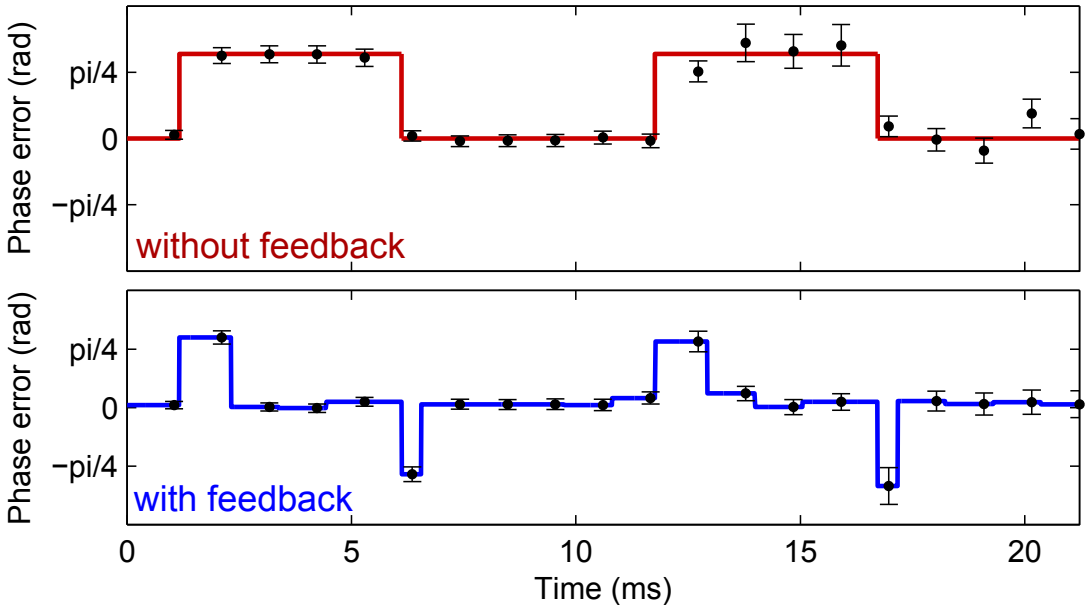

Figure 5.9.: Phase jumps without (red) and with (blue) feedback

be reconstructed. This is the reason why the phase lock has to keep the phase drift in the inversion region. We insert therefore the integrated signal from the weak nondestructive measurement into the feedback controller which changes the phase of the LO via a phase shifter. For the normalization of the nondestructive signal with respect to the atom number, always the background and the full scale value are taken from the previous experimental run. The feedback is proportional to J_y, similar to that for the analog noise in the previous chapter (Section 4.3.3). The gain value this time is set such that at 22.5° the gain is equal to one.

The results with the same noise but with feedback are shown in the blue line in Figure 5.8. After each interrogation, feedback is performed after the state is rotated back into the atomic interferometer. The total delay for the feedback is approximately 150 μs depending on the calculation time of the microcontroller. With feedback, the phase drift does not exceed the $\pi/2$ limit. The saw-tooth form is drawn considering the delay time for the feedback and taking the slope of the phase drift without feedback. Figure 5.8 shows that it is possible to lock the phase of classical oscillator on the phase of a collective quantum superposition state. It is the first demonstration that a classical object can be stabilized on a

quantum system in a superposition state.

In Figure 5.9, we studied another noise action, where phase jumps on the LO were applied with an additional phase shifter. Starting at 1.2 ms, the phase jumps back and forth 1 rad every 5 ms. Figure 5.9 (top) shows the phase without feedback and Figure 5.9 (bottom) with feedback. The experimental points (dark circles) are reconstructed from the result of the weak measurements. The solid lines without (red) and with (blue) feedback are drawn from the known timings for the applied noise and the feedback on the phase. For the blue line, the value for the phases is taken from the results of the weak measurements.

When the feedback controller is activated, the phase difference is set close to zero after the feedback delay. The correction is not perfect because of the minimal step size of 5.625° of the phase shifter, the uncertainty in the weak measurements and the feedback delay. In addition to the phase reconstruction process itself, this causes the deviation of the phase from zero after the feedback. The phase excursions are corrected after varying delays, because the feedback controller only acts at fixed times. The delays range here from 0.4 ms to 1 ms.

5.4.3. Full Feedback Scheme

As mentioned above, the atomic phase lock would not lead to metrological gain for an atomic clock in our setup, because of the dephasing in the optical

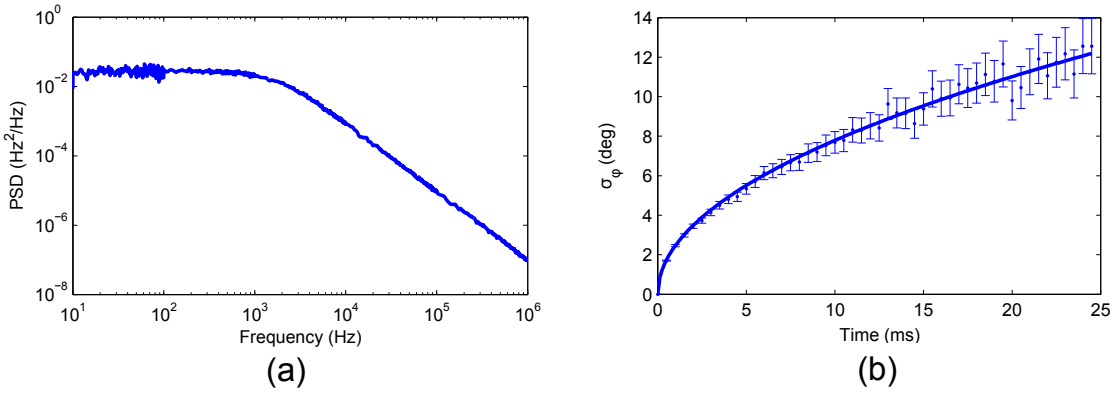

Figure 5.10.: LO overwhelmed with white frequency noise. (a) Power-spectral density (PSD) of LO noise. (b) Phase drift in an atomic clock with interrogation time T from LO noise.

dipole trap. Nevertheless, we can operate an atomic clock with the atomic phase lock in order to demonstrate its operation principle. For a proof-of-principle demonstration, we overwhelm the frequency of our LO with white frequency noise with a power spectral density of $h = 0.0262$ Hz^2/Hz low pass filtered at 1.6 kHz with 20 dB/decade (Figure 5.10(a)). The normalized power spectral density is $S_y^{LO} = h_0 = \frac{h}{f_{\mathrm{LO}}^2} = 5.6 \times 10^{-22}$ Hz^{-1}. The filter at 1.6 kHz was applied for a simpler analysis of the noise, it is still white and uncorrelated for our purposes because the relevant time scale is the cycle time of the experiment of 2 s.

The white noise was generated with a signal generator. It was added to the LO using the modulation input of the RF generator of the LO with a conversion factor of 200 Hz/V$_{\mathrm{rms}}$. In Figure 5.10(b), the expected phase drift from the LO noise versus the interrogation time is shown. It was obtained from a 2 s sample of LO noise, cut in equally spaced pieces to take the standard deviation. The standard deviation was then multiplied by $\sqrt{2}$ because events for white noise are uncorrelated, and so the total phase drift will be increased by the feedback controller. The phase drift in Figure 5.10(b) grows with the square root of time as expected for white noise. As an example, at 4 ms the average phase drift is 5°.

At the beginning, we run a conventional atomic clock with $T = 1$ ms and $T_D = 1.9$ s as shown in Figure 5.11 in red. To simplify the experimental implementation, we use for the final measurement the same pulse as for the weak measurement with 60 ns duration and a probe power of 480 μW. The correction signal is added to the noise applied on the LO an then connected to the modulation input of the LO. The two-sample Allan deviation was calculated from this combined signal. The clock instability reaches a $\tau^{-1/2}$-scaling after a few clock cycles consistent with the level expected from Equation (5.3) for the detection noise limit of an atomic clock. The error bars are given by the limited number of experimental points (we used 1000 clock cycles).

The instability of the clock[3] ($1.6 \times 10^{-9}\ \tau^{-1/2}$) is several magnitudes higher than with state-of-the art atomic clocks, largely because of the small interrogation time and the low SNR of the read-out. After the operation of a conventional atomic clock, we activate the atomic phase lock for $N = 10$ cycles (Figure 5.11, blue). The clock instability has an approximate $\tau^{-1/2}$-scaling as

[3] We follow the convention that the unit $\sqrt{s}$ is omitted for describing the scaling of the Allan deviation

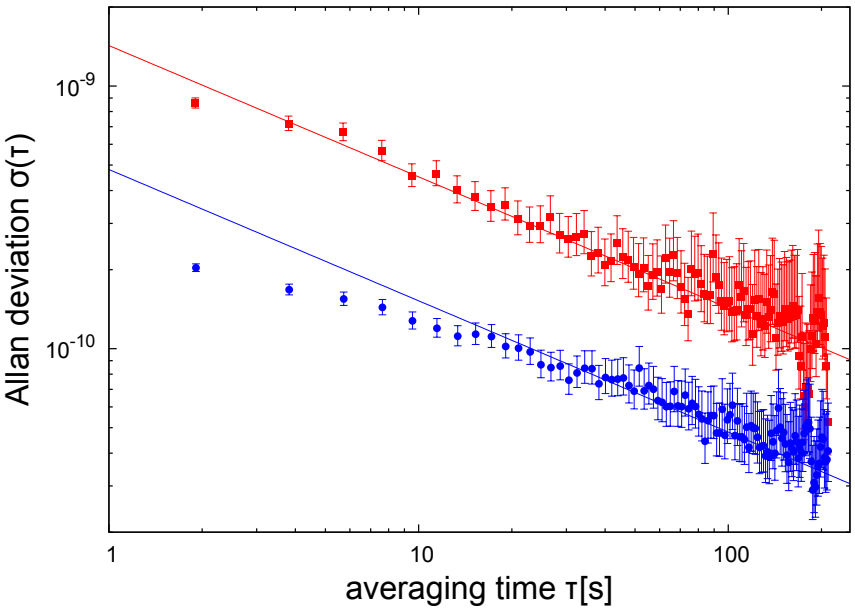

Figure 5.11.: Allan deviation without (red squares) and with (blue circles) atomic phase lock for N=10.

a clock operated with a normal Ramsey interferometer but at a lower level. Overall, the instability is decreased by a value of 4.7 dB. Nevertheless, without any additional decoherence sources, the clock instability should decrease from Equation (5.3) for $N = 10$ by approximately one order of magnitude since $T \ll T_c$.

To test quantitatively the behavior of the clock instability, we scan the Allan deviation for different repetition numbers N of the phase lock cycle. In Figure 5.12, the experimental results are shown in black circles. The points are obtained from a fit of the Allan deviation data with $\sigma_y = A\tau^{-1/2}$ for each run of the clock with a different number of phase lock cycles. The error bars are dominated by the fluctuations of the atom number over the time of the data acquisition. They are underestimated since we still had residual correlations in the LO signal but imposed $\sigma_y = A\,\tau^{-1/2}$ for the fit. The red line is an analytical prediction for the expected clock instability. It is calculated from the contribution of the Dick effect and the detection noise limit *via*

$$\sigma_y = \sqrt{\sigma_{y,\mathrm{Dick}}^2 + \sigma_{y,\mathrm{det}}^2}\,. \tag{5.26}$$

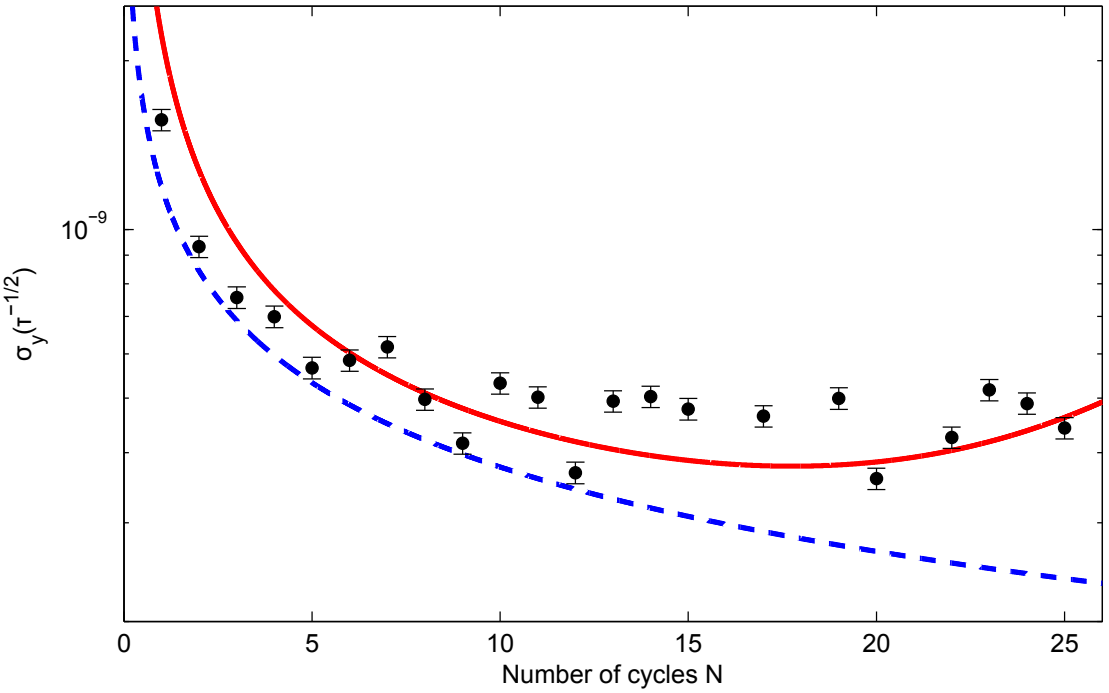

Figure 5.12.: Scaling of clock instability with number of phase lock cycles. The experimental results are shown in black circles. The dashed blue line is the Dick limit calculated from the known LO frequency noise, and the red line is the predicted instability from the known experimental parameters.

The contribution of the Dick effect is calculated using Equation (5.10) and shown as a blue dashed line. The contribution from detection noise then accounts for the remaining difference from the red curve. To calculate the SNR for the detection noise limit in Equation (5.3), we take the initial SNR of the measurement for a fully coherent state and correct it for the decoherence of the state. In addition, the phase shifter for the feedback was not precisely calibrated and had an accuracy of $\pm 2°$ for each angular position, as reported in the datasheet and confirmed experimentally. In our feedback control scheme with the reconstruction of the phase, this has a similar effect as the uncertainty in the final phase read out. The uncertainty from the phase shifter is therefore added in variance to the uncertainty from the final measurement. The phase shifter for the feedback can be a bottleneck in the implementation of the phase lock scheme in other experiments and much attention should be dedicated to its choice and calibration.

Without decoherence and Dick effect, the clock uncertainty would decrease as $1/N$ because of the long dead time. In general, depending on the initial ratio between interrogation time and dead time, the detection noise limit scales between $1/N$ and $1/\sqrt{N}$ in this ideal case. The decoherence from the probe and the trap damps this evolution and leads to a lower gain. With no or low decoherence, the Dick limit would be the dominating limit in our experiment. Starting from $N = 18$, the clock instability increases again because of the decay of the mean spin vector. In other experiments, it is likely that this limit will be the vacuum lifetime of the atoms instead of the dephasing in the trap.

Figure 5.12 shows the general potential of the atomic phase lock to improve an atomic clock. In state-of-the art atomic clocks, the LO is usually not dominated by white frequency noise (chosen here because it is easier to generate), but by $1/f$ noise. In the next step, the atomic phase lock should be implemented in an existing clock with a long interrogation time limited by $1/f$ noise.

5.5. Variations of the Feedback Protocol

5.5.1. Feedback on the Atomic Phase

The feedback protocol can be also applied if the feedback is not performed on the LO but on the atoms itself. The feedback on the atoms is similar to that presented in Chapter 4, and the pulse sequence is shown in Figure 5.13. The difference to the previous feedback scheme is that the spin state is not brought close to the x-axis by feedback on the phase of the LO but by a microwave pulse on the atoms. After the feedback, the relative phase between the LO and the atoms is the same as in the previous scheme. Since there is no feedback on the LO, it is the atomic phase which is changed.

The practical advantage of the protocol is that in principle no phase shifter for the LO is needed[4]. Otherwise, the feedback protocol is the same as described in the preceding section.

[4]The rotations around the different axis around the Bloch sphere could be also implemented by setting a large offset on the LO for a short duration.

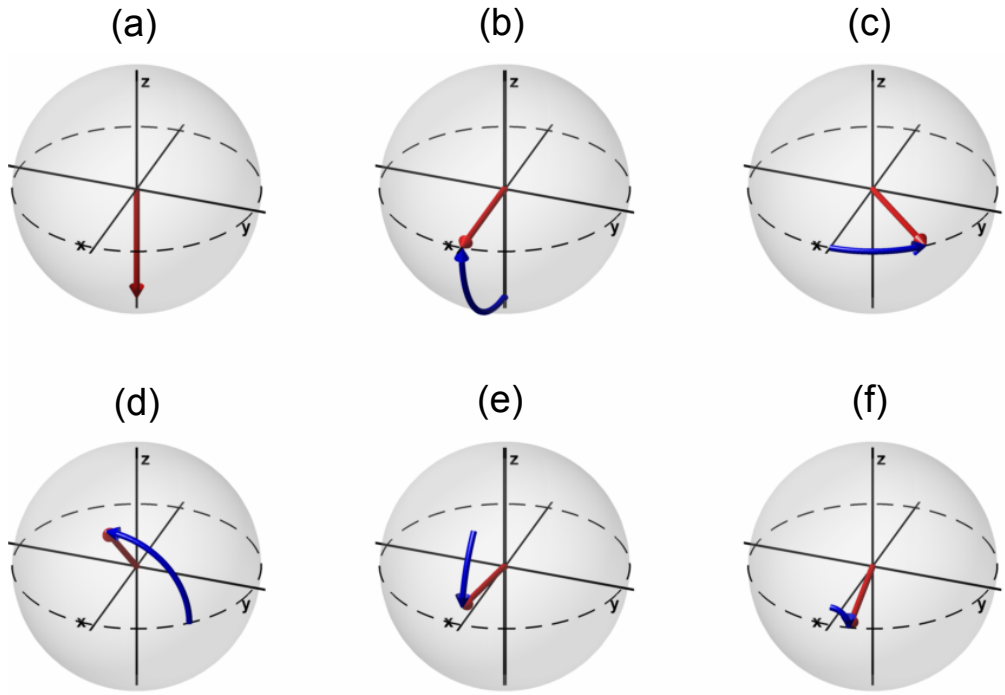

Figure 5.13.: Scheme for locking the atomic phase on the LO phase. Steps (a) to (d) are the same as for the protocol in Section 5.3. A microwave pulse in (e) turns the state back on the equatorial plane of the Bloch sphere. The last rotation in (f) is used to account for errors from the uncertainty of the weak measurement.

5.5.2. Auxiliary Atomic Ensemble

The atomic phase lock faces the same problem as in spin squeezing, the possibility that it could introduce systematic errors (for example by the spontaneous emission induced by the measurements). Such errors can be estimated and corrected, but should be better avoided. A scheme which would strongly suppress possible systematic errors is shown in Figure 5.14, and uses two atomic ensembles.

The idea is that the weak intermediate measurements are only applied on one atomic auxiliary ensemble (Atoms 1), and the main atomic ensemble (Atoms 2) is operated as a conventional atomic clock. The main clock ensemble is not manipulated during the phase lock stage, but its interrogation time is nevertheless significantly increased. As before, the phase shifter should be better characterized than the limit given by the atomic projection noise.

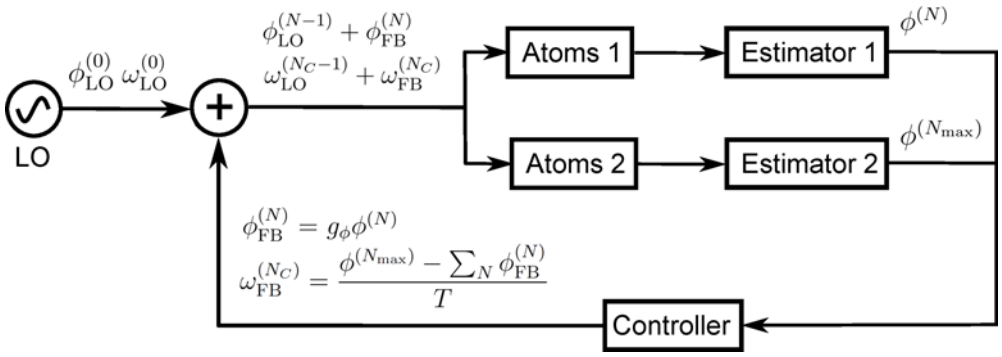

Figure 5.14.: Atomic phase lock with auxiliary clock ensemble. The weak measurements and intermediate state rotations are only applied on ensemble "Atoms 1". The main ensemble "Atoms 2" is operated with the standard Ramsey protocol, with the difference that the total phase drift is reconstructed from the intermediate phase shifts and the final phase measurement.

The scheme from Figure 5.14 is a possible solution for optical lattice clocks, which are often already operated with two clock ensembles [Hinkley 13, Bloom 13]. In addition, it could also be used if the main clock (atoms 2) is not an atomic ensemble but only a single ion, which might be advantageous to reach a better accuracy in the clock. One could, for example, combine a mercury lattice clock (auxiliary) with a single mercury ion (main).

5.6. Other Proposals to Increase Interrogation Time in Atomic Clocks

In competition with the atomic phase lock, two other proposals to increase the interrogation time in atomic clocks recently appeared. They are shortly summarized below with a discussion of their advantages and disadvantages.

Cascaded frequency stabilization In [Borregaard 13a], it was proposed to stabilize the LO frequency on one atomic ensemble with a maximal interrogation time T_1, and to use the stabilized LO for the interrogation of another ensemble with a longer interrogation time T_2. The procedure can be repeated with more

atomic ensembles, so that the interrogation time T for the last ensemble is not limited by the LO noise.

The advantage of the scheme is that it already works with a low number of atoms per ensemble, down to seven atoms. The phase lock scheme requires a higher atom number because of the condition that the mean spin direction is preserved after the intermediate measurements. The disadvantage of the proposed scheme is that it requires very high experimental resources. The protocol in [Borregaard 13a] was devised for zero dead time operation, and realistically always two ensembles are at least required then for each stabilization step. The scheme for the cascaded frequency stabilization would need the development of new experimental setups in which a large number of atomic ensembles can be operated simultaneously.

Phase reconstruction with several atomic ensembles In [Rosenband 13], a strategy very similar to the one above was proposed, in which the total phase drift in an interrogation time T is reconstructed from the phase drifts from clocks operating either at different frequencies or interrogation times. For the example of different interrogation times, the idea is that the measurements on atomic ensembles operated with an interrogation time T_1 can be used to reconstruct the number of phase wraps in an interrogation time $T_2 = DT_1$, where D is an integer number. Again, several of those reconstruction steps can be cascaded with the addition of more atomic ensembles.

In [Kessler 13], it has been shown that the strategy can be extended so that also for GHZ-states a longer interrogation time can be reached. For the proposed phase reconstruction method, the same advantages and disadvantages as in the scheme with the cascaded frequency stabilization apply.

5.7. Application of Atomic Phase Lock to Other Sensors

The atomic phase lock scheme can be applied to any type of atomic interferometer. In matter-wave interferometers, the atoms travel in a superposition of different paths in real space and interfere. The requirement to apply the atomic phase lock is that the matter-waves are periodically overlapped, such that a weak

measurement of the phase can be performed. In the following, examples for such schemes combined with the atomic phase lock are given.

5.7.1. Gravimeter

An atomic gravimeter is an interferometer especially designed for measuring the gravitational acceleration g. In an atomic gravimeter, the equivalent of the LO is the reference frame used to make the acceleration measurement. As an example, in a Ramsey-Bordé interferometer, the mirrors for the reflection of the Raman beams can vibrate. This leads to a loss of phase information. Similar to the inversion problem in an atomic clock, if the phase noise becomes too large, the output signal becomes ambiguous and the sensitivity is reduced (see e.g. [Sorrentino 12]). This gives an effective limit for the interrogation time as in an atomic clock.

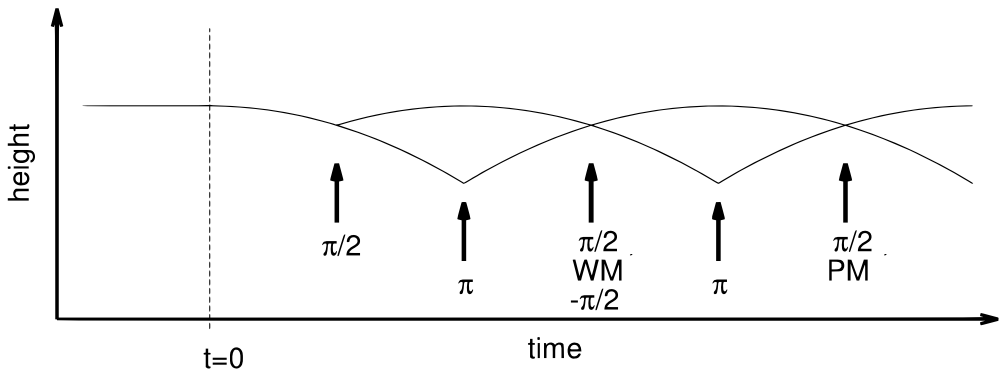

Figure 5.15.: Raman-Bordé interferometer in bouncing configuration with atomic phase lock. In the overlap regions weak measurements on the atomic phase and feedback on the Raman beams is performed.

The atomic phase lock can be combined with a Ramsey-Bordé interferometer in a bouncing configuration as shown in Figure 5.15. In this interferometer, after the splitting of the matter-waves with a $\pi/2$-pulse, the trajectories cross repeatedly thanks to π-pulses [Impens 06]. The beam-splitter and mirror pulses are performed with counter-propagating beams for a stimulated Raman transitions [Kasevich 91]. In the overlap regions, the phase could be read out with a fast sequence of a $\pi/2$-pulse, a weak measurement (WM), and a $-\pi/2$-pulse. Feedback

can then be applied either on the mirror for the Raman beams or preferentially on the phase of the Raman beams. As before, a final precise measurement (PM) is performed at the end, to precisely evaluate the phase evolution after the extended interrogation time.

The scheme is not limited to interferometers in a levitated configuration, but can also be used with free falling clouds as shown in Figure 5.16. The application of the atomic phase lock requires the insertion of intermediate π-pulses to cross the matter waves.

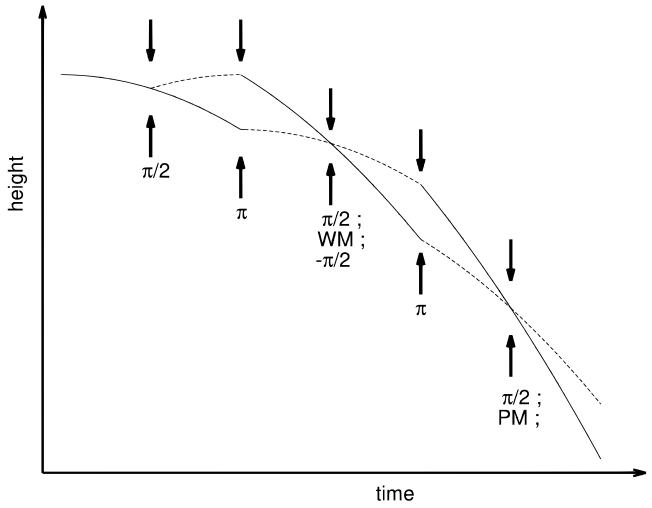

Figure 5.16.: Ramsey-Bordé interferometer with free falling atomic ensemble and atomic phase lock.

5.7.2. Gyroscopes

As a final example, the atomic phase lock could be applied to a gyroscope on an atom chip as it is currently under development [Alzar 12]. The basis of such a gyroscope is the Sagnac effect with which rotations can be measured. As shown in Figure 5.17, the atoms are confined in a ring potential in which they can travel in a superposition of two paths. In the overlap region (every half-turn) a weak measurement of the phase can be performed, and feedback on the Raman beam splitters applied. The same rules for the reconstruction of the total phase apply as discussed in the previous examples.

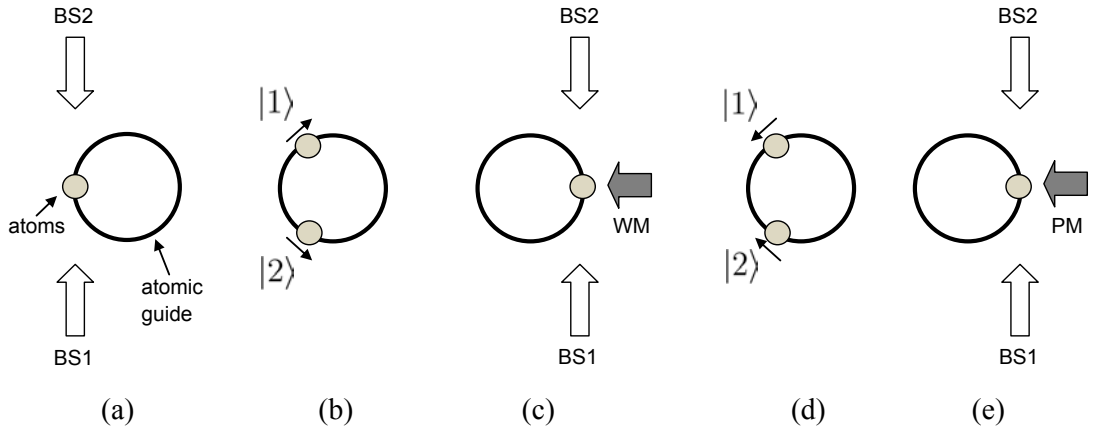

Figure 5.17.: Gyroscope with atoms trapped in a ring potential. (a) Splitting of the wavefunction with a beams splitter (BS). (b) Free interrogation. (c) Weak measurement (WM). (d) Free interrogation. (e) Final precise measurement (PM). Steps (a)-(d) can be repeated several times until the precise final measurement (PM) is performed.

The prospective gain of the atomic phase lock for inertial sensors is even higher than for atomic clocks, because their sensitivity scales as the square of the interrogation time T. A particular interest of the phase lock could be for inertial sensors which are operated in harsh environments such as on an airplane [Geiger 11]. The list of possible configurations in which our feedback scheme could improve atomic interferometers is not exhaustive. The feedback protocol can be in principle applied to any type of interferometer in which the two halves of the split wavefunction can be periodically overlapped.

6. Conclusion

The objective of this thesis was to explore new paths for the operation of atomic interferometers. The main result has been to stabilize atoms in a superposition state against perturbations from the environment, and to develop strategies to convert this to metrological gain in atomic interferometers.

During the course of this PhD work, we have introduced several new techniques and ideas. One of the first results was the all-optical evaporation to Bose-Einstein condensation in an optical cavity in a butterfly configuration. This is an interesting solution for the all-optical condensation to quantum degeneracy with a low optical power consumption. In further work with the optical cavity, we adopted a new technology for the serrodyne frequency shifting of light, and implemented it in a novel laser stabilization scheme. We showed that our scheme performs better than a conventional scheme relying on an AOM for several parameters like the correction bandwidth, correction range and optical losses. Nevertheless, because of spurious frequency components in the serrodyne frequency shifting, the laser stabilization scheme is at the moment not suited for the absolute frequency stabilization of lasers. It is recommended for experimental situations such as ours, where mainly the intra-cavity field is of interest.

We worked in our experiment with the atomic species ^{87}Rb and an optical dipole trap at a telecom wavelength of 1560 nm. The strong light shift on the D2 line was used for the trap loading with a light-shift induced dark MOT, but it posed problems for the manipulation and measurement of the trapped atomic ensembles. We therefore introduced a method to compensate the light shift from the trap with a laser at a wavelength of 1529 nm, such that the differential light shift on the D2 line is highly suppressed. We are planning to investigate if the light-shift engineering with the 1529 nm laser could be used for more efficient loading schemes of the dipole trap. The high density of atoms in the optical dipole trap led to the problem of multiple scattering events in the state preparation with optical pumping. We have shown a method to nevertheless prepare an ensemble

with pure internal states, but with the cost that only one third of the atoms are kept.

The experimental setup included a nondestructive detection system based on FM spectroscopy, and we showed how to push the probe in free space close to its performance limits. We introduced a scheme to avoid light shifts and asymmetrical spontaneous emission, and optimized the SNR for a given destructivity. It was demonstrated that the detection system can be used to follow Rabi-oscillations in real time with a high precision, and that the atomic projection noise can be resolved. The detection system cannot produce spin squeezed states because of the mixing of the internal states by spontaneous emission and because no optical cavity was used to increase the matter-light coupling. This is planned to be addressed in a new generation of the detection system. Nevertheless, the detection system with a single free space optical beam is a good option in environments with strong vibrations where an optical cavity cannot be used.

Atomic ensembles are usually preferred to single atoms in atomic interferometers because of a higher SNR in the final state read-out. There is a second, much less explored advantage in using atomic ensembles, which is that the phase and population difference of a collective spin state can be measured to a high precision while only causing a small measurement back-action. We presented in this manuscript the first steps to benefit from this property in atom interferometry.

In a first series of experiments, we prepared the atoms in a superposition state and applied artificial noise on the ensemble. We demonstrated that a feedback control system based on weak nondestructive measurements and coherent microwave pulses can at least partially stabilize an atomic coherent spin state. Different parameters to evaluate the feedback system were introduced, and we found that the coherence of the output state is the easiest to be addressed experimentally. We demonstrated then the protection of the coherence of an atomic superposition state against different models of decoherence. The interest of the introduced methods could be to evaluate the performance of a feedback system without having a specific protocol for atom interferometry in mind, and so as a benchmark to compare different feedback systems.

The application of active feedback control to the states in atomic interferometers is a new field, with until now only two theoretical proposals

[Shiga 12, Borregaard 13b] and the experimental results presented in this manuscript. The proposal in [Shiga 12] contains a protocol for the stabilization of the phase of the LO in an atomic clock on the phase of the superposition state in an atomic ensemble. We performed a careful analysis of the scheme, and came to the conclusion that there is room for improvements for the long term clock instability. This motivated us to develop a new feedback protocol, which could be also applied to others kinds of atomic interferometers.

We experimentally read out periodically the phase difference between the LO and the atoms in a superposition state, and applied feedback on the phase of the LO. This showed that a classical oscillator can be stabilized on an atomic ensemble in a superposition state. It was demonstrated that feedback on the LO can avoid phase drifts outside the region where the phase can be unambiguously determined. This enables a longer interrogation time in an atomic clock, which reduces effectively the white frequency noise limit from uncorrelated phase measurements and feedback on the LO frequency.

The main application area for the atomic phase lock is for systems where the LO noise is the dominating decoherence source. This condition was not fulfilled in our experiment for atomic clock operation because of the dephasing in the dipole trap. We nevertheless implemented the full feedback protocol for demonstration purposes, and added for this a high level of white frequency noise to the LO. We showed that the basic principle of the full feedback scheme worked, which is the reconstruction of the total phase drift in an interrogation time T from the applied and measured phase shifts. The scaling of the clock instability with the number of phase lock cycles indicates the possible gain in other interferometers.

The atomic phase lock has a similar status as spin squeezing, the basic operation principles have been demonstrated, but the application to state-of-the-art interferometers such as clocks, gravimeters or gyroscopes remains to be shown. The key difficulty will be to avoid systematic errors from the nondestructive measurements and the intermediate state rotations. In our experiment, it could be interesting to return to the initial orientation of the experiment and to implement the cavity-aided nondestructive detection. Spin squeezing itself has been demonstrated by several different groups, but applying it to a gravimeter remains an interesting goal. Along the same lines, the presented feedback protocols for the atomic phase lock for inertial sensors could be tested in our experiment.

The work in this thesis has raised a new set of questions. The formulations for general state operations and quantum measurements are contained in this manuscript, but we addressed only a limited class of feedback scenarios. In atomic interferometers with low particle numbers, the intermediate state measurements will be necessarily partially projective, and more sophisticated feedback protocols have to be designed. Another question is how an atomic interferometer with the new feedback control methods can be optimized with respect to all available experimental resources. Also, a detailed treatment of the Dick effect in the new atom interferometer operation schemes should be performed, in order to make reliable predictions. The findings in this manuscript will hopefully serve as a good starting point for studies in these directions.

A. Weak Measurements of CSSs with Postselection

This appendix shall clarify the difference between weak measurements with and without postselection. It should further indicate a limitation on weak value amplification in atom interferometry. Another point is the introduction to the interesting concept of the two-state vector formalism in quantum mechanics.

A.1. Presentation of a Simple Example

We take the simple example in Figure A.1, where a CSS is prepared along the the x-axis on the equator of the Bloch sphere at time t_1. At a time $t > t_1$ we perform a very weak Gaussian measurement (with an uncertainty much larger than the wavefunction) along the z-axis. At a later time $t_2 > t > t_1$, a projective measurement along the z-axis is performed. The experiment is repeated several times, and binned according to the measurement results of the last projective measurement. We assume that we only take the very rare case that the last projective measurement found all particles projected up (this is the postselection).

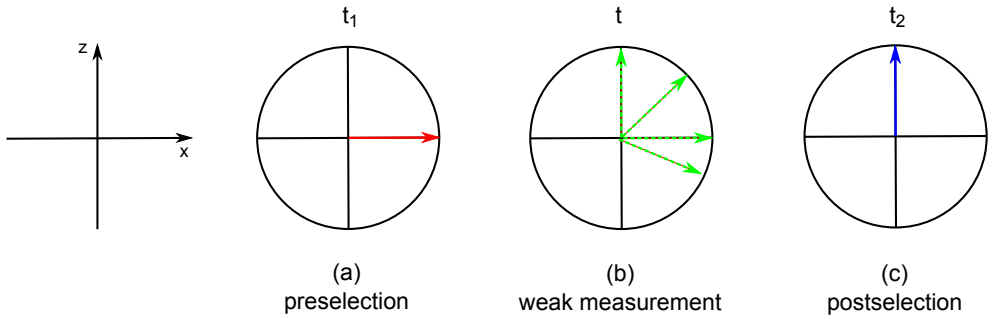

Figure A.1.: Example considered in the following calculations. (a) A CSS prepared at time t_1 along the x-axis of the Bloch sphere. (b) Weak measurement along the z-axis of the Bloch sphere. (c) A final projective measurement finds all spins projected up.

What would one intuitively predict for the result of the intermediate weak measurement? We know that the projectivity from the weak measurement is very small and cannot project all the spins up. If we obtain the result from the weak measurement that all spins are up, one could nevertheless even find all spins projected down in the final projective measurement. Because the intermediate measurements have almost no impact on the result of the final measurement, and the state was prepared on the equator, one could therefore argue that the results for the weak measurements will be distributed around the equator of the Bloch sphere, independently of the result of the later projective measurement. It will be shown below that the opposite is true. The results of the weak measurements on the z-axis will be always distributed around the result of the later projective measurement on the z-axis.

Predictions of the above form were at first made in the context of a time symmetric formulation of quantum mechanics, the two-state vector formalism (TSVF) [Aharonov 90, Aharonov 07]. In the TSVF it is postulated that there are quantum states both travelling forward in time (the preselected states) and backwards in time (the postselected states). The constraints both from the future and the past quantum states decide the results of intermediate measurements. This gives an intermediate explanation for the results of the above experiment: because the postselected quantum state travels back in time, it imposes the constraint that all spins are actually prepared up at time t. The expectation value of the weak measurement along the the z-axis is therefore to find all particles up.

If at time t we would instead perform a weak measurement along the diagonal between the x- and z-axis, we would measure a spin with a factor $\sqrt{2}$ longer than the original spin. This is because the preselected state imposes a full spin along the x-axis and the postselection a full spin along the z-axis. Weak measurements of this kind combined with postselection are the basis of weak value amplification schemes where systematically larger values are found for properties than they should be allowed. The predictions of the TSVF have been experimentally verified in a series of experiments [Ritchie 91, Hosten 08, Dixon 09]. However, the question should be raised if the same predictions cannot be made as well with standard quantum mechanics. It is shown below that at least for the above example with a weak measurement on a CSS standard quantum mechanics makes the same predictions, which requires only the right use of generalized measurement operators and Bayesian inference. After this the calculation for the same example in the

TSVF is shown.

A.2. Calculation with Standard Quantum Mechanics

We take the Equations (1.83) and (1.84) for generalized quantum measurements from Chapter 2. The initial preselected state is $|\Psi_{\text{in}}\rangle = \left|\theta = \frac{\pi}{2}, \varphi = 0\right\rangle$. The probability to measure a result m_w with the weak measurement is given by

$$p\left(m_w\right) = \langle\theta,\varphi| M_{m_w}^{\dagger} M_{m_w} |\theta,\varphi\rangle \tag{A.1}$$

$$= \frac{1}{\sqrt{2\pi}} \frac{\xi}{\sigma_{\text{det}}} \exp\left[-\frac{\xi_\theta^2 m_w^2}{2\sigma_{\text{det}}^2}\right] , \tag{A.2}$$

and the state after the weak measurement is

$$|\Psi_w\rangle = \left(2\pi \frac{1}{1+\kappa^2} J\right)^{-1/4} \sum_{m=_J}^{J} e^{-\frac{\left(m - \frac{\kappa^2}{1+\kappa^2} m_w\right)^2}{2\frac{1}{1+\kappa^2}J}} e^{-i(J+m)\phi} |J,m\rangle \ . \tag{A.3}$$

The postselected state after the final projective measurement is $|\Psi_f\rangle = |J, m = J\rangle$. We ask at first the question about the probability to obtain the postselected state which is directly given with

$$p(\Psi_f|m_w) = |\langle J, m = J|\Psi_w\rangle|^2 \ . \tag{A.4}$$

The multiplication of $p(\Psi_f|m_w)$ with $p(m)$ gives from Bayesian inference the probability weight to have had the measurement result m_w which influenced to have the final state Ψ_f. After normalization of the probability distribution of the weak measurement results from standard quantum mechanics (SQM) is

$$p_{SQM}(m_w|\Psi_f) = \left(2\pi\sigma_{\text{det}}^2\right)^{-1/2} e^{-\frac{1}{2\sigma_{\text{det}}^2}(m_w - J)^2} \ . \tag{A.5}$$

A.3. Calculation with Time Symmetric Quantum Mechanics

In the TSVF, there is a preselected state $\langle\Psi_{\text{in}}|$ travelling forward in time and postselected state $|\Psi_f\rangle$ travelling backwards in time. The probability to have a result m_w for the weak measurement at an intermediate time t is inferred from the form of the measurement operator and the constraints from the past and the future. In the case that all three are written in the same basis, this corresponds

to multiplying the wavefunction from the past and the future, and to convolve it with $E_w = M_{m_w}^\dagger M_{m_w}$. In general, the probability distribution is obtained from [Aharonov 90]

$$p(m_w|\Psi_f) = \frac{\langle\Psi_{\text{in}}|\, M_{m_w}^\dagger M_{m_w}\, |\Psi_f\rangle}{\langle\Psi_{\text{in}}|\Psi_f\rangle}\ , \tag{A.6}$$

which gives for our case

$$p_{TSVF}(m_w|\Psi_f) = \left(2\pi\sigma_{\text{det}}^2\right)^{-1/2} e^{-\frac{1}{2\sigma_{\text{det}}^2}(m_w-J)^2}\ . \tag{A.7}$$

We see from Equations (A.5) and (A.7) that the predictions from SQM and the TSVF for weak measurement results are the same. Nevertheless, the calculation for the TSVF was easier and could be done in a single line. There is no known proof that SQM and the TSVF give in general the same predictions, but the above results strongly suggest that this is the case for the collective spin systems treated in this thesis.

The major drawback of weak measurements with postselection is in general the low probability to obtain desired results for the postselection. If one would for example like to perform a weak value amplification by a factor $\sqrt{2}$ on a CSS, this would require $2^{N_{\text{at}}}$ experimental repetitions to find the final state in which all spins are projected up. Even if there would be a proof that weak value amplification could lead to metrological gain for atom interferometry, the number of required experimental cycles might be just too high for systems with high atom numbers.

B. Level Structure of Rubidium-87

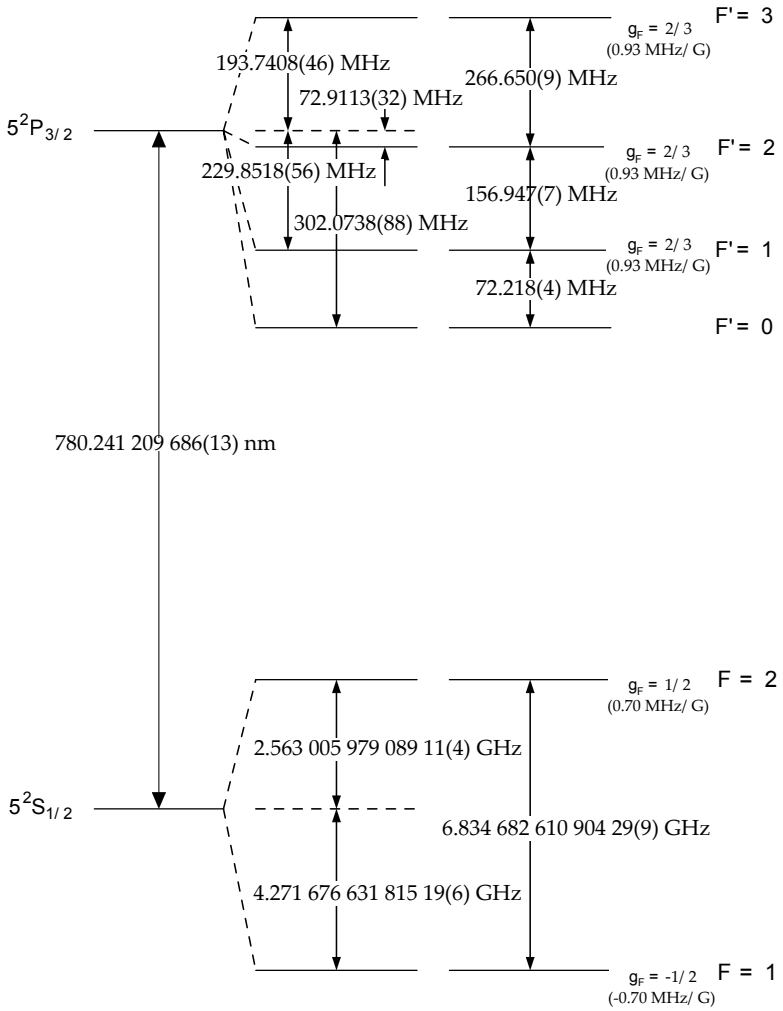

Figure B.1.: Atomic levels on the D2-line of ^{87}Rb, taken from [Steck 01]. Each of the the hyperfine states splits under a magnetic field in $2F+1$ magnetic sublevels m_F, which are not shown.

C. Atomic Polarizabilities and Branching

C.1. Polarizability

The polarizability of an atomic level μ is given by [Grimm 00]

$$\alpha_\mu = \frac{1}{\hbar} \sum_k \frac{|\langle k \,|\mathbf{d}|\, \mu \rangle|^2 \, \omega_{k,\mu}}{\omega_{k,\mu}^2 - \omega^2} \,, \tag{C.1}$$

where ω is the frequency of the light and $\omega_{k,\mu}$ are the transition frequencies. In general, the states k, μ are each designated with atom numbers L, I, J, F, and m_F where L is the angular momentum of the outer electron, I is the nuclear atomic momentum, $J = L + S$ is the total electron angular momentum with $S = 1/2$, and $F = I + J$.

We used the approach presented in [Safronova 04] for the calculation of the polarizabilities of the $5P_{3/2}$ and $5S_{1/2}$ states from the radiation at 1550 nm and 1529 nm in Section 2.6.1. From the Wigner-Eckart theorem, the polarizability of a state with total angular momentum J_μ from linearly polarized light can be written as [Budker 04]

$$\alpha_\mu = \alpha_0 + \alpha_2 \frac{3m_{J_\mu} - J_\mu(J_\mu + 1)}{J_\mu(2J_\mu - 1)} \,, \tag{C.2}$$

where α_0 is called the scalar polarizability and α_2 is the tensor polarizability. We assumed that the scalar polarizability is dominating, which can be written as [Safronova 04]

$$\alpha_0 = \frac{2}{3(2J_\mu + 1)} \sum_k \frac{d_{k\mu}^2 \omega_{k,\mu}}{\omega_{k,\mu}^2 - \omega^2} \,, \tag{C.3}$$

where $d_{k\mu}$ is a reduced dipole element and the sum is only performed over different total angular momentum states. The relevant reduced dipole elements for our experiment are summarized in Table C.1.

The above calculations require that the laser is far detuned from the hyperfine

Transition	$d_{k\mu}$ (in ea_0)	λ (in nm)
$5P_{3/2} \rightarrow 6S_{1/2}$	6.047	1366.875
$5P_{3/2} \rightarrow 4D_{3/2}$	3.633	1529.261
$5P_{3/2} \rightarrow 4D_{5/2}$	10.899	1529.366
$5S_{1/2} \rightarrow 5P_{1/2}$	4.221	794.979
$5S_{1/2} \rightarrow 5P_{3/2}$	5.956	780.241

Table C.1.: Dipole elements of ^{87}Rb (from [Arora 07]).

splitting of the considered states. For the calculations of the couplings and light-shifts on the D2 line in ^{87}Rb in Chapter 3 this condition is not given. As described in the main text, we took here the dipole moment and relative transition strengths S as already calculated in [Steck 01].

C.2. Branching Ratios from Spontaneous Emission

The calculation in Section 3.4.3 required the knowledge of the probability to fall from one excited state to the different ground state levels. To calculate the branching ratio for each set of transitions $(F', m'_F = 0) \rightarrow (F = 1, 2, mf = -1, 0, +1)$, we normalize the probability for each transition (the squared transition coefficients S) by the sum of all probabilities (which is here always 1/2). The probabilities to fall from $(F', m'_F = 0)$ to the different ground state levels is listed in Table C.2.

	$F = 2$		$F = 1$	
	$m_F \pm 1$	$m_F = 0$	$m_F \pm 1$	$m_F = 0$
$F' = 3$	1/5	3/5	0	0
$F' = 2$	1/4	0	1/12	1/3
$F' = 1$	1/20	1/15	5/12	0
$F' = 0$	0	0	1/3	1/3

Table C.2.: Branching ratios from $(F', m'_F = 0)$ to the magnetic ground state levels in $F = 1$ and $F = 2$

D. Dephasing in Dipole Trap

The dipole trap at 1560 nm causes a differential light-shift between the hyperfine ground states of ^{87}Rb. Atoms at different positions in the dipole trap have then a different energy difference between the hyperfine states. This implies that after a CSS is prepared on the equator of the Bloch sphere, the single spins dephase with time. In an atomic clock, this dephasing can not be removed with spin echos because this would result in the loss of phase information. The dephasing between the spins is then an effective decoherence source.

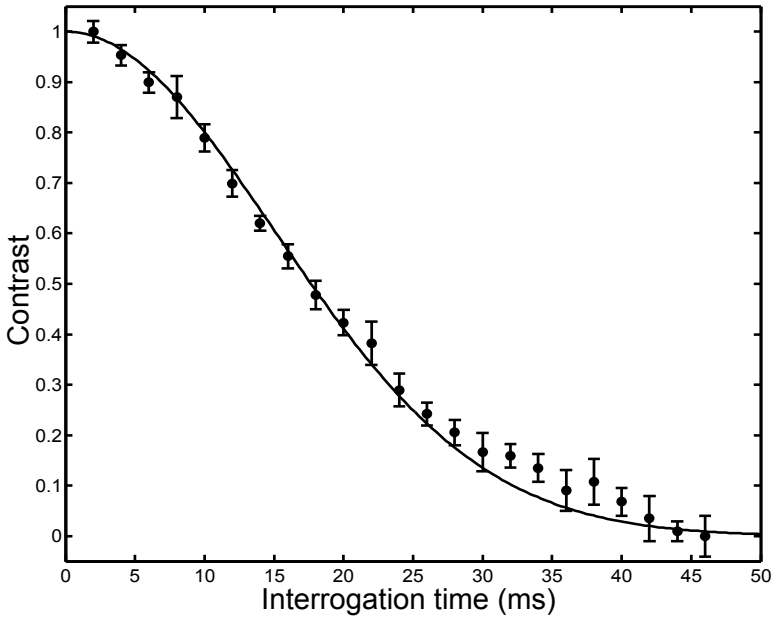

Figure D.1.: Measurement of the dephasing of the atomic states in the optical trap. The measured points (black circles) are the contrast of a Ramsey interferometer as a function of the interrogation time. The data are fitted with a Gaussian decay.

The dephasing in the dipole trap is measured with a Ramsey interferometer sequence. We prepare a superposition state with a $\pi/2$-pulse, let the state

evolve freely for a varying interval, and close the interferometer with another $\pi/2$-pulse. The interferometer is read-out with our nondestructive detection system and the result is shown in Figure D.1. The solid line is a fit with a Gaussian decay $\mathcal{C}(\tau) = \exp[-\frac{1}{2}(\frac{\tau}{\bar{\tau}})^2]$. The decay was assumed to be Gaussian because of the Gaussian thermal distribution and the Gaussian potential shape. For a temperature of the atoms of 10 μK and 10 W of optical power at 1550 nm in each cavity arm we obtain a decay time of $\bar{\tau} = 15$ ms.

The state decay from inhomogeneous dephasing is the main decoherence source for our experiment in clock operation. The differential light shift from the dipole trap on the hyperfine levels could be in principle partially compensated with a beam at 780 nm between the two hyperfine ground states [Kaplan 02] or with the vectorial light shift from a beam with an elliptical polarization [Dudin 10]. Another possibility would be to enter the regime of spin-self rephasing in the dipole trap [Büning 11].

E. State Parameters Before and After Feedback

We give here the derivation of the formulas for the coherence, von Neumann entropy and fidelity as used in Table 4.1.

E.1. Coherence

We consider a CSS $|\theta,\varphi\rangle$ with $J = N_{\mathrm{at}}/2$, pointing in the (θ,φ) direction. Its expectation value is

$$\langle \mathbf{J} \rangle_{\theta,\varphi} = \begin{pmatrix} \langle J_x \rangle_{\theta,\varphi} \\ \langle J_y \rangle_{\theta,\varphi} \\ \langle J_z \rangle_{\theta,\varphi} \end{pmatrix} = J \begin{pmatrix} -\sin\theta\cos\varphi \\ \sin\theta\sin\varphi \\ -\cos\theta \end{pmatrix} . \tag{E.1}$$

The coherence of the CSS is $\|\langle \mathbf{J} \rangle_\theta\| / J = 1$. An arbitrary statistical mixture of CSSs $\{|\theta_k,\varphi_k\rangle\}$ can be described by the density matrix

$$\rho = \sum_k p_k \left|\theta_k,\varphi_k\right\rangle \left\langle\theta_k,\varphi_k\right| \ , \tag{E.2}$$

where $\sum_k p_k = 1$. From the linearity of the trace, we have for $l = x, y, z$:

$$\begin{aligned} \langle J_l \rangle (\rho) &= \mathrm{Tr}\left(J_l \rho\right) && \text{(E.3)} \\ &= \sum_k p_k \mathrm{Tr}\left(J_l \left|\theta_k,\varphi_k\right\rangle \left\langle\theta_k,\varphi_k\right|\right) && \text{(E.4)} \\ &= \sum_k p_k \langle J_l \rangle_{\theta_k,\varphi_k} , && \text{(E.5)} \end{aligned}$$

therefore, the mean Bloch vector related to the density operator ρ is

$$\langle \mathbf{J} \rangle (\rho) = \sum_k p_k \langle \mathbf{J} \rangle_{\theta_k,\varphi_k} . \tag{E.6}$$

The coherence of the mixture ρ, $\eta(\rho) = \|\langle \mathbf{J} \rangle(\rho)\| / J$ is then

$$\begin{aligned} \eta(\rho) &= \left[\left(\sum_k p_k \sin\theta_k \cos\varphi_k\right)^2 + \left(\sum_k p_k \sin\theta_k \sin\varphi_k\right)^2 \right. \\ &\quad \left. + \left(\sum_k p_k \cos\theta_k\right)^2\right]^{1/2}. \end{aligned} \tag{E.7}$$

Using this relation and the expressions for the noise $\mathcal{E}_\alpha(\rho_0)$ (eq. (4.6)) and the feedback controller $\mathcal{C}_\alpha(\rho_0)$ (eq. (4.13)), one obtains the values of the coherence given in Table 4.1. Note that in the case $\varphi_k = 0$, we have the simple relation:

$$\eta(\rho) = \left|\sum_k p_k e^{i\theta_k}\right|. \tag{E.8}$$

All these results obtained for a discrete probability distribution p_k can be generalized to a continuous distribution $p(\theta)$ $(-\pi \leq \theta \leq \pi)$ by the replacement $\sum_k \to \int d\theta$.

E.2. Fidelity

The fidelity with respect to an initial state $|\psi_0\rangle = |\theta_0, \varphi_0\rangle$ is

$$\mathcal{F}(\rho, |\psi_0\rangle) = \langle\psi_0|\,\rho\,|\psi_0\rangle \tag{E.9}$$

$$= \sum_k p_k \left|\langle\theta_0, \varphi_0|\,\theta_k, \varphi_k\rangle\right|^2. \tag{E.10}$$

We expand the CSS $|\theta, \varphi\rangle$ in the Dicke basis $|J, m\rangle$,

$$|\theta, \varphi\rangle = \sum_{m=-J}^{J} \binom{2J}{J+m}^{1/2} \sin^{J+m}\frac{\theta}{2} \cos^{J-m}\frac{\theta}{2} e^{-i\varphi(J+m)} |J, m\rangle, \tag{E.11}$$

which gives then the overlap between two CSSs

$$\langle\theta, \varphi|\,\theta', \varphi'\rangle = e^{-iJ(\varphi-\varphi')}\left[\cos\frac{\theta}{2}\cos\frac{\theta'}{2} + e^{i(\varphi-\varphi')}\sin\frac{\theta}{2}\sin\frac{\theta'}{2}\right]^{2J}. \tag{E.12}$$

This can be approximated with a Gaussian distribution for a large number of atoms $(J \gg 1)$ to

$$\left|\langle\theta, \varphi|\,\theta', \varphi'\rangle\right|^2 \sim e^{-\frac{J}{2}\left[(\theta-\theta')^2 + \frac{1}{2}(1-\cos 2\theta')(\varphi-\varphi')^2\right]}. \tag{E.13}$$

Finally, using Equations (E.10) and (E.13), one can evaluate the fidelity of the mixture ρ.

E.3. Von Neumann Entropy

Equation (E.13) implies that whenever the RCR angle is large enough so that the angles between the CSSs in the statistical mixture ρ are large compared to the atomic shot-noise,

$$\forall k \neq k', \begin{cases} \theta_k - \theta_{k'} \gg 1/\sqrt{N_{\mathrm{at}}} \\ \text{or} \\ \varphi_k - \varphi_{k'} \gg 1/\sqrt{N_{\mathrm{at}}} \end{cases} \tag{E.14}$$

then the CSSs that compose the mixed state $\rho = \sum_k p_k \left|\theta_k, \varphi_k\right\rangle \left\langle\theta_k, \varphi_k\right|$ are almost orthogonal,

$$\left\langle\theta_k, \varphi_k\right| \left.\theta_{k'}, \varphi_{k'}\right\rangle \sim \delta_{k,k'} \ . \tag{E.15}$$

In this case, the von Neumann entropy of ρ satisfies

$$S(\rho) \sim -\sum_k p_k \log_2 p_k \ . \tag{E.16}$$

Combining this relation and the expressions $\mathcal{E}_\alpha(\rho_0)$ (Equation (4.6)) and $\mathcal{C}_\alpha(\rho_0)$ (Equation (4.13)), provides the values of the von Neumann entropy in Table 4.1.

F. Dick Effect under 1/f-Noise

We discuss here the scaling of the Dick effect under $1/f$-noise, as it is mentioned in the main text. An analytical solution for the Fourier components of the sensitivity function under Ramsey operation is given by [Santarelli 96]:

$$g_0 = \frac{4}{T_C}\left(\frac{T}{2} + \frac{2\tau_{\pi/2}}{\pi}\right) , \tag{F.1}$$

$$g_n = \frac{2T_c\left(4n\tau_{\pi/2}\cos\left(\frac{\pi\left(nT+2n\tau_{\pi/2}\right)}{T_C}\right) + T_C\sin\left(\frac{n\pi T}{T_C}\right)\right)}{n\pi\left(T_C^2 - \left(4n\tau_{\pi/2}\right)^2\right)} . \tag{F.2}$$

Furthermore, in the case of $1/f$ noise with a flat Allan deviation $\sigma_{1/f}$, the spectral noise density of the free running LO is described by

$$S_y^{LO}\left(f_c\right)) = \frac{1}{2\ln\left(2\right)}\frac{\sigma_{1/f}^2}{f} . \tag{F.3}$$

Equation (5.4) becomes in this case [Dick 87]

$$\sigma_{y,Dick} = \frac{\Delta f}{f} = \sqrt{\frac{1}{\tau}\frac{T_C}{2\ln\left(2\right)}\frac{\sigma_{1/f}^2}{g_0^2}\sum_{n=1}^{\infty}\frac{g_n^2}{n}} . \tag{F.4}$$

Equations (F.1), (F.2) and (F.4) can be used to estimate the expected Dick limit in the clock operation with $1/f$ noise. In Figure F.1, the characteristic scaling of the Dick limit as a function of the dead time is shown in blue. We assume $\sigma_{1/f} = 2\times10^{-9}$, $T = 1$ ms and $\tau_{\pi/2} = 47$ μs. The length of the dead time defines the duty cycle $d = \frac{T_C - T_D}{T_C}$. For a comparison, the detection noise limit with SNR $= 100$ and $f = 6.835$ GHz for the same parameters is given (red).

The Dick limit is rapidly decreasing with the duty cycle since nearly all phase drifts are detected. The detection noise limit follows the scaling from Equation (5.3) and reaches $\sigma_{y,\mathrm{det}} = 4.8\times10^{-11}s^{-1}\frac{1}{\sqrt{\tau}}$ at $d = 1$. Figure F.1

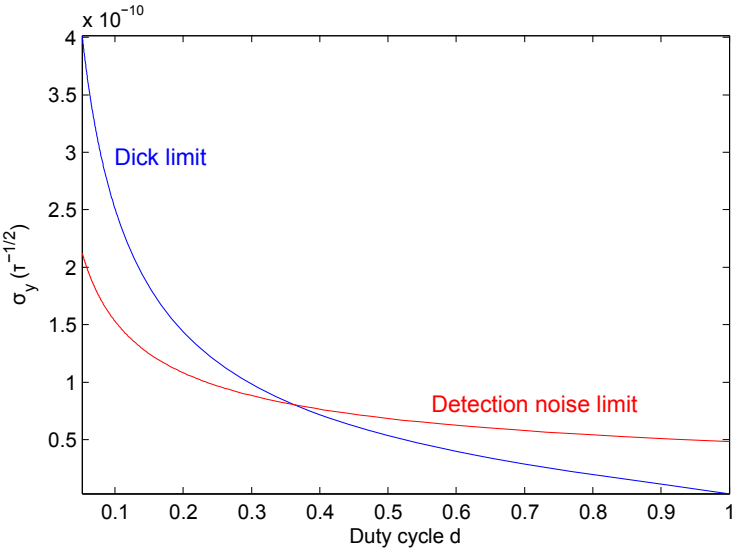

Figure F.1.: Characteristic evolution of the Allan deviation under $1/f$ noise as a function of the duty cycle. In blue the Dick limit and in red the detection noise limit. The parameters of the calculation are defined in the main text.

demonstrates the importance of working with a low dead time in an atomic clock. In practice, a dead time approaching zero can be achieved by alternately interrogating two separate atomic ensembles while feedback on the same LO is performed. With this interleaving technique the state of one atomic ensemble is prepared, while the other is interrogated, and the contribution from the Dick effect is highly suppressed and even removed [Biedermann 13]. Another strategy to reduce the Dick limit, called synchronous detection, consists in the splitting of the LO signal and the separate stabilization of the signals on one atomic ensemble each. The frequency correction signals from each path are then subtracted and the original frequency fluctuations of the LO are rejected [Bize 00, Takamoto 11].

The interleaving or synchronous detection techniques cannot reduce the white noise limit from detection noise. For this reason, we focused in the analysis of the atomic phase lock technique in Chapter 5 on the detection noise limit.

Acknowledgements

Last but not least, I would like to thank everybody I worked with and who accompanied me in this years of the PhD. I would like to thank Philippe Bouyer and Arnaud Landragin for having proposed and planned such an interesting experimental apparatus. I am very grateful to Arnaud and Philippe that they supported us in leaving the path towards spin squeezing, and to take the risk to work on the feedback experiments. Several groups have started to explore spin squeezing for the improvement of atomic interferometers, but we have been the first to investigate the feedback control of atomic superposition states for this goal. I enjoyed in my PhD time very much the intellectual challenges and creativity which our work required, and I am happy that I was given this opportunity.
When I think back, there are several discoveries and developments in this thesis which make me happy. For example, I remember how much fun it was when we finished the serrodyne stabilization system, and hit the optical table as hard as possible just to see when the feedback loop would unlock. For the nondestructive detection system, I still like the elegance of our method to avoid light shifts from the nondestructive probe, even though it made the technological requirements on the photodiode harder. I am excited about the feedback protocols which we invented, and would like to explore more its applications and modifications with partially projective measurements.
In this PhD time, Alain Aspect has been my official PhD supervisor. I have always been impressed of Alains general knowledge in physics, and his comments on our work. I appreciated very much that when I went to him and asked him about his opinion about weak measurements in time symmetric quantum mechanics, he invited Sandu Popescu to give a talk on this topic at the Institut d'Optique. Thank you very much also to Sandu Popescu, who I enjoyed to talk to.
Andrea Bertoldi has been a postdoc on the experiment during my PhD, and was especially at the end effectively the supervisor of the experiment. I always appreciated Andrea very much on a personal level, he has been always very direct, honest, fair, and interested in me as a person. I liked very much working with Andrea, and I doubt that in many domains I will ever reach his skill level. I hope

very much that Andrea will obtain soon a fixed scientific position and wish him and his family (Martha, Olivia and Amelia) all the best for the future.
I have worked during my PhD time with three other PhD students on the experiment. Simon Bernon was the first PhD student, and he started to build the experimental apparatus. Simons PhD thesis was of great use for me to understand the details of the setup and I thank Simon for introducing me to the experiment. I liked Simons severity and professional approach in the experimental work. After Simon left, I worked with Thomas Vanderbruggen on the experimental apparatus. Thomas taught me how to build stable optical systems (by shaking my mirrors and photodiodes and asking me to realign everything if something moved). I enjoyed the (sometimes quite loud) discussions between Thomas and me, not only about our experiment, but also about general concepts in physics. Many ideas on the experiment came from our discussions late in the evening. I learned from Thomas a great deal about the experimental details of the setup and he prepared me as his successor. Shortly before Thomas left, Etienne Cantin arrived as a Master student and became later a PhD student. The experiment was already planned to move from Palaiseau to the new laboratory in Bordeaux, and Etienne was a PhD student in Bordeaux. It has been a difficult task for Etienne, who started to prepare parts for the experiment in Bordeaux, and travelled always for half a week to Palaiseau to work on the experimental setup. Etienne was always ready to work directly on the experimental setup, even when he missed something, and I have great confidence in Etienne that he will lead the experiment to new interesting results. I wish him a lot of luck in the further experimental work and hope he can rebuild the experiment fast in Bordeaux.
I always enjoyed the strong infrastructure and support at the Institut d'Optique. Although we built most of electronic boards by ourselves, Frédéric Moron from the electronics shop helped us in the design of our electronics components and especially at the beginning of my PhD I was a steady guest in his rooms. Also André Villing was very helpful, especially with the electronic sequencer control boxes. In the mechanics workshop, it was André Guilbaud who helped us with little mechanical components made for our experiment. I would like to thank all administrative staff at the Institut d'Optique, which made my life much easier. I appreciated how tasks like the organization of the travelling to conferences or the ordering of components was (at least in parts) taken over by the administration.
During my time as a PhD student, I was a teaching assistant at the Institut d'Optique. I helped to teach the students in optical labworks (even half of the time in French! I wonder for whom it was harder, for the students or for me), where I

enjoyed very much working with Nicolas Dubreuil and Lionel Jacubowiez. Besides that, I taught LabView to the students (also half in French), where I worked with Frederic Capmas and Jean Marie Feybesse. I thank the Institut d'Optique very much to have given me the opportunity to teach, which let me learn in depth new topics and grow personally.
I was happy to do my PhD in a large group, where some of the PhD students became my best friends. I would like to thank everybody for the nice atmosphere in the group. The permanent researchers in the group, Thomas Bourdel, Isabelle Bouchoulle, David Clément, Laurent Sanchez-Palencia, Vincent Josse, Denis Boiron, Marc Cheneau and Chris Westbrook are all great physicists who I wish exciting results in the future. I would like to thank all PhD students and postdocs, with almost everybody I went to at least one party or had a beer. I could tell to everybody a little story but it would fill to many pages. You should just know that I will never forget you. Thanks to Thomas Plisson, Baptiste Allard, Fred Jendrzejewski, Marie Bonneau, Valentin Volchkov, Giuseppe Carleo, Marie Piraud, Thibaut Jacqmin, Vincent Ménoret, Remi Geiger, Josselin Ruaudel, Bess Fang, Kilian Müller, Guillaume Salomon, Raphael Lopes, Samuel Lellouch, Guilhem Boéris, Yami Fang, Lauriane Fouché, Quentin Bouton, Almazbek Imanaliev, Aisling Johnson and Jérémie Richard. I would like to thank Raphael very much that he lent his old laptop to me so that I could write my PhD thesis on it, that was very nice. I would like to thank Bess and Kilian, who have not only become some of my best friends, but also corrected each a few chapters of my PhD thesis. The same did Benno Rem, who was not a PhD student at the Institut d'Optique but at ENS, and with whom I always enjoyed to drink a beer or/and to talk about physics or other things. Thank you for everything, you are awesome guys.
There is one PhD student of the group who I have not mentioned in the previous list: Lynn Hoendervanger, my girlfriend. It is hard for me to summarize all the support and happiness Lynn gave me. You are wonderful, and here is not even enough space to tell you how much I thank you. If one thing ever counted in my PhD, then it was meeting you.
I would like to thank all my friends and family who supported me during my PhD. I dedicated this manuscript to my family, who not only supported me during my PhD but also in the long educational path before the PhD. It is a shame my father could not see me getting a PhD, but I am sure he would have been proud of me. Thank you for everything dad.
I would also like to thank my physics teachers in school, Mr. Korn and Mr. Weidemann, my math teacher Mrs. Jäger, and all those engaged physics lecturers

at university whose lectures I had the pleasure to attend. I have always admired those lecturers who could convey the passion for the search for truth in physics to their students, thanks to all of you.
It is weird, with my PhD another section of my life comes to its end. I have met so many amazing people, lived in France, went to exciting places and conferences and learned about great Physics. I will surely quite often remember this time. What at the end perhaps counts most, are all those little moments of laughing, excitement and fun. I would like to thank everybody who made me smile, and I hope I let some of you smile too. I wish you all the best for the future, thanks a lot.

Bibliography

[Adams 97] C. S. Adams & E. Riis. *Laser cooling and trapping of neutral atoms.* Prog. Quantum Electron., vol. 21, no. 1, pages 1–79, 1997.

[Aharonov 88] Y. Aharonov, D. Z. Albert & L. Vaidman. *How the result of a measurement of a component of the spin of a spin-1/2 particle can turn out to be 100.* Phys. Rev. Lett., vol. 60, pages 1351–1354, 1988.

[Aharonov 90] Y. Aharonov & L. Vaidman. *Properties of a quantum system during the time interval between two measurements.* Phys. Rev. A, vol. 41, no. 1, page 11, 1990.

[Aharonov 07] Y. Aharonov & L. Vaidman. *The two-state vector formalism: an updated review.* In Time in Quantum Mechanics, pages 399–447. Springer, 2007.

[Aharonov 10] Y. Aharonov, S. Popescu & J. Tollaksen. *A time-symmetric formulation of quantum mechanics.* Physics Today, vol. 63, no. 11, pages 27–32, 2010.

[Ahn 02] C. Ahn, A. C. Doherty & A. J. Landahl. *Continuous quantum error correction via quantum feedback control.* Phys. Rev. A, vol. 65, no. 4, page 042301, 2002.

[Allan 66] D. W. Allan. *Statistics of atomic frequency standards.* Proc. IEEE, vol. 54, no. 2, pages 221–230, 1966.

[Alzar 12] C. L. Garrido Alzar, W. Yan & A. Landragin. *Towards high sensitivity rotation sensing using an atom chip.* In Research in Optical Sciences, page JT2A.10. Optical Society of America, 2012.

[André 04] A. André, A. S. Sørensen & M. D. Lukin. *Stability of Atomic Clocks Based on Entangled Atoms.* Phys. Rev. Lett., vol. 92, page 230801, 2004.

[Appel 09a] J. Appel, A. MacRae & A. I. Lvovsky. *Versatile digital GHz phase lock for external cavity diode lasers.* Meas. Sci. Technol., vol. 20, page 055302, 2009.

[Appel 09b] J. Appel, P. J. Windpassinger, D. Oblak, U. B. Hoff, N. Kjærgaard & E. S. Polzik. *Mesoscopic atomic entanglement for precision measurements beyond the standard quantum limit.* Proc. Natl. Acad. Sci. U.S.A., vol. 106, no. 27, pages 10960–10965, 2009.

[Armen 02] M. A. Armen, J. K. Au, J. K. Stockton, A. C. Doherty & H. Mabuchi. *Adaptive homodyne measurement of optical phase.* Phys. Rev. Lett., vol. 89, no. 13, page 133602, 2002.

[Arora 07] B. Arora, M. S. Safronova & C. W. Clark. *Magic wavelengths for the np-ns transitions in alkali-metal atoms.* Phys. Rev. A, vol. 76, page 052509, 2007.

[Aspect 82] A. Aspect, J. Dalibard & G. Roger. *Experimental test of Bell's inequalities using time-varying analyzers.* Phys. Rev. Lett., vol. 49, no. 25, page 1804, 1982.

[Behbood 13] N. Behbood, G. Colangelo, F. Martin Ciurana, M. Napolitano, R. J. Sewell & M. W. Mitchell. *Feedback Cooling of an Atomic Spin Ensemble.* Phys. Rev. Lett., vol. 111, page 103601, 2013.

[Bell 64] J. S. Bell. *On the einstein-podolsky-rosen paradox.* Physics, vol. 1, no. 3, pages 195–200, 1964.

[Berman 97] P. R. Berman. Atom interferometry. Academic press, 1997.

[Bernon 11a] S. Bernon. *Piégeage et mesure non-destructive d'atomes froids dans une cavité en anneau de haute finesse.* PhD thesis, Ecole Polytechnique, 2011.

[Bernon 11b] S. Bernon, T. Vanderbruggen, R. Kohlhaas, A. Bertoldi, A. Landragin & P. Bouyer. *Heterodyne non-demolition measurements on cold atomic samples: towards the preparation of non-classical states for atom interferometry.* New J. Phys., vol. 13, no. 6, page 065021, 2011.

[Bertoldi 10] A. Bertoldi, S. Bernon, T. Vanderbruggen, A. Landragin & P. Bouyer. *In situ characterization of an optical cavity using atomic light shift.* Opt. Lett., vol. 35, no. 22, pages 3769–3771, 2010.

[Biedermann 13] G. W. Biedermann, K. Takase, X. Wu, L. Deslauriers, S. Roy & M. A. Kasevich. *Zero-dead-time operation of interleaved atomic clocks.* Phys. Rev. Lett., vol. 111, no. 17, page 170802, 2013.

[Bize 00] S. Bize, Y. Sortais, P. Lemonde, Shougang Zhang, P. Laurent, G. Santarelli, C. Salomon & A. Clairon. *Interrogation oscillator noise rejection in the comparison of atomic fountains.* IEEE Trans. Ultrason., Ferroelect., Freq. Contr., vol. 47, no. 5, page 1253, 2000.

[Bjorklund 80] G. C. Bjorklund. *Frequency-modulation spectroscopy: a new method for measuring weak absorptions and dispersions.* Opt. Lett., vol. 5, no. 1, pages 15–17, 1980.

[Bloch 46] F. Bloch. *Nuclear Induction.* Phys. Rev., vol. 70, pages 460–474, 1946.

[Bloom 13] B. J. Bloom, T. L. Nicholson, J. R. Williams, S. L. Campbell, M. Bishof, X. Zhang, W. Zhang, S. L. Bromley & J. Ye. *A new generation of atomic clocks: accuracy and stability at the* 10^{-18} *Level.* arXiv:1309.1137, 2013.

[Bohnet 13] J. G. Bohnet, K. C. Cox, M. A. Norcia, J. M. Weiner, Z. Chen & J. K. Thompson. *Reduced back-action for phase sensitivity 10 times beyond the standard quantum limit.* arXiv:1310.3177, 2013.

[Borregaard 13a] J. Borregaard & A. S. Sørensen. *Efficient atomic clocks operated with several atomic ensembles.* Phys. Rev. Lett., vol. 111, page 090802, 2013.

[Borregaard 13b] J. Borregaard & A. S. Sørensen. *Near-Heisenberg-limited atomic clocks in the presence of decoherence.* Phys. Rev. Lett., vol. 111, page 090801, 2013.

[Boyer 00] V. Boyer. *Condensation de bose-einstein avec un electroaimant a noyau ferromagnetique : strategies de refroidissement dans des champs magnetiques intenses.* PhD thesis, Université Paris 6, 2000.

[Braginsky 80] V. B. Braginsky, Y. I. Vorontsov & K. S. Thorne. *Quantum nondemolition measurements.* Science, vol. 209, no. 4456, pages 547–557, 1980.

[Brańczyk 07] A. M. Brańczyk, P. E. M. F. Mendonça, A. Gilchrist, A. C. Doherty & S. D. Bartlett. *Quantum control of a single qubit.* Phys. Rev. A, vol. 75, page 012329, 2007.

[Budker 04] D. Budker, D. F. Kimball & D. P. DeMille. Atomic physics: an exploration through problems and solutions. Oxford University Press, 2004.

[Büning 11] G. K. Büning, J. Will, W. Ertmer, E. Rasel, J. Arlt, C. Klempt, F. Ramirez-Martinez, F. Piéchon & P. Rosenbusch. *Extended coherence time on the clock transition of optically trapped Rubidium.* Phys. Rev. Lett., vol. 106, no. 24, page 240801, 2011.

[Chen 11] Z. Chen, J. G. Bohnet, S. R. Sankar, J. Dai & J. K. Thompson. *Conditional spin squeezing of a large ensemble via the vacuum rabi splitting.* Phys. Rev. Lett., vol. 106, page 133601, 2011.

[Clément 09] J.-F. Clément, J.-P. Brantut, M. Robert-de Saint-Vincent, R. A. Nyman, A. Aspect, T. Bourdel & P. Bouyer. *All-optical runaway evaporation to Bose-Einstein condensation.* Phys. Rev. A, vol. 79, page 061406, 2009.

[Dalfovo 99] F. Dalfovo, S. Giorgini, L. P. Pitaevskii & S. Stringari. *Theory of Bose-Einstein condensation in trapped gases.* Rev. Mod. Phys., vol. 71, pages 463–512, 1999.

[Deutsch 10] C. Deutsch, F. Ramirez-Martinez, C. Lacroûte, F. Reinhard, T. Schneider, F. Fuchs J.-N.and Piéchon, F. Laloë, J. Reichel & P. Rosenbusch. *Spin self-rephasing and very long coherence times in a trapped atomic ensemble.* Phys. Rev. Lett., vol. 105, no. 2, page 020401, 2010.

[Dick 87] G. J. Dick. *Local oscillator induced instabilities in trapped ion frequency standards.* Proceedings of the Precise Time and Time Interval Meeting, Redondo Beach, page 133, 1987.

[Dicke 54] R. H. Dicke. *Coherence in spontaneous radiation processes.* Phys. Rev., vol. 93, pages 99–110, 1954.

[Dickerson 13] S. M. Dickerson, J. M. Hogan, A. Sugarbaker, D. M. S. Johnson & M. A. Kasevich. *Multiaxis inertial sensing with long-time point source atom interferometry.* Phys. Rev. Lett., vol. 111, page 083001, 2013.

[Dixon 09] P. B. Dixon, D. J. Starling, A. N. Jordan & J. C. Howell. *Ultrasensitive beam deflection measurement via interferometric weak value amplification.* Phys. Rev. Lett., vol. 102, no. 17, page 173601, 2009.

[Doherty 00] A. C. Doherty, S. Habib, K. Jacobs, H. Mabuchi & S. M. Tan. *Quantum feedback control and classical control theory.* Phys. Rev. A, vol. 62, page 012105, 2000.

[Dorner 12] U Dorner. *Quantum frequency estimation with trapped ions and atoms.* New J. Phys., vol. 14, no. 4, page 043011, 2012.

[Drever 83] R. W. P. Drever, J. L. Hall, F. V. Kowalski, J. Hough, G. M. Ford, A. J. Munley & H. Ward. *Laser phase and frequency stabilization using an optical resonator.* Appl. Phys. B, vol. 31, no. 2, pages 97–105, 1983.

[Dudin 10] Y. O. Dudin, A. G. Radnaev, R. Zhao, J. Z. Blumoff, T. A. B. Kennedy & A. Kuzmich. *Entanglement of light-shift compensated atomic spin waves with telecom light.* Phys. Rev. Lett., vol. 105, no. 26, page 260502, 2010.

[Erhart 12] J. Erhart, S. Sponar, G. Sulyok, G. Badurek, M. Ozawa & Y. Hasegawa. *Experimental demonstration of a universally valid error-disturbance uncertainty relation in spin measurements.* Nature Phys., vol. 8, no. 3, pages 185–189, 2012.

[Esteve 08] J. Esteve, C. Gross, A. Weller, S. Giovanazzi & M. K. Oberthaler. *Squeezing and entanglement in a Bose–Einstein condensate.* Nature, vol. 455, no. 7217, pages 1216–1219, 2008.

[Faust 13] T. Faust, J. Rieger, M. J. Seitner, J. P. Kotthaus & E. M. Weig. *Coherent control of a classical nanomechanical two-level system.* Nature Phys., 2013.

[Ferrie 13] C. Ferrie & J. Combes. *Weak values considered harmful.* arXiv:1307.4016, 2013.

[Feynman 57] R. P. Feynman, F. L. Vernon Jr. & R. W. Hellwarth. *Geometrical representation of the Schrödinger equation for solving maser problems.* J. Appl. Phys., vol. 28, no. 1, pages 49–52, 1957.

[Geiger 11] R. Geiger, V. Ménoret, G. Stern, N. Zahzam, P. Cheinet, B. Battelier, A. Villing, F. Moron, M. Lours, Y. Bidel, A. Bresson, A. Landragin & P. Bouyer. *Detecting inertial effects with airborne matter-wave interferometry.* Nat. Commun., vol. 2, page 474, 2011.

[Gillett 10] G. G. Gillett, R. B. Dalton, B. P. Lanyon, M. P. Almeida, M. Barbieri, G. J. Pryde, J. L. Obrien, K. J. Resch, S. D. Bartlett & A. G. White. *Experimental feedback control of quantum systems using weak measurements.* Phys. Rev. Lett., vol. 104, no. 8, page 080503, 2010.

[Grangier 98] P. Grangier, J. A. Levenson & J.-P. Poizat. *Quantum non-demolition measurements in optics.* Nature, vol. 396, no. 6711, pages 537–542, 1998.

[Grimm 00] R. Grimm, M. Weidemüller & Y. B. Ovchinnikov. *Optical dipole traps for neutral atoms.* vol. 42, pages 95 – 170, 2000.

[Guerlin 07] C. Guerlin, J. Bernu, S. Deléglise, C. Sayrin, S. Gleyzes, S. Kuhr, M. Brune, J.-M. Raimond & S. Haroche. *Progressive field-state collapse and quantum non-demolition photon counting.* Nature, vol. 448, no. 7156, pages 889–893, 2007.

[Hall 84] J. Hall & T. W. Hänsch. *External dye-laser frequency stabilizer.* Opt. Lett., vol. 9, page 502, 1984.

[Hänsch 75] T. W. Hänsch & A .L. Schawlow. *Cooling of gases by laser radiation.* Opt. Commun., vol. 13, no. 1, pages 68 – 69, 1975.

[Hatridge 13] M. Hatridge, S. Shankar, M. Mirrahimi, F. Schackert, K. Geerlings, T. Brecht, K. M. Sliwa, B. Abdo, L. Frunzio, S. M. Girvin, R. J. Schoelkopf & M. H. Devoret. *Quantum back-action of an individual variable-strength measurement.* Science, vol. 339, no. 6116, pages 178–181, 2013.

[Heisenberg 27] W. Heisenberg. *Über den anschaulichen Inhalt der quantentheoretischen Kinematik und Mechanik.* Zeitschrift für Physik, vol. 43, no. 3-4, pages 172–198, 1927.

[Hinkley 13] N. Hinkley, J. A. Sherman, N. B. Phillips, M. Schioppo, N. D. Lemke, K. Beloy, M. Pizzocaro, C. W. Oates & A. D. Ludlow.

An atomic Clock with 10^{18} *instability.* Science, vol. 341, no. 6151, pages 1215–1218, 2013.

[Hosten 08] O. Hosten & P. Kwiat. *Observation of the spin Hall effect of light via weak measurements.* Science, vol. 319, no. 5864, pages 787–790, 2008.

[Houtz 09] R. Houtz, C. Chan & Holger Müller. *Wideband, efficient optical serrodyne frequency shifting with a phase modulator and a nonlinear transmission Line.* Opt. Express, vol. 17, no. 21, pages 19235–19240, 2009.

[Hughes 09] K. J. Hughes, J. H. T. Burke & C. A. Sackett. *Suspension of atoms using optical pulses, and application to gravimetry.* Phys. Rev. Lett., vol. 102, page 150403, 2009.

[Hume 07] D. B. Hume, T. Rosenband & D. J. Wineland. *High-fidelity adaptive qubit detection through repetitive quantum nondemolition measurements.* Phys. Rev. Lett., vol. 99, page 120502, 2007.

[Impens 06] F. Impens, P. Bouyer & Ch. J. Bordé. *Matter-wave cavity gravimeter.* Appl. Phys. B, vol. 84, no. 4, pages 603–615, 2006.

[Inoue 13] R. Inoue, S.-I.-R. Tanaka, R. Namiki, T. Sagawa & Y. Takahashi. *Unconditional quantum-noise suppression via measurement-based quantum feedback.* Phys. Rev. Lett., vol. 110, page 163602, 2013.

[Itano 93] W. M. Itano, J. C. Bergquist, J. J. Bollinger, J. M. Gilligan, D. J. Heinzen, F. L. Moore, M. G. Raizen & D. J. Wineland. *Quantum projection noise: Population fluctuations in two-level systems.* Phys. Rev. A, vol. 47, no. 5, page 3554, 1993.

[Jiang 11] Y. Y. Jiang, A. D. Ludlow, N. D. Lemke, R. W. Fox, J. A. Sherman, L.-S. Ma & C. W. Oates. *Making optical atomic clocks more stable with* 10^{-16}*-level laser stabilization.* Nature Photon., vol. 5, no. 3, pages 158–161, 2011.

[Johnson 88] L. M. Johnson & C. H. Cox III. *Serrodyne optical frequency translation with high sideband suppression.* J. Lightwave Technol., vol. 6, no. 1, pages 109–112, 1988.

[Johnson 10] D. M. S. Johnson, J. M. Hogan, S.-W. Chiow & M. A. Kasevich. *Broadband optical serrodyne frequency shifting.* Opt. Lett., vol. 35, page 745, 2010.

[Jordan 13] A. N. Jordan, J. Martínez-Rincón & J. C. Howell. *Technical advantages for weak value amplification: When less is more.* arXiv:1309.5011, 2013.

[Kaplan 02] A. Kaplan, M. F. Andersen & N. Davidson. *Suppression of inhomogeneous broadening in rf spectroscopy of optically trapped atoms.* Phys. Rev. A, vol. 66, no. 4, page 045401, 2002.

[Kasevich 91] M. Kasevich & S. Chu. *Atomic interferometry using stimulated Raman transitions.* Phys. Rev. Lett., vol. 67, no. 2, page 181, 1991.

[Katz 08] N. Katz, M. Neeley, M. Ansmann, R. C. Bialczak, M. Hofheinz, E. Lucero, A. O'Connell, H. Wang, A. N. Cleland, J. M. Martinis & A. N. Korotkov. *Reversal of the weak measurement of a quantum state in a superconducting phase qubit.* Phys. Rev. Lett., vol. 101, page 200401, 2008.

[Kessler 12] T. Kessler, C. Hagemann, C. Grebing, T. Legero, U. Sterr, F. Riehle, M. J. Martin, L. Chen & J. Ye. *A sub-40-mHz-linewidth laser based on a silicon single-crystal optical cavity.* Nature Photon., vol. 6, no. 10, pages 687–692, 2012.

[Kessler 13] E. M. Kessler, P. Kómár, M. Bishof, L. Jiang, A. S. Sørensen, J. Ye & M. D. Lukin. *Heisenberg-limited atom clocks based on entangled qubits.* arXiv:1310.6043, 2013.

[Ketterle 96] W. Ketterle & N.J. Van Druten. *Evaporative cooling of trapped atoms.* volume 37 of *Adv. At., Mol., Opt. Phys.*, pages 181 – 236. Academic Press, 1996.

[Kitagawa 93] M. Kitagawa & M. Ueda. *Squeezed spin states.* Phys. Rev. A, vol. 47, no. 6A, pages 5138–5143, 1993.

[Knee 13] G. C. Knee & E. M. Gauger. *Weak-value amplification offers no advantage for overcoming technical imperfections.* arXiv:1306.6321, 2013.

[Kogelnik 66] H. Kogelnik & T. Li. *Laser Beams and Resonators.* Appl. Opt., vol. 5, no. 10, pages 1550–1567, 1966.

[Kohlhaas 12] R. Kohlhaas, T. Vanderbruggen, S. Bernon, A. Bertoldi, A. Landragin & P. Bouyer. *Robust laser frequency stabilization by serrodyne modulation.* Opt. Lett., vol. 37, no. 6, pages 1005–1007, 2012.

[Koschorreck 10] M. Koschorreck, M. Napolitano, B. Dubost & M. W. Mitchell. *Sub-projection-noise sensitivity in broadband atomic magnetometry.* Phys. Rev. Lett., vol. 104, page 093602, 2010.

[Kraus 71] K. Kraus. *General state changes in quantum theory.* Annals of Physics, vol. 64, no. 2, pages 311–335, 1971.

[Kraus 83] K. Kraus, A. Böhm, J. D. Dollard & W. H. Wootters. *States, effects, and operations fundamental notions of quantum theory.* In States, Effects, and Operations Fundamental Notions of Quantum Theory, volume 190, 1983.

[Le Targat 13] R. Le Targat*et al.* *Experimental realization of an optical second with strontium lattice clocks.* Nat. Commun., vol. 4, 2013.

[Leroux 10a] I. D. Leroux, M. H. Schleier-Smith & V. Vuletić. *Implementation of cavity squeezing of a collective atomic spin.* Phys. Rev. Lett., vol. 104, page 073602, 2010.

[Leroux 10b] I. D. Leroux, M. H. Schleier-Smith & V. Vuletić. *Orientation-dependent entanglement lifetime in a squeezed atomic clock.* Phys. Rev. Lett., vol. 104, page 250801, 2010.

[Lloyd 00] S. Lloyd. *Coherent quantum feedback.* Phys. Rev. A, vol. 62, no. 2, page 022108, 2000.

[Louchet-Chauvet 10] A. Louchet-Chauvet, J. Appel, J. J. Renema, D. Oblak, N. Kjaergaard & E. S. Polzik. *Entanglement-assisted atomic clock beyond the projection noise limit.* New J. Phys., vol. 12, no. 6, page 065032, 2010.

[Ma 11] J. Ma, X. Wang, C. P. Sun & F. Nori. *Quantum spin squeezing.* Phys. Rep., vol. 509, no. 2, pages 89–165, 2011.

[Mancini 07] S. Mancini & H. M. Wiseman. *Optimal control of entanglement via quantum feedback.* Phys. Rev. A, vol. 75, no. 1, page 012330, 2007.

[Marion 03] H. Marion*et al.* *Search for variations of fundamental constants using atomic fountain clocks.* Phys. Rev. Lett., vol. 90, no. 15, page 150801, 2003.

[Ménoret 11] V. Ménoret, R. Geiger, G. Stern, N. Zahzam, B. Battelier, A. Bresson, A. Landragin & P. Bouyer. *Dual-wavelength laser source for onboard atom interferometry.* Opt. Lett., vol. 36, no. 21, pages 4128–4130, 2011.

[Müntinga 13] H. Müntinga*et al.* *Interferometry with Bose-Einstein condensates in microgravity.* Phys. Rev. Lett., vol. 110, page 093602, 2013.

[O'Brien 07] J. L. O'Brien. *Optical quantum computing.* Science, vol. 318, no. 5856, pages 1567–1570, 2007.

[Ockeloen 13] C. F. Ockeloen, R. Schmied, M. F. Riedel & P. Treutlein. *Quantum Metrology with a Scanning Probe Atom Interferometer.* Phys. Rev. Lett., vol. 111, page 143001, 2013.

[Ozawa 03] M. Ozawa. *Physical content of Heisenberg's uncertainty relation: limitation and reformulation.* Phys. Lett. A, vol. 318, no. 1, pages 21–29, 2003.

[Ozawa 05] M. Ozawa. *Universal uncertainty principle in the measurement operator formalism.* J. Opt. B, vol. 7, no. 12, page S672, 2005.

[Parker 10] T. E. Parker. *Long-term comparison of caesium fountain primary frequency standards.* Metrologia, vol. 47, no. 1, page 1, 2010.

[Quessada 03] A. Quessada, R. P. Kovacich, I. Courtillot, A. Clairon, G. Santarelli & P. Lemonde. *The Dick effect for an optical frequency standard.* J. Opt. B, vol. 5, no. 2, page S150, 2003.

[Ramsey 80] N. F. Ramsey. *The method of successive oscillatory fields.* Physics Today, vol. 33, page 25, 1980.

[Ritchie 91] N. W. M. Ritchie, J. G. Story & R. G. Hulet. *Realization of a measurement of a weak value.* Phys. Rev. Lett., vol. 66, no. 9, page 1107, 1991.

[Robertson 29] H. P. Robertson. *The Uncertainty Principle.* Phys. Rev., vol. 34, pages 163–164, 1929.

[Rosenband 08] T. Rosenband, D. B. Hume, P. O. Schmidt, C. W. Chou, A. Brusch, L. Lorini, W. H. Oskay, R. E. Drullinger, T. M. Fortier, J. E. Stalnaker, S. A. Diddams, W. C. Swann, N. R. Newbury, W. M. Itano, D. J. Wineland & J. C. Bergquist. *Frequency ratio of Al^+ and Hg^+ single-ion optical clocks; metrology at the 17th decimal place.* Science, vol. 319, page 1808, 2008.

[Rosenband 13] T. Rosenband & D. R. Leibrandt. *Exponential scaling of clock stability with atom number.* arXiv:1303.6357, 2013.

[Rowe 01] M. A. Rowe, D. Kielpinski, V. Meyer, C. A. Sackett, W. M. Itano, C. Monroe & D. J. Wineland. *Experimental violation of a Bell's inequality with efficient detection.* Nature, vol. 409, no. 6822, pages 791–794, 2001.

[Rozema 12] L. A. Rozema, A. Darabi, D. H. Mahler, A. Hayat, Y. Soudagar & A. M. Steinberg. *Violation of Heisenbergs measurement-disturbance relationship by weak measurements.* Phys. Rev. Lett., vol. 109, no. 10, page 100404, 2012.

[Safronova 04] M. S. Safronova & C. W. Clark. *Inconsistencies between lifetime and polarizability measurements in Cs.* Phys. Rev. A, vol. 69, no. 4, page 040501, 2004.

[Santarelli 96] G. Santarelli. *Contribution à la réalisation dune fontaine atomique.* PhD thesis, Université Pierre et Marie Curie Paris VI, 1996.

[Santarelli 99] G. Santarelli, Ph. Laurent, P. Lemonde, A. Clairon, A. G. Mann, S. Chang, A. N. Luiten & C. Salomon. *Quantum projection noise in an atomic fountain: a high stability cesium frequency standard.* Phys. Rev. Lett., vol. 82, page 4619, 1999.

[Sayrin 11] C. Sayrin, I. Dotsenko, X. Zhou, B. Peaudecerf, T. Rybarczyk, S. Gleyzes, P. Rouchon, M. Mirrahimi, H. Amini, M. Brune, J.-M. Raimond & S. Haroche. *Real-time quantum feedback prepares and stabilizes photon number states.* Nature, vol. 477, page 73, 2011.

[Schleier-Smith 10] M. H. Schleier-Smith, I. D. Leroux & V. Vuletić. *States of an ensemble of two-level atoms with reduced quantum uncertainty.* Phys. Rev. Lett., vol. 104, page 073604, 2010.

[Sewell 12] R. J. Sewell, M. Koschorreck, M. Napolitano, B. Dubost, N. Behbood & M. W. Mitchell. *Magnetic sensitivity beyond the projection noise limit by spin squeezing.* Phys. Rev. Lett., vol. 109, page 253605, 2012.

[Shaji 07] A. Shaji & C. M. Caves. *Qubit metrology and decoherence.* Phys. Rev. A, vol. 76, no. 3, page 032111, 2007.

[Shiga 12] N. Shiga & M. Takeuchi. *Locking the local oscillator phase to the atomic phase via weak measurement.* New J. Phys., vol. 14, no. 2, page 023034, 2012.

[Smith 02] W. P. Smith, J. E. Reiner, L. A. Orozco, S. Kuhr & H. M. Wiseman. *Capture and release of a conditional state of a cavity QED system by quantum feedback.* Phys. Rev. Lett., vol. 89, no. 13, page 133601, 2002.

[Smith 04] G. A. Smith, S. Chaudhury, A. Silberfarb, I. H. Deutsch & P. S. Jessen. *Continuous weak measurement and nonlinear dynamics in a cold spin ensemble.* Phys. Rev. Lett., vol. 93, page 163602, 2004.

[Sobel 07] Dava Sobel. Longitude: The true story of a lone genius who solved the greatest scientific problem of his time. Walker & Company, reprint edition, 2007.

[Sorrentino 12] F. Sorrentino, A. Bertoldi, Q. Bodart, L. Cacciapuoti, M. De Angelis, Y.-H. Lien, M. Prevedelli, G. Rosi & G. M. Tino. *Simultaneous measurement of gravity acceleration and gravity gradient with an atom interferometer.* Appl. Phys. Lett., vol. 101, no. 11, pages 114106–114106, 2012.

[Steck 01] D. A. Steck. *Rubidium 87 D Line Data*, 2001.

[Stellmer 13] S. Stellmer, B. Pasquiou, R. Grimm & F. Schreck. *Laser cooling to quantum degeneracy.* Phys. Rev. Lett., vol. 110, page 263003, 2013.

[Takamoto 05] M. Takamoto, F.-L. Hong, R. Higashi & H. Katori. *An optical lattice clock.* Nature, vol. 435, no. 7040, pages 321–324, 2005.

[Takamoto 11] M. Takamoto, T. Takano & H. Katori. *Frequency comparison of optical lattice clocks beyond the dick limit.* Nature Photon., vol. 5, page 288, 2011.

[Takano 09] T. Takano, M. Fuyama, R. Namiki & Y. Takahashi. *Spin squeezing of a cold atomic ensemble with the nuclear spin of one-half.* Phys. Rev. Lett., vol. 102, page 033601, 2009.

[Thomsen 02] L. K. Thomsen, S. Mancini & H. M. Wiseman. *Spin squeezing via quantum feedback.* Phys. Rev. A, vol. 65, page 061801, 2002.

[Thorpe 11] M. J. Thorpe, L. Rippe, T. M. Fortier, M. S. Kirchner & T. Rosenband. *Frequency stabilization to* 6×10^{-16} *via spectral-hole burning.* Nature Photon., vol. 5, no. 11, pages 688–693, 2011.

[Ueda 92] M. Ueda & M. Kitagawa. *Reversibility in quantum measurement processes.* Phys. Rev. Lett., vol. 68, pages 3424–3427, 1992.

[Vanderbruggen 11] T. Vanderbruggen, S. Bernon, A. Bertoldi, A. Landragin & P. Bouyer. *Spin-squeezing and Dicke-state preparation by heterodyne measurement.* Phys. Rev. A, vol. 83, page 013821, 2011.

[Vanderbruggen 12] T. Vanderbruggen. *Détection non-destructive pour linterférométrie atomique et Condensation de Bose-Einstein dans une cavité optique de haute nesse.* PhD thesis, Université Paris-Sud, 2012.

[Vanderbruggen 13] T. Vanderbruggen, R. Kohlhaas, A. Bertoldi, S. Bernon, A. Aspect, A. Landragin & P. Bouyer. *Feedback control of trapped coherent atomic ensembles.* Phys. Rev. Lett., vol. 110, page 210503, 2013.

[Vijay 12] R. Vijay, C. Macklin, D. H. Slichter, S. J. Weber, K. W. Murch, R. Naik, A. N. Korotkov & I. Siddiqi. *Stabilizing Rabi oscillations in a superconducting qubit using quantum feedback.* Nature, vol. 490, no. 7418, pages 77–80, 2012.

[von Neumann 96] J. von Neumann. Mathematical foundations of quantum mechanics, volume 2. Princeton university press, 1996.

[Wang 03] X. Wang & B. C. Sanders. *Spin squeezing and pairwise entanglement for symmetric multiqubit states.* Phys. Rev. A, vol. 68, no. 1, page 012101, 2003.

[Weber 03] T. Weber, J. Herbig, M. Mark, H.-C. Naegerl & R. Grimm. *Bose-Einstein condensation of cesium.* Science, vol. 299, page 232, 2003.

[Weihs 98] G. Weihs, T. Jennewein, C. Simon, H. Weinfurter & A. Zeilinger. *Violation of Bell's inequality under strict Einstein locality conditions.* Phys. Rev. Lett., vol. 81, no. 23, page 5039, 1998.

[Wigner 59] E. Wigner. Group theory: and its application to the quantum mechanics of atomic spectra, volume 5. Academic Press, 1959.

[Windpassinger 08] P. J. Windpassinger, D. Oblak, P. G. Petrov, M. Kubasik, M. Saffman, C. L. Garrido Alzar, J. Appel, J. H. Müller, N. Kjærgaard & E. S. Polzik. *Nondestructive probing of Rabi oscillations on the cesium clock transition near the standard quantum limit.* Phys. Rev. Lett., vol. 100, page 103601, 2008.

[Wineland 75] D. J. Wineland & H. G. Dehmelt. *Proposed $10^1 4\ \Delta/$ laser fluorescence spectroscopy on Tl^+ mono-ion oscillator.* Bull. Am. Phys. Soc., vol. 20, page 637, 1975.

[Wineland 78] D. J. Wineland, R. E. Drullinger & F. L. Walls. *Radiation-pressure cooling of bound resonant absorbers.* Phys. Rev. Lett., vol. 40, pages 1639–1642, 1978.

[Wineland 92] D. J. Wineland, J. J. Bollinger, W. M. Itano, F. L. Moore & D. J. Heinzen. *Spin squeezing and reduced quantum noise in spectroscopy.* Phys. Rev. A, vol. 46, no. 11, page R6797, 1992.

[Wineland 98] D. J. Wineland, C. Monroe, W. M. Itano, D. Leibfried, B. E. King & D. M. Meekhof. *Experimental issues in coherent quantum-state manipulation of trapped atomic ions.* J. Res. Natl. Inst. Stand. Technol., vol. 103, page 259, 1998.

[Zhang 90] W.-M. Zhang, D. H. Feng & R. Gilmore. *Coherent states: theory and some applications.* Rev. Mod. Phys., vol. 62, pages 867–927, 1990.

Abstract

In this thesis, we describe an until now unexplored approach in the operation of atomic interferometers; the feedback control of the atomic states during their evolution.
Towards this goal, we present several novel experimental techniques, such as the all-optical Bose-Einstein condensation of ^{87}Rb in a cavity enhanced dipole trap, a new laser stabilization technique based on serrodyne frequency shifting and the development of frequency modulation spectroscopy as a minimal destructive tool for the measurement of atomic population differences. This nondestructive detection is combined with feedback, either directly on the atoms with microwave radiation or on the microwave oscillator. In this way, we show that atomic quantum states can be protected against decoherence from collective noise.
We develop dedicated feedback protocols to use this method to improve atomic interferometers, and experimentally demonstrate one such protocol in an atomic clock. We show that the interrogation time in atomic interferometers can be prolonged, which holds promise for increasing the sensitivity of atomic sensors.

KEYWORDS: Atom Interferometry - Cold Atoms - Nondestructive Measurements - Feedback Control - Optical Cavity - Laser Stabilization

Résumé

Dans cette thèse, nous décrivons une approche jusqu'à maintenant inexploré dans le développement des interféromètres atomiques ; la rétroaction des états atomiques au cours de leur évolution.
Le long de cet objectif, nous présentons des nouvelles techniques expérimentales, comme la condensation de Bose-Einstein tout-optique d'atomes de ^{87}Rb à l'aide d'une cavité optique, une nouvelle technique de stabilisation de laser décalage de fréquence serrodyne et le développement de la' spectroscopie par modulation de fréquence comme un outil non-destructif pour mesurer des différences de population atomique. Cette détection non destructive est combinée à la rétroaction, soit directement sur les atomes avec un rayonnement micro-onde soit sur l'oscillateur à micro-ondes. De cette manière, nous montrons que les états quantiques atomiques peuvent être protégés contre la décohérence d'un bruit collectif.
Grâce à cette méthode, nous développons des protocoles de rétroaction dédiés pour améliorer les interféromètres atomiques, et démontrons expérimentalement l'un d'entre eux dans le cas d'une horloge atomique. Nous montrons que le temps d'interrogation dans les interféromètres atomiques peut être prolongé, ce qui est prometteur pour augmenter la sensibilité des senseurs atomiques.

MOTS-CLÉS : Interférométrie Atomique - Atomes Froids - Mesures Non Destructifs - Contrôle à Rétroaction - Cavité Optique - Stabilisation des Lasers